Important Notice

This copy may be used only for the purposes of research and private study, and any use of the copy for a purpose other than research or private study may require the authorization of the copyright owner of the work in question. Responsibility regarding questions of copyright that may arise in the use of this copy is assumed by the recipient.

UNIVERSITY OF CALGARY

Time-lapse Full-Waveform Inversion for CO_2 Sequestration Monitoring: Strategies and Applications to Field Accelerometer and DAS Data

by

He Liu

A THESIS
SUBMITTED TO THE FACULTY OF GRADUATE STUDIES
IN PARTIAL FULFILLMENT OF THE REQUIREMENTS FOR THE
DEGREE OF DOCTOR OF PHILOSOPHY

GRADUATE PROGRAM IN GEOPHYSICS

CALGARY, ALBERTA
August, 2025

© He Liu 2025

Abstract

Time-lapse full-waveform inversion (FWI) is a powerful technique for seismic analysis, enabling high-resolution imaging of subsurface physical properties to monitor reservoir changes during injection, production, and long-term CO_2 storage. However, accurate time-lapse analysis remains challenging due to the requirement for highly repeatable seismic surveys, including consistent acquisition geometry, stable ambient noise conditions, and other environmental factors. To address these challenges, this thesis develops a target-oriented common-model strategy (TO CMS) to mitigate non-repeatability issues that conventional parallel strategies (PRS) fail to overcome. TO CMS combines the strengths of target-oriented FWI (TO FWI)—which improves inversion convergence within the reservoir region—and the common-model strategy (CMS)—which reduces time-lapse artifacts by guiding both baseline and monitor inversions along similar convergence paths. Additionally, a multi-source amplitude-encoding method is employed to significantly reduce computational cost without compromising inversion accuracy. In the context of field-scale CO_2 monitoring, vertical seismic profile (VSP) surveys provide higher vertical resolution and improved signal-to-noise ratio (SNR) compared to surface seismic methods. When integrated with FWI, VSP data further enhances the detectability of subtle time-lapse anomalies. Despite these advantages, the application of FWI to field VSP data has remained limited due to its sensitivity to non-repeatable acquisition and noise. This thesis presents a field experiment utilizing time-lapse walkaway VSP data and FWI to monitor long-term subsurface changes associated with a small-scale CO_2 injection. The workflow demonstrates that FWI can successfully detect reservoir changes resulting from the injection of less than 60 tons of CO_2 into a shallow, 7-meter-thick reservoir at a depth of approximately 300 meters. The results confirm that even in low-injection-volume scenarios, time-lapse FWI can deliver high-resolution imaging and effectively capture small-scale velocity changes. Building on this, the study further investigates the use of Distributed Acoustic Sensing (DAS) for time-lapse FWI. DAS offers key advantages such as high spatial sampling density, long-term deployment potential, and reduced operational costs, making it a promising alternative to conventional receivers. A second field experiment is conducted at the same site using time-lapse DAS-based VSP data. Despite limited acquisition geometry and the presence of strong near-surface noise, the application of TO CMS enables successful detection of CO_2-induced changes. The time-lapse results show strong agreement with the synthetic test, confirming the robustness of the proposed workflow.

Preface

This thesis, adopting a manuscript-style format, amalgamates the essence of extensive research efforts encapsulated in a series of papers. These papers, which form the core chapters of this thesis, reflect a deep dive into the innovative development of time-lapse full-waveform inversion strategies, and the application of time-lapse full-waveform inversion to field VSP data, especially using Distributed Acoustic Sensing (DAS) technology to achieve low-cost, long-term and small scale CO2 injection and sequestration monitoring.

Chapter 3 has been previously published in the IEEE Transactions ob Geoscience and Remote Sensing, titled "Multi-source time-lapse elastic full-waveform inversion using a target-oriented common-model strategy" authored by Liu H, Fu X, Trad D, Innanen K and Cao D, 2025. This chapter develops a advanced and robust time-lapse full-waveform inversion strategy.

Chapter 4 has been previously published in Geophysics, entitled " High-resolution monitoring of CO2 sequestration using walkaway VSP and full-waveform inversion" authored by Liu H, Fu X, Cai X, Trad D, Innanen K, 2025. This chapter is a field study on time-lapse full-waveform inversion using field VSP data at CaMI, and it explores the feasibility of application of time-lapse full-waveform inverison in a 7-m thin reservior at the shallow depth with a small amount of CO2 injection.

Chapter 5 has been previously published at IMAGE conference in 2025, entitled "Time-lapse full-waveform inversion of distributed acoustic sensing data". This work is authored by Liu H, Fu X, Cai X, Trad D, Innanen K, which first time explores the feasibility of full-

waveform inversion using field DAS data, highlighting the feasbility of DAS technology in the field application for low-cost, long-term of small amount of CO2 injection and sequestration.

Acknowledgements

Initiating this acknowledgment, I wish to express my deep appreciation towards my supervisors Dr. Daniel Trad and Dr. Kris Innanen, whose expertise and mentorship have been nothing short of transformative throughout my doctoral journey. Their sagacious advice, constant encouragement, and insightful critiques were instrumental in shaping my research focus.

A significant portion of the computational groundwork of this thesis was facilitated by Kevin Hall and Marie Macquet, whose assistance in arranging the necessary computational assets was invaluable. Without their support, the progress of this work would have been significantly delayed, if not entirely halted. Engaging with Kevin and Marie also expanded my comprehension of seismic operations and the practical utility of distributed acoustic sensing in real-world scenarios.

My heartfelt thanks go out to all the vibrant minds and kind souls at CREWES, whose camaraderie made my time there immensely gratifying. I am thankful to all the CREWES members, especially my collegues in the same lab for their friendship, enriching discussions, and constructive feedback that undeniably bolstered the quality of my research.

I am grateful to my family and friends for their unwavering belief in me and their unconditional support throughout this journey. Their love, encouragement, and understanding have been a constant source of motivation, enabling me to overcome challenges and persevere.

The financial backing provided by the Government of Alberta and the Society for Exploration Geophysicists was crucial in advancing my studies. Additionally, my sincere appreciation extends to the Natural Sciences and Engineering Research Council of Canada (NSERC) under the grants CRDPJ 461287-14 and CRDPJ 543691-20, and to the corporate benefactors of CREWES, whose financial contributions were pivotal in making this thesis a reality.

Lastly, I express my gratitude towards Carbon Management Canada and the Containment and Monitoring Institute for allowing the inclusion of field data in Chapter 4 and 5.

Dedication

To my parents for their unwavering support and encouragement.

Contents

List of Figures

List of Tables

List of Symbols, Abbreviations, and Nomenclature

Symbol	Definition
CaMI	Containment and monitoring institute
CCS	Carbon Capture and Storage
CCUS	Carbon capture, utilization, and storage
CG	Conjugate gradient
CMC	Carbon Management Canada
CREWES	Consortium for Research in Elastic Wave Exploration Seismology
FRS	Field Research Station
FWI	Full-Waveform Inversion
SNR	Signal-to-noise ratio
VSP	Vertical Seismic Profiling
2D	Two-dimensional
3C	Three-component
3D	Three-dimensional
$\mathbf{d}_{\text{obs}}^{i}$	The ith component observed seismic data
$\mathbf{d}_{\text{syn}}^{i}$	The ith component synthetic seismic data
V_p	P-wave velocity
V_s	S-wave velocity

λ	Lamé's first parameter
μ	Shear modulus or Lamé's second parameter
ρ	Density
$\mathrm{CO_2}$	Carbon Dioxide
PRS	Parallel strategy
SQS	Sequential strategy
DDS	Double difference strategy
CMS	Common-model strategy
CDS	Central difference strategy
TO	Target oriented
RTM	Reverse time migration
$LSRTM$	Least-squares reverse time migration
$MCMC$	Markov Chain Monte Carlo

Chapter 1

Introduction

1.1 CO_2 monitoring and time-lapse full-waveform inversion

The continuous increase in anthropogenic carbon dioxide (CO_2) emissions remains the dominant driver of global climate change, necessitating mitigation strategies that complement renewable energy deployment and improvements in energy efficiency. Carbon Capture, Utilization, and Storage (CCUS) represents a technically mature and large-scale approach for reducing emissions from hard-to-abate industrial sectors. It involves capturing CO_2 from major point sources, utilizing it in chemical or energy processes, and permanently storing it in deep geological formations such as saline aquifers and depleted hydrocarbon reservoirs (Metz et al., 2005; Bachu, 2008; Benson and Cole, 2008; Masson-Delmotte et al., 2021). The security of geological storage is ensured by a combination of structural, residual, solubility, and mineral trapping mechanisms, which have been validated through field demonstrations including the Sleipner, Weyburn, and Quest projects (Arts et al., 2004a; Wright et al., 2009; Eiken et al., 2011). CCUS is inherently interdisciplinary, integrating chemical and process engineering for capture, materials and reservoir engineering for injection and containment, and geoscience, geomechanics, and environmental monitoring for assessing and maintaining storage integrity (Bachu, 2000; Lumley, 2010; Daley et al., 2016; Ringrose and Meckel, 2019).

CO_2 sequestration, as the core component of CCUS, has advanced rapidly over the past decades with the shared goal of mitigating greenhouse gas emissions and ensuring storage security. The development of monitoring technologies and methodologies has become integral to verifying the performance and safety of geological storage. Early field-scale demonstrations, such as the Sleipner project in Norway and the Weyburn project in Canada, established a foundation for understanding CO_2 behavior in subsurface formations and validating predictive models (Benson and Cole, 2008; Vinje et al., 2025). Building on these pioneering efforts, modern monitoring approaches increasingly rely on seismic and geophysical techniques to detect and track plume migration, pressure evolution, and potential leakage pathways within storage reservoirs.

The deployment of advanced monitoring techniques such as seismic monitoring has enhanced the ability to track the migration of CO_2 plumes.Time-lapse seismic analysis is widely used for monitoring subsurface property changes, for instance, the reservoir changes caused by oil/gas production or CO_2 injection (Greaves and Fulp, 1987; Ross and Altan, 1997; Wang et al., 1998; Barkved et al., 2003; Arts et al., 2004b; Barkved et al., 2005; Chadwick et al., 2009; Kazemeini et al., 2010; Pevzner et al., 2017). To enable high-resolution imaging for monitoring subsurface changes, time-lapse seismic analysis often relies on full-waveform inversion (FWI), a powerful technique that offers a detailed reconstruction of subsurface properties. FWI is a high-resolution seismic imaging technique that leverages the full information contained within seismic traces, including both amplitude and phase, to extract physical parameters of the subsurface medium probed by seismic waves (Virieux and Operto, 2009; Virieux et al., 2017; Zhang and Curtis, 2020; Operto et al., 2023), which is proposed by Tarantola (1984) in time domain to invert the subsurface P-wave velocity model by minimizing the $l2$-norm of the difference between predicted and observed data (Symes, 2008).

When FWI is used for time-lapse analysis, the most commonly used strategy is known as the parallel strategy (PRS) (Lumley et al., 2003; Plessix et al., 2010), in which the baseline and monitor models are independently inverted with the same initial model, and the inverted time-lapse change is the difference between two inverted models. However, this conventional strategy suffers from severe artifacts that mainly result from the non-repeatability issue that commonly exist in time-lapse surveys, such as non-repeatable source/receiver locations, noises, surface velocities, etc. Hence, many researcher have proposed different strategies to deal with this issue. Routh et al. (2012) propose to use the inverted baseline model as the initial model for the monitor model inversion to save computational time, which is known as the sequential strategy (SQS). Watanabe et al. (2004) and Zheng et al. (2011) introduce the double-difference strategy (DDS), but it's still very sensitive to source/receiver locations (Zhou and Lumley, 2021b; Fu and Innanen, 2023). Zhang and Huang (2013) take the DDS a step further by incorporating a target-oriented scheme (updating the local area, including reservoir changes in the model, instead of the entire model) to enhance the effectiveness of time-lapse EFWI. For the reason of focusing on reservoir change, the DDS has become a popular strategy in field data application and numerical tests (Yang et al., 2015a, 2016; Malcolm and Willemsen, 2016). Hicks et al. (2016) propose the common-model strategy (CMS), which consists of two stages of inversions, and each stage follows the same process as the PRS. In the second stage of the CMS, the inverted baseline and monitor models from the first stage are averaged as the new initial model. This strategy has been adopted in field data in a North Sea field (Hicks et al., 2016) and a post-salt field in the Campos Basin Bortoni et al. (2021). This strategy shows improved performance in mitigating artifacts and is less sensitive in the case of non-repeatability of source locations.

In chapter 3, we develop a target-oriented common-model strategy (TO CMS) for time-lapse FWI, incorporating a multi-source method (chapter 2). All the mentioned implementations in time-lapse data are based on acoustic FWI. Hereon, we extend this strategy to time-lapse elastic FWI. This approach leverages the advantages of TO FWI, which enhances model convergence in the target area to improve time-lapse results, and common-model time-lapse FWI, which mitigates time-lapse errors by using an optimized starting model to guide baseline and monitor inversions toward similar convergence. Both strategies help suppress artifacts in the inverted time-lapse results, while the multi-source method—an amplitude-encoding strategy—effectively reduces computational overhead by allowing multiple seismic shots to be simulated simultaneously in the FWI.

In field CCUS projects, time-lapse seismic inversion is a powerful tool for monitoring reservoir changes introduced by CO_2 injection and sequestration. Vertical seismic profile (VSP) surveys offer higher vertical resolution and an improved signal-to-noise ratio compared with surface seismic methods. When combined with full-waveform inversion (FWI), a high-resolution seismic imaging technique capable of capturing subtle reservoir changes over time (Virieux and Operto, 2009), VSP data further improves the detection of time-lapse anomalies. This makes the application of FWI to VSP data particularly well-suited for reservoir monitoring. Liang et al. (2013) detected the time-lapse changes in a heavy oil field introduced by steam injection. Yang et al. (2014) reported challenges in detecting time-lapse differences related to CO_2 injection, partly due to limitations in acquisition geometry. A notable result was obtained by Egorov et al. (2017), who applied FWI to single-source VSP data and identified changes in a saline aquifer at 1500 m depth, caused by the injection of 15,000 tons of CO_2. Cai et al. (2024) used FWI to monitor short-term CO_2 injection at 300 m depth with rapidly repeated single-source VSP data. Other studies have explored using FWI with various borehole data to monitor water injection at shallow depths. Nakata et al. (2022) monitored the dynamic transient fluid-flow effects introduced by water injection at a depth around 25 m, using controlled-source crosswell data. Liu et al. (2023) monitored velocity changes at an approximate depth of 11.6 m associated with in-situ fracture evolution at a shallow contamination site, using continuous active-source borehole data. These studies underscore the potential of this technique for high-resolution subsurface imaging. However, due to its sensitivity to non-repeatable noise, the application of FWI to time-lapse VSP data remains relatively rare, particularly for CO_2 monitoring.

Unlike the cases mentioned above, which involve shallow water injection, large-scale deep

CO_2 injections, single-source time-lapse surveys, or short-term monitoring, Chapter 4 conducts a field experiment using time-lapse walkaway VSP data and FWI to track long-term changes in a thin (7 meters), shallow (at approximately 300 m depth) reservoir caused by less than 60 tons of CO_2 injection. At the Field Research Station (FRS), located approximately 200 km southeast of Calgary and developed by the Containment and Monitoring Institute (CaMI) under Canada Management Canada (CMC) Research Institutes Inc., a small scale CO_2 sequestration project is undergoing. Less than 60 tons of CO_2 was injected within a 7 m-thick target formation. The VSP datasets were acquired with accelerometers and Distributed Acoustic Sensing (DAS) in 2018 and 2022, serving as the baseline and monitor data (Hall et al., 2019a; Innanen et al., 2022).

Distributed Acoustic Sensing (DAS) is a revolutionary technology that transforms passive optical fibers into an array of virtual microphones, enabling continuous monitoring and real-time analysis of acoustic interactions along the fiber's length. This technology is predicated on the backscatter of light within the fiber induced by acoustic vibrations surrounding it. Over the past decade, DAS has playing a critical role across a spectrum of geological, environmental, and urban studies. Initially demonstrated in diverse settings such as CCUS sites and infrastructure test facilities (Daley et al., 2013; Ancelle et al., 2014; Macquet et al., 2022), DAS has since proven its efficacy in harsh environments, including permafrost, glaciated terrains, and geothermal areas (Ajo-Franklin et al., 2016; Walter et al., 2020; Jousset et al., 2017).

In borehole seismic exploration, DAS is a great new tool for subsurface investigation due to its resilience under extreme conditions, cost-efficiency, and enhanced data acquisition capabilities. DAS technology, especially in the context of DAS-VSP, significantly reduces operational costs. Its application in 3D DAS-VSP surveys has proven particularly effective in delineating complex geological structures with higher spatial resolution and wider frequency ranges. Furthermore, alternative cable designs, such as helical and straight fiber, have been explored to improve DAS performance (Hall et al., 2018, 2019b). Time-lapse 3D DAS-VSP, or 4D surveys, have shown immense promise in monitoring subsurface property variations, crucial for operations like CO_2 sequestration, hydraulic fracturing, and fluid injections.

Distributed Acoustic Sensing (DAS) holds a promising potential for advancing the efficacy and safety of CO_2 sequestration and monitoring processes, a critical facet of carbon capture and storage endeavors. The technology facilitates real-time monitoring of the subsurface, enabling the detection and mapping of CO_2 plume migration within the storage reservoirs (Daley et al., 2013). DAS's high spatial and temporal resolution makes it a valuable tool for tracking the injection of CO_2, and its dispersion in subsurface formations, thus providing a robust framework for validating reservoir models and ensuring the integrity of the sequestration sites (Dou et al., 2017). Moreover, the technology aids in the identification and assessment of induced seismicity or any other geomechanical alterations which might arise from the injection processes, offering an early-warning system for potential leaks or caprock integrity breaches. The passive and continuous monitoring capacity of DAS allows for a comprehensive surveillance over the sequestration lifecycle, assuring compliance with regulatory frameworks and public safety mandates. By delivering a deeper understanding of the subsurface dynamics associated with CO_2 sequestration, DAS significantly contributes to optimizing the operational procedures and bolstering the public and regulatory confidence in CCUS technologies as viable solutions for reducing greenhouse gas emissions.

In Chapter 5, I conduct a field experiment using time-lapse walkaway DAS VSP data and FWI to monitor long-term subsurface changes induced by CO_2 injection. Chapter 5 present a workflow that applies FWI to detect time-lapse anomalies associated with the injection of less than 60 tons of CO_2 into a 7 m-thick shallow reservoir. The results demonstrate the capability of DAS-based FWI to achieve high-resolution inversion and accurately track small-scale CO_2-induced changes. This study highlights the feasibility of leveraging DAS for long-term, high-resolution CO_2 monitoring in real field conditions.

1.2 Contributions

The contributions of this thesis lay in the following points:

1 In Chapter 3, a target-oriented common-model strategy (TO CMS) for time-lapse FWI, incorporating a multi-source method is developed. This approach leverages the advantages of TO FWI, which enhances model convergence in the target area to improve time-lapse results, and common-model time-lapse FWI, which mitigates time-lapse errors by using an optimized starting model to guide baseline and monitor inversions toward similar convergence. Both strategies help suppress artifacts in the inverted time-lapse results, while the multi-source method—an amplitude-encoding strategy—effectively reduces computational overhead by allowing multiple seismic shots to be simulated simultaneously in the FWI.

2 In Chapter 4, a field experiment using time-lapse VSP data and FWI to monitor long-term changes in a thin, shallow reservoir due to CO_2 injection is conducted. We present a workflow that uses time-lapse FWI for field walkway VSP data to identify time-lapse changes related to less than 60 tons of CO_2 injected into a 7 m-thick reservoir at a depth of 300 m. A frequency range of 5 to 60 Hz is applied to achieve high-resolution results. This experiment showcases the capability of FWI to perform high-resolution inversion and detect time-lapse anomalies within a shallow reservoir caused by a small amount of CO_2 injection. To the best of our knowledge, no similar field experiments have been reported.

3. In Chapter 5, we conduct a field experiment using time-lapse walkaway DAS VSP data and FWI to monitor long-term subsurface changes induced by CO_2 injection. We present a workflow that applies FWI to detect time-lapse anomalies associated with the injection of less than 60 tons of CO_2 into a 7 m-thick shallow reservoir. Our results demonstrate the capability of DAS-based FWI to achieve high-resolution inversion and accurately track small-scale CO_2-induced changes. This study highlights the feasibility of leveraging DAS for long-term, high-resolution CO_2 monitoring in real field conditions.

1.3 Thesis overview and objectives

The thesis presents an in-depth exploration of underground geophysical methods, focusing particularly on monitoring CO_2 injection and sequestration. This research is structured into six chapters, each addressing critical aspects of geophysical methods and its applications on time-lapse seismic data.

Chapter 1 sets the stage by discussing the current development in CO_2 sequestration and monitoring, as well as the application of seismic geophysics in it. Meanwhile, it introduces the capabilities of DAS in capturing the intricacies of CO_2 sequestration, laying the groundwork for the advanced techniques discussed in later chapters. Besides, in later sections, it introduces the main approaches that are studied in this thesis- (Time-lapse) full-waveform inverison. At last, it also introduces FWI using multi-source strategies, which elevate the calculation effiencey.

Chapter 2 delves into the implementation of FWI using a multi-source strategy. This section unravels the improved calculation effiency of FWI and offers a option for time-lapse FWI.

Chapter 3 develops a target-oriented common-model strategy, which provides a robust and effective result for time-lapse elastic FWI. This chapter demonstrates that this strategy is non-sensitive to the non-repeatability issues that commonly exist in field time-lapse surveys. In addition, a multi-source strategy is incorporated into FWI, which well help elevate the calculation overburden issue of time-lapse elastic FWI.

Chapter 4 focuses on the application of time-lapse FWI to Vertical Seismic Profile (VSP) data and explores the potential of this technique in monitoring CO_2 injection and sequestration within a 7-m thin reservoir at shallow depth. The chapter bridges the gap between theory and application, highlighting the enhanced imaging capabilities achieved through this approach.

Chapter 5 focuses on the application of DAS in CO_2 monitoring, and time-lapse FWI is performed using DAS VSP data at CaMI to monitor the CO_2 injection and sequestration within a 7-m thin reservoir at shallow depth. This chapter presents the first-time application of FWI using DAS data, highlighting the capability of DAS data providing low-cost, high-resolution inversion results in CO_2 monitoring.

Finally, Chapter 6 concludes the thesis by summarizing the key contributions and findings of the research. It presents a synthesis of the insights gained from each chapter and offers a perspective on the future applications and developments of time-lapse FWI stategies, and field experiments especially using DAS technology in monitoring and CO_2 sequestration.

Each chapter of this thesis is a stepping stone towards a comprehensive understanding of time-lapse FWI and DAS technology applications in geophysics, culminating in a substantial contribution to the field and paving the way for future research in effective CO_2 monitoring and sequestration.

While this thesis focuses on developing advanced time-lapse FWI strategies and demonstrating their feasibility and effectiveness for monitoring CO_2 injection using both conventional and DAS VSP data, several limitations remain. The non-repeatability scenarios tested using the target-oriented common-model strategy are relatively moderate compared with those encountered in real field surveys; therefore, developing more powerful and robust time-lapse FWI strategies remains an important goal. In the field data application, the inversion accuracy is constrained by incomplete near-surface velocity information, the absence of shear-wave and density models, and the limited quality and repeatability of the field DAS data. The proposed TO-CMS is adopted as a practical solution to mitigate non-repeatable acquisition geometry; however, it inevitably reduces sensitivity to subtle overburden changes that may indicate CO_2 leakage. These limitations define the current scope of this work and underscore the need for future research to develop more adaptive and overburden-aware inversion strategies for reliable and sensitive CO_2 sequestration monitoring.

Chapter 2

Multi-source full-waveform inversion

A super-shot or blended data strategy has been used in marine and land seismic surveys to reduce acquisition costs by reducing the time spent on the field. Full waveform inversion (FWI) has been used to estimate high-resolution subsurface velocity models. However, it suffers from expensive computational costs for matching the synthetic and the observed data. To reduce the costs of both data acquisition and processing, FWI using blended data has been recognized as very promising in future oil exploration. In this work, we use an amplitude-encoding strategy with different bases to accelerate the FWI process and compare their performance. The synthetic examples show that amplitude-encoding FWI using different bases as encoding functions can mitigate the crosstalk noise very well, providing good estimations of velocity models and convergence rate for both acoustic and elastic media. To further improve the calculation efficiency, we also adopt the dynamic encoding concept and reduce the number of super-shots every a few iterations. Since the encoding functions are not changed during the iterations, we can directly simulate the super-shots without the blending stage. From the updated velocity model comparison, we can see that the inversion results by dynamic encoding are almost identical to those by static encoding with further reduced calculation effort. This multi-source strategy will be adopted in chapter 3.

2.1 Introduction

FWI is a high-resolution seismic imaging technique that is based on using the entire content of seismic traces for extracting physical parameters of the medium sampled by seismic waves (Virieux et al., 2017). The classical time-domain FWI was originally proposed by Tarantola (1984) to invert the velocity model by minimizing the l2-norm of the difference between predicted and observed data (Symes, 2008). This technique is very useful but computationally expensive.

To reduce the costs of both data acquisition and processing, a simultaneous source-firing strategy has been recognized as very promising in future oil exploration. Increasing field efficiency by recording more than one source has been explored utilizing encoded shot gathers or super-shots (Romero et al., 2000). However, once the super-shots are acquired, traditional seismic processing methods require a de-blending process for velocity model estimation and seismic migration (Florez et al., 2016).

Source-encoding strategies were first introduced into pre-stack migration in the frequency domain (Morton and Ober, 1998; Romero et al., 2000). Krebs et al. (2009) proposed to multiply the source wavelet with a random encoding sequence of +1 or -1 and then blend all the shot gathers into one super-shot. Zhan et al. (2009) proposed to compose a multi-source shot gather of a sum of single-shot gathers with random time delays. This usually requires zero-padding the input shot gathers along the time axis, which may add extra cost for the time-domain wave extrapolator and memory. Dai et al. (2012) proposed to combine these two source-encoding strategies for least-squares reverse time migration (LSRTM). Usually, all shots are blended into several sub-super-shots that contain all the shot records. Hu et al. (2016) proposed an efficient amplitude encoding strategy using a cosine basis to perform LSRTM. Godwin and Sava (2013) proposed an amplitude encoding strategy using Hartley basis for wave-equation migration and compared its performance with some other source-encoding strategies. To date, source-encoding strategies have been used to accelerate RTM, LSRTM and FWI process (Krebs et al., 2009; Dai et al., 2012; Godwin and Sava, 2013;

Pan, 2017). Instead of modifying the phase or zero-padding the input shot gathers, the implementation of the amplitude encoding method is based on weighting the amplitude of the shot gathers. Therefore, it can be conveniently incorporated into the time-domain wave propagator. What is also different is that one super shot contains all the shot gathers.

In this work, we present amplitude encoding acoustic and elastic FWI using different bases and compare the inversion results. We also adopt the dynamic encoding concept and change the number of super-shots every a few iterations to further reduce the calculation effort.

2.2 Amplitude-encoding FWI in time domain

In the case of constant density, the acoustic wave equation is described by

$$\frac{1}{v^2(\mathbf{x})}\frac{\partial^2 p\left(\mathbf{x},t;\mathbf{x}_s\right)}{\partial t^2}-\nabla^2 p\left(\mathbf{x},t;\mathbf{x}_s\right)=f_s\left(\mathbf{x},t;\mathbf{x}_s\right) \tag{2.1}$$

where $f_s\left(x,t;x_s\right)=f\left(t'\right)\delta\left(x-x_s\right)\delta\left(t-t'\right)$.

According to equation 2.1, the data misfit $\Delta p=p_{cal}-p_{obs}$ can be defined by the differences at the receiver positions between the recorded seismic data p_{obs} and the forward modeled seismic data $p_{\text{cal}}=f(m)$ for each source-receiver pair of the seismic survey. In the acoustic velocity inversion, $f(\cdot)$ indicates the forward modeling function, whereas m corresponds to the velocity model to be inverted. The goal of FWI is to match the data misfit by iteratively updating the velocity model. We also define the data misfit function as the objective function taking the least-squares norm of the misfit vector Δp, which is given by

$$\begin{aligned} E(\mathbf{m}) &= \frac{1}{2}\Delta\mathbf{p}^{\dagger}\Delta\mathbf{p}=\frac{1}{2}\left\|\mathbf{p}_{\text{cal}}-\mathbf{p}_{\text{obs}}\right\|^2 \\ &= \frac{1}{2}\sum_{r=1}^{ng}\sum_{s=1}^{ns}\int_0^{t_{\max}}\mathrm{d}t\left|p_{\text{cal}}\left(\mathbf{x}_r,t;\mathbf{x}_s\right)-p_{\text{obs}}\left(\mathbf{x}_r,t;\mathbf{x}_s\right)\right|^2 \end{aligned} \tag{2.2}$$

where ns and ng are the number of sources and receivers and † denotes the adjoint operator (conjugate transpose).

In encoding FWI, shot gathers are transformed into super shot gathers by the encoding matrix, which is defined as

$$\mathbf{B} = \begin{bmatrix} b^{1,1} & b^{2,1} & . & b^{N_{ig},1} \\ b^{1,2} & b^{2,2} & . & b^{N_{sig},2} \\ . & . & . & . \\ b^{1,N_{sup}} & b^{2,N_{sup}} & . & b^{N_{sig} \cdot N_{sup}} \end{bmatrix} \tag{2.3}$$

where N_{sup} is the number of the super-shots and N_{sig} is the number of the individual shots ($N_{sup} < N_{sig}$). The N_{sig} synthetic data and observed data are blended into N_{sup} blended data by

$$\begin{aligned} \mathbf{p}_{\text{cal}}^{\text{sup}} &= \mathbf{B}\mathbf{p}_{\text{cal}} \\ \mathbf{p}_{\text{obs}}^{\text{sup}} &= \mathbf{B}\mathbf{p}_{\text{obs}} \end{aligned} \tag{2.4}$$

The ratio between N_{sig} and N_{sup} is the factor by which the computational cost is reduced. Since usually N_{sup} is much smaller than N_{sig}, the encoding FWI would achieve much better efficiency due to the reduction of data dimension. Then the encoding objective function is given by:

$$\begin{aligned} E(\mathbf{m}) = \frac{1}{2}\Delta\mathbf{p}^{\dagger}\Delta\mathbf{p} &= \frac{1}{2}\left\|\mathbf{p}_{\text{cal}} - \mathbf{p}_{\text{obs}}\right\|^2 \\ &= \frac{1}{2}\left(p_{\text{cal}} - p_{\text{obs}}\right)\mathbf{B}^{\text{T}}\mathbf{B}\left(p_{\text{cal}} - p_{\text{obs}}\right) \end{aligned} \tag{2.5}$$

The matrix $\mathbf{B}^T\mathbf{B}$ is referred to as the crosstalk matrix, and when it's equal to the identity matrix, the encoding objective function is equal to the traditional objective function. FWI using blended data would produce the same results as in conventional FWI cases. Therefore, to make the inversion result from the encoding FWI comparable with that from the conventional FWI, the designed encoding crosstalk matrix should be a good approximation of the identity matrix.

In this work, we use different bases as the encoding functions to design the amplitude encoding matrices.

The Hartley encoding matrix is defined as (Tsitsas, 2010):

$$b_{m,n} = \cos\left(\frac{2\pi mn}{n_{\text{sig}}}\right) + \sin\left(\frac{2\pi mn}{n_{\text{sig}}}\right) \tag{2.6}$$

The discrete form of the cosine basis is (Hu et al., 2016):

$$b_{m,n} = \sqrt{\frac{2}{n_{\text{sig}}}} \cos\left(\frac{\pi}{n_{\text{sig}}} \frac{(2m\%n_{\text{sig}} + 1)(2n + 1)}{4}\right) \tag{2.7}$$

The sine encoding matrix is defined as (Tsitsas, 2010):

$$\mathrm{b}_{m,n} = \sqrt{\frac{2}{n_{\text{sig}}}} \sin\left(\frac{\left(m + \frac{1}{2}\right)\left(n + \frac{1}{2}\right)\pi}{n_{\text{sig}}}\right) \tag{2.8}$$

Also, we noticed that the random polarity encoding strategy (Krebs et al., 2009) works in a very similar way. It also applies different weights to the shot records or source wavelets to compose super-shots, except that the weights are only + 1 or -1. In addition, it composes all the individual shots into only one super-shot, and changes the encoding sequence at each iteration. In this work, we use it in a different way, we don't change the encoding sequence at each iteration, but also use it as a basis and establish a encoding matrix, and then compose multiple super-shots. Given enough number of individual shots and super-shots, the crosstalk matrix for this basis will also be close to an identity matrix. The random polarity basis can be expressed as:

$$\mathrm{b}_{m,n} = 1 \text{ or } -1 \tag{2.9}$$

In equation 6 to 10, the parameters are defined in the same way, $m = 1, \ldots, N_{sig}$ is the shot-index, $n = 1, \ldots, N_{sup}$ is the super-shot index, and n_{sig} is the periodization index, which we set to be half of N_{sig}.

2.3 Numerical results for acoustic FWI

2.3.1 Marmousi model

In this section, we use a Marmousi model with a distance of 9216 m and a depth of 3008 m on a grid of 16 meters discretized in a grid of 576 by 188 grid points, which is shown in Fig 2.1a. On top of the Marmousi model is a water layer with the thickness of 320 m, the acoustic velocity is set to 1500 m/s. which makes the whole model size 576 by 208 grid points. We get the initial model shown in Fig 2.1b by smoothing the original Marmousi model, but the top layer remains not smoothed.

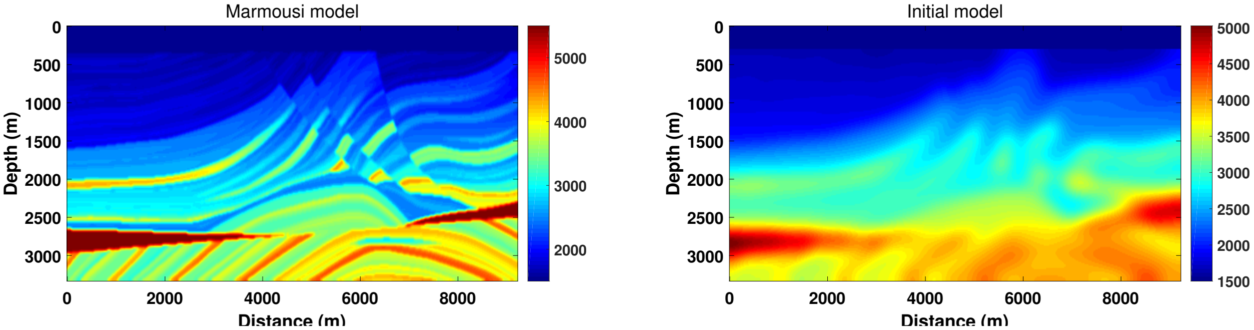

Figure 2.1: (a) The original Marmousi is down sampled along depth and lateral direction. The shots are generated according to the Marmousi model. (b) The initial model of FWI for Marmousi model, which is obtained by smoothing the original model.

In this work, we generate all synthetic shot gathers by solving the acoustic wave equations in time domain for all 140 sources, which are evenly distributed near the surface of original Marmousi model with a spatial interval of 64 m (4 grid points). We deploy 576 receivers right beneath the sources with a spatial interval of 16 m (1 grid point). The Ricker wavelet sources are fired with a central frequency of 4 Hz. We record the seismic waveforms for 4.2 s with an time step of 1.5 ms. For conventional FWI, all the sources are fired individually and shot gathers are recorded separately. For amplitude encoding FWI, we apply different amplitude weights to the shot gathers to compose super-shots.

In our experiments, we use Hartley, cosine, sine and random polarity as encoding functions. For comparison, we blend all the shot gathers into 7, 35 and 70 super-shots. Fig 2.2 and Fig 2.3 are the encoding matrices and corresponding crosstalk matrices. The elements of encoding matrices are the weights we apply to the individual shots and compose super-shots. The crosstalk matrices show how close they are to an identity matrix. We can see with an increasing number of blended data, more off-diagonal elements are close to zero.

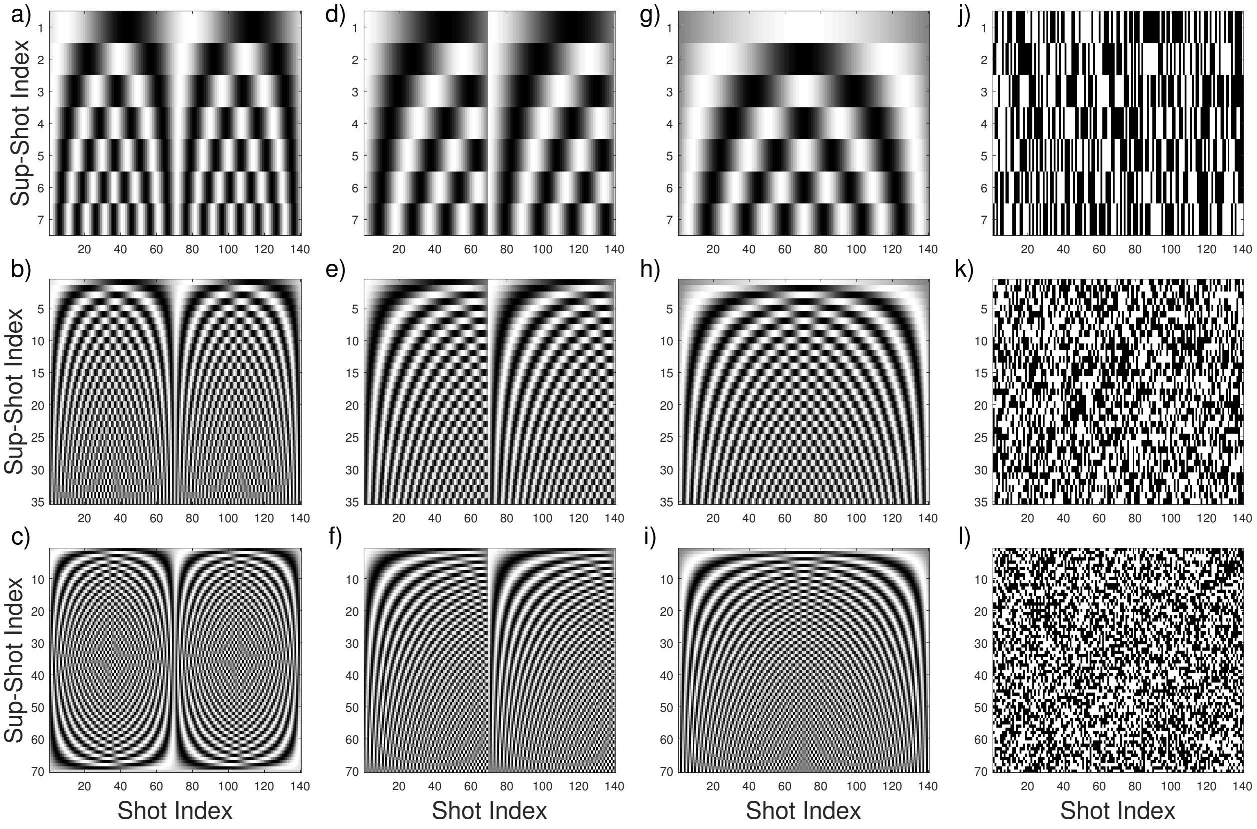

Figure 2.2: Amplitude encoding matrices: columns from left to right are by Hartley, cosine, sine and random polarity bases; rows from up to down are for 7, 35 and 70 super-shots, respectively.

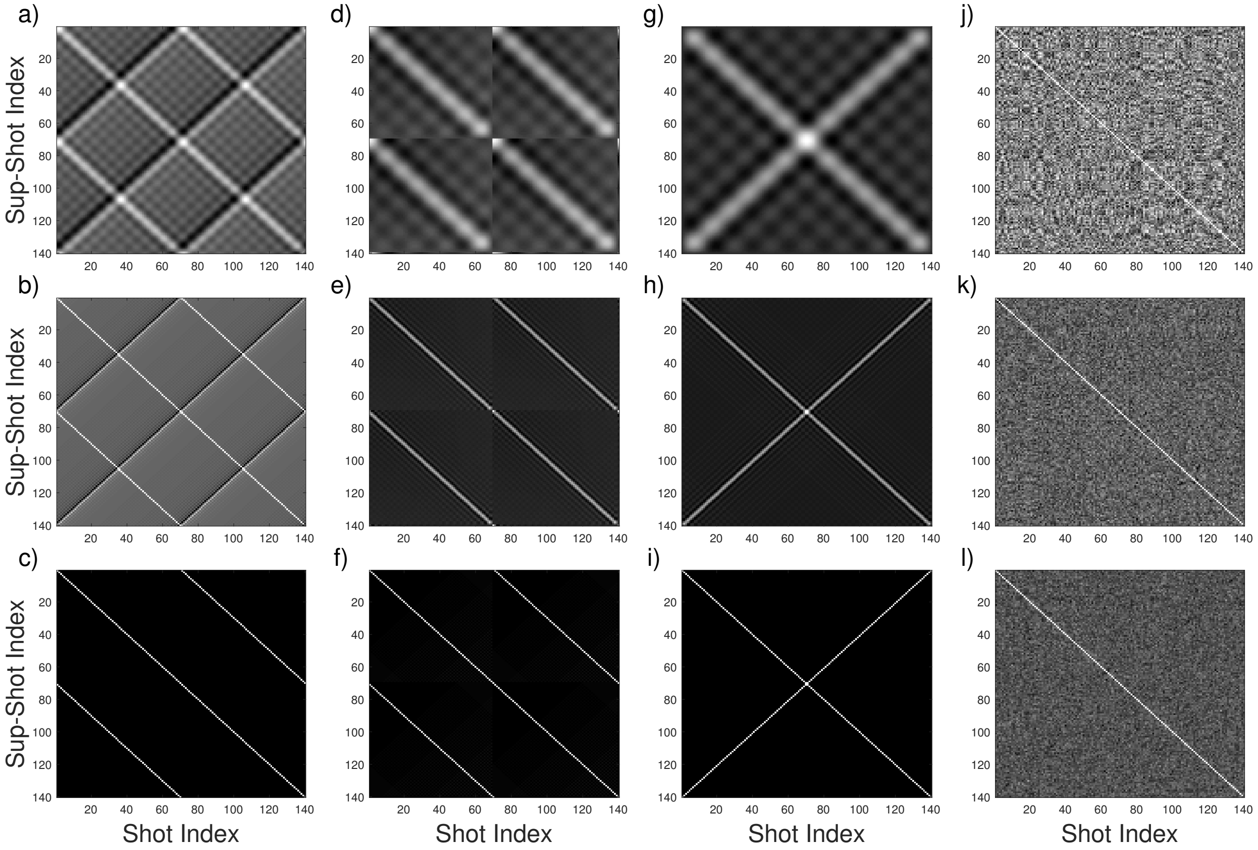

Figure 2.3: crosstalk matrices: columns from left to right are by Hartley, cosine, sine and random polarity bases; rows from up to down are for 7, 35 and 70 super-shots, respectively.

In Fig 2.4, we present the first individual shot in the conventional case and the first super-shots in the amplitude-encoding cases using different bases. We can notice that each super-shot contains all the individual shots and information of the whole model.

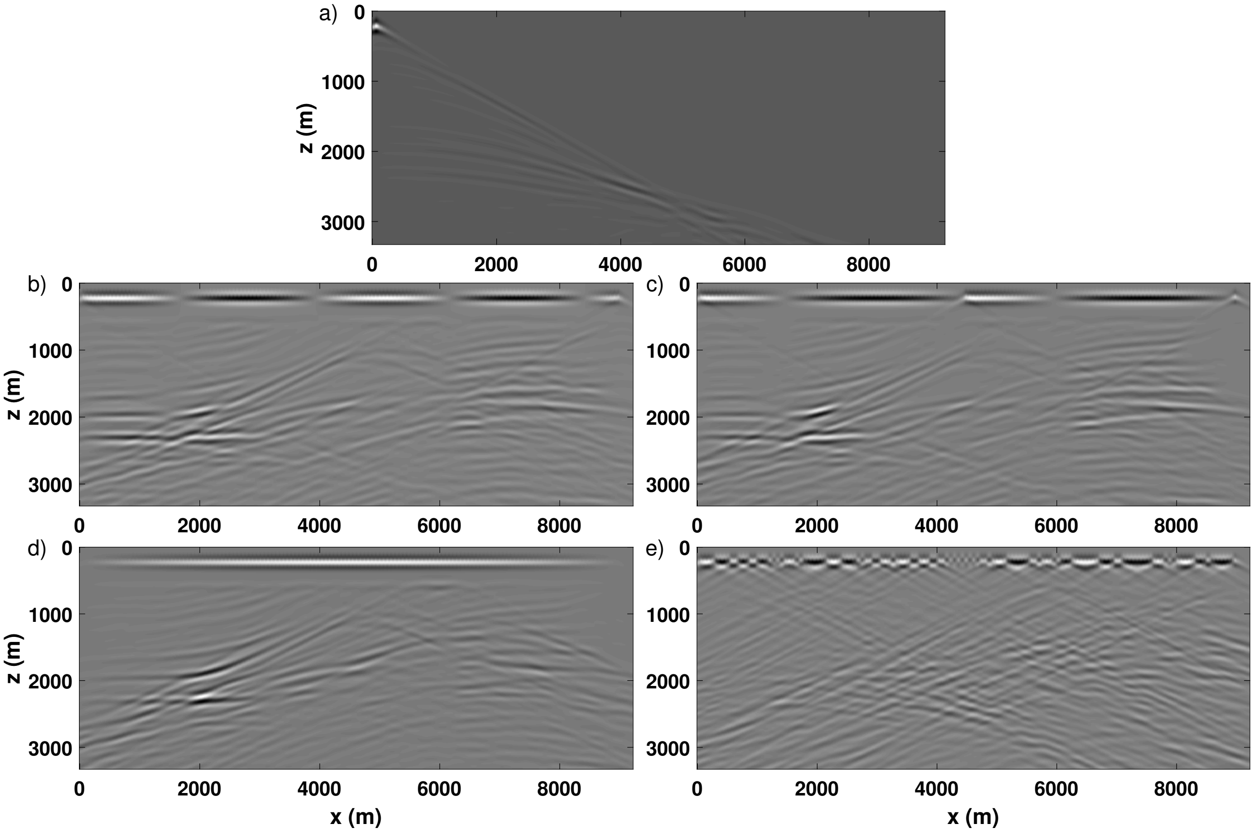

Figure 2.4: a) is the first individual shot in the conventional case; b) to e) are the first super-shot in the amplitude-encoding cases.

In this work, we run FWI using a gradient-based method (Yang et al., 2015b) for 100 iterations. For comparison, we first present the inversion result using conventional FWI, which is displayed in Fig 2.5a. Then we perform amplitude-encoding FWI using different bases as the encoding functions. For brevity, the inversion results at the early stage using 7 and 70 super-shots are shown in Fig 2.5b-i. When we first take a look at the left column using 7 super-shots (see Fig 2.5b, d, f and h), we can notice there exists some crosstalk noise in the middle left or upper left, while with increasing number of super-shots (see results using 70 super-shots in the right column in Fig 2.5) , the crosstalk noise can be better mitigated and the images are almost noise-free.

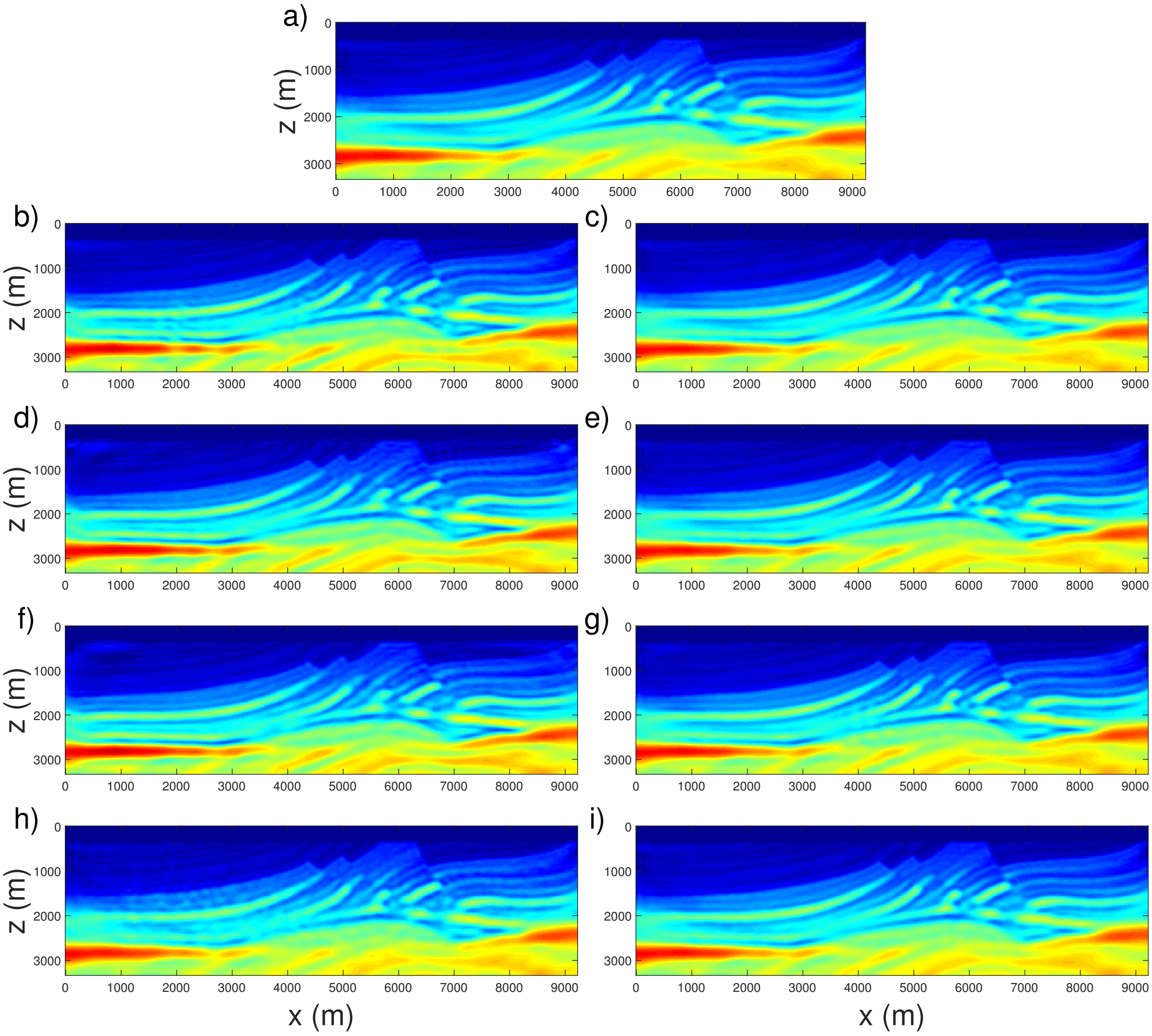

Figure 2.5: The updated velocity models after 25 iterations: a) by conventional FWI; b) and c) are by Hartley basis with 7 and 70 super-shots; d) and e) are by cosine basis with 7 and 70 super-shots; f) and g) are by sine basis with 7 and 70 super-shots; h) and i) are by random polarity basis with 7 and 70 super-shots.

The inversion results after 100 iterations are shown in Fig 2.6. Generally, in our experiments, compared with the result by conventional FWI in Fig 2.6a, we can see amplitude-encoding FWI using all 4 different encoding functions would produce very good estimations of the velocity model, even with only 7 super-shots (see the left columns in Fig 2.5 and 2.6).

However, to achieve better imaging quality, it still requires more super-shots to mitigate the crosstalk noise with much more extra calculation effort.

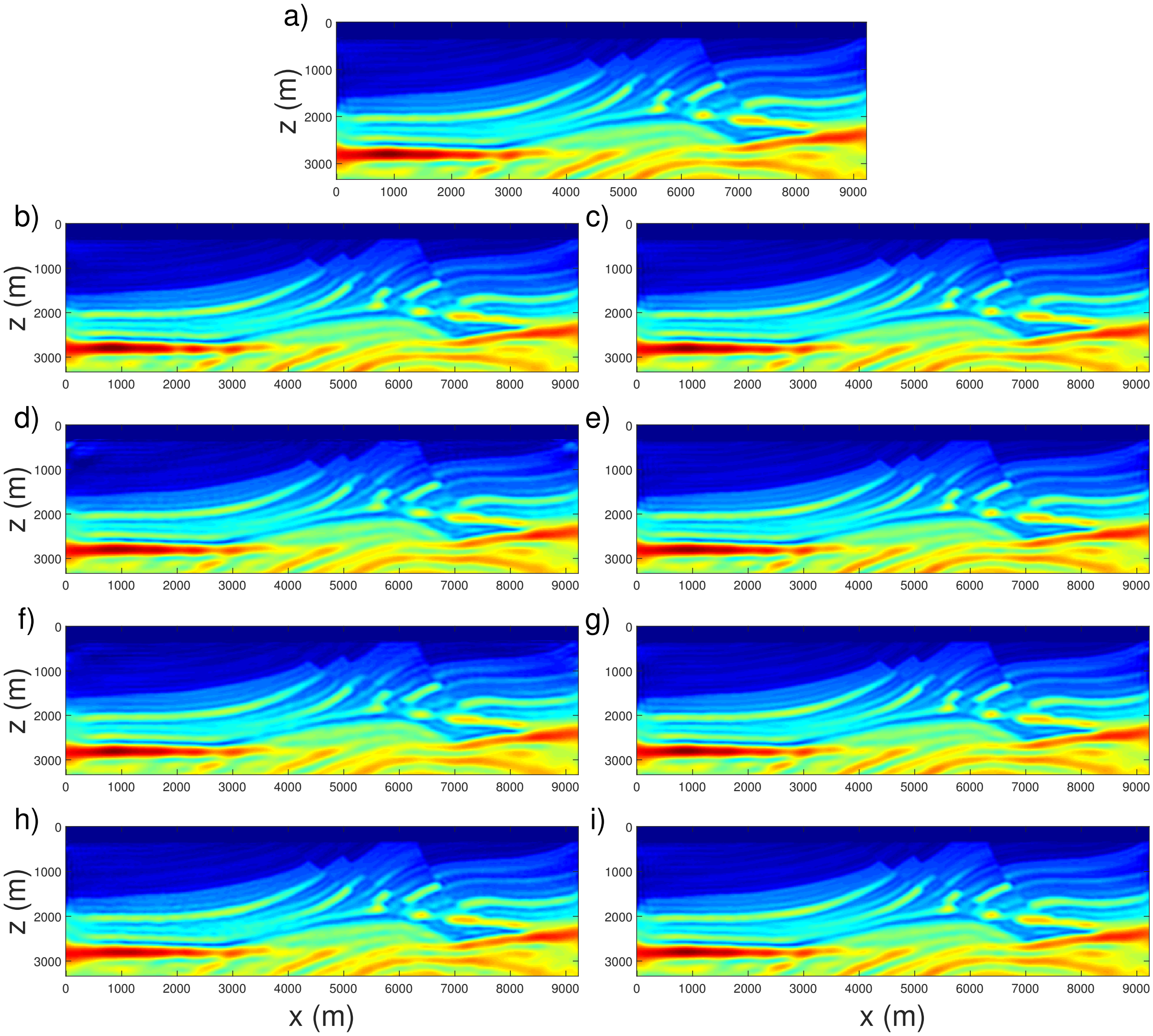

Figure 2.6: The updated velocity models after 100 iterations: a) by conventional FWI; b) and c) are by Hartley basis with 7 and 70 super-shots; d) and e) are by cosine basis with 7 and 70 super-shots; f) and g) are by sine basis with 7 and 70 super-shots; h) and i) are by random polarity basis with 7 and 70 super-shots.

As shown in Fig 2.7, we compare the data misfits in the conventional and amplitude-encoding FWI cases using 70 super-shots encoded by different bases. Note that the maximum value of data misfit we display here is 0.2. From the comparison, we can notice that using amplitude-encoding strategy, the encoding FWI experiments show very similar convergency as in the conventional case.

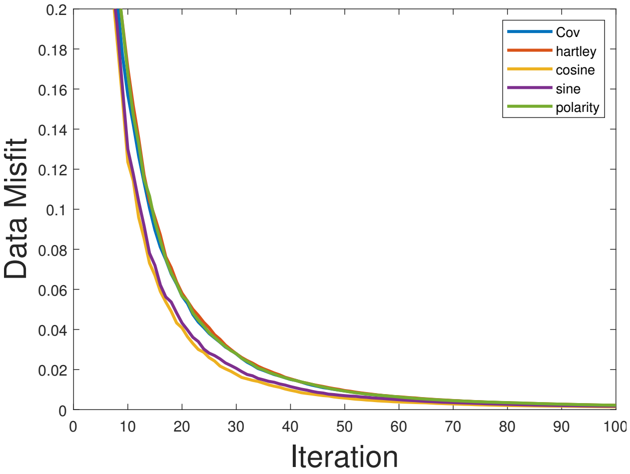

Figure 2.7: Comparison of data misfit function

To obtain ideal updated velocity models with better mitigated crosstalk noise as in the 70 super-shots cases, clearly the data dimension is not reduced enough. To further improve the calculation efficiency, we adopt the dynamic encoding concept (Krebs et al., 2009). They proposed to change the encoding sequence every iteration to avoid accumulating the crosstalk noise for better imaging quality. In our case, compared to the inversion results using 70 super-shots, we can notice the crosstalk noise in the inversion results using 7 super-shots are not significant. So instead of changing the encoding functions, we dynamically reduce the number of super-shots every a few iterations to further reduce the data dimension, hoping to achieve a better compromise between imaging quality and calculation efficiency. In our test, for the first step, we still compose the individual shot gathers into 70 super-shots and run FWI for 25 iterations, then we compose the shot gathers into 35 super-shots and run FWI for another 25 iterations using the updated velocity model by the first step. Likewise, we then use 14 super-shots and 7 super-shots for 25 iterations each. So overall, we also update the velocity model 100 times.

We present the inversion results using dynamic encoding concept after 100 iterations in Fig 2.8. When we respectively compare them with the updated velocity models using 70 super-shots in the static-encoding cases shown in the right column of Fig 2.6, we can see both encoding strategies provide almost identical inversion results and using different bases make no significant difference, but the data dimension has been further reduced.

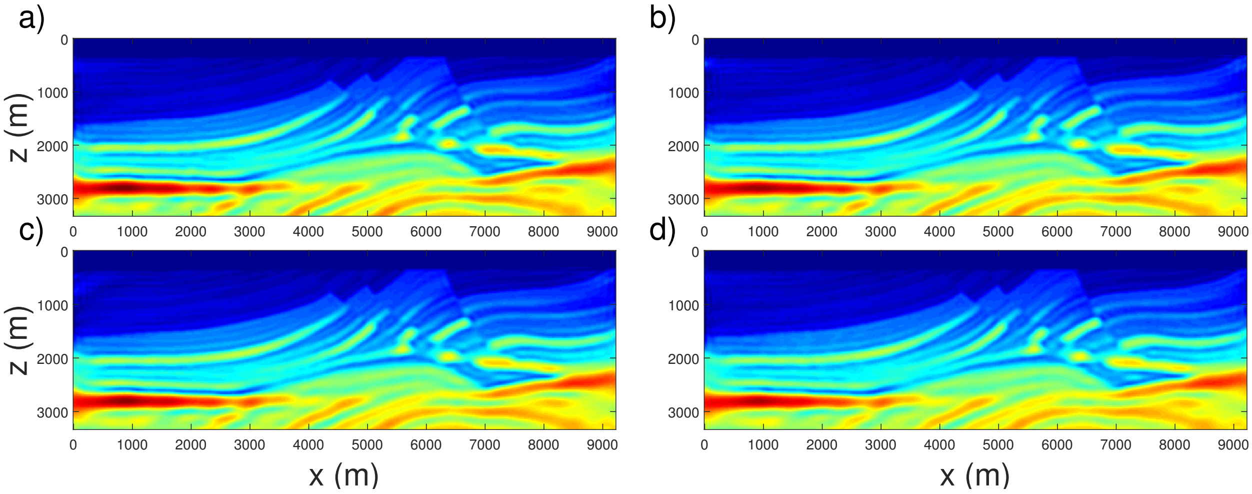

Figure 2.8: Inversions results using dynamic-encoding concept by different bases: a) Hartley; b) cosine; c) sine and d) random polarity.

The data misfit and vertical profile comparisons are shown in Fig 2.9a and b, respectively. We can see that using dynamic encoding concept can provide a very similar convergence rate as in the static encoding cases. In addition, since the number of super-shots is changed every 25 iterations, the data misfit function curves may not be smooth. Compared to the previous static case, we can notice that using Hartley and random polarity bases, when the number of super-shot is reduced during inversion process, there might be obvious "jump" in the misfit curves. While in the cosine and sine bases cases, even the super-shot number is reduced, the curves are still very smooth. From the comparison of vertical profiles in the middle of the model, we can see the lines are almost overlapped, amplitude-encoding FWI using all different 4 bases gives very good estimations of the true velocity model.

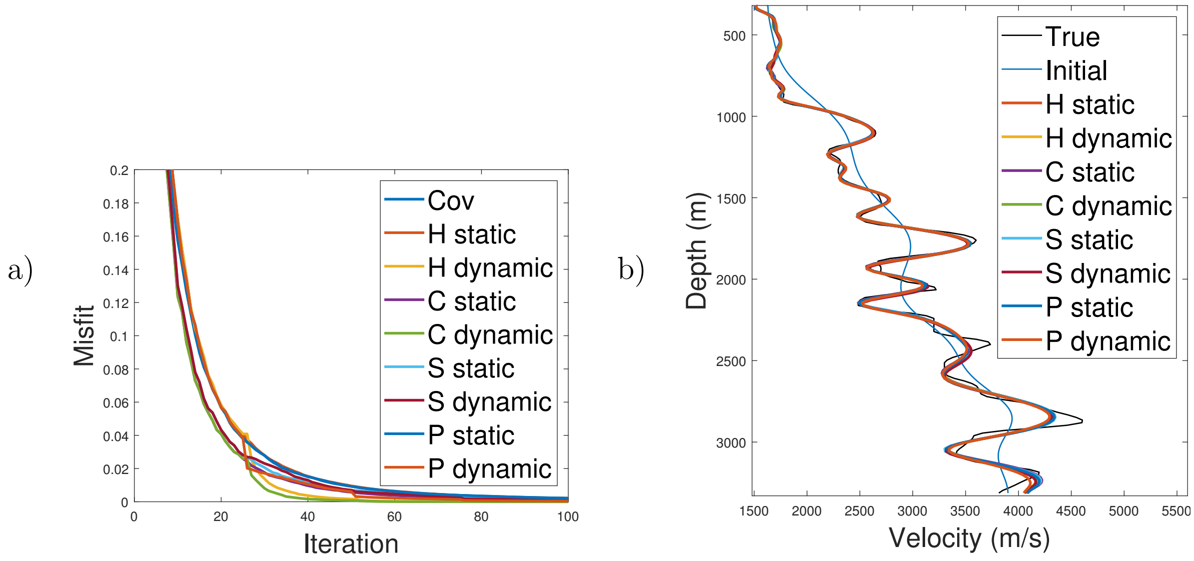

Figure 2.9: a) is the comparison of vertical profiles at distance equals to 4680 m; b) is the comparison of data misfit functions versus iteration.

2.3.2 Foothills model

To further validate the feasibility of amplitude-encoding strategy, we also used this Foothills model with a distance of 6672 m and a depth of 4000 m in a grid of 417 by 250 cells with 16 meters size each, which is shown in Fig 2.10a. We also get the initial model by smoothing the original Marmousi model, as shown in Fig 2.10b.

For this model, we generate all synthetic shot gathers for 100 sources, which are evenly distributed near the surface of true model with a spatial interval of 64 m. We deploy 417 receivers right beneath the sources with a spatial interval of 16 m. The Ricker wavelet sources are fired with a central frequency of 8 Hz. We record the seismic waveforms for 6.0 s with a time step of 1.5 ms.

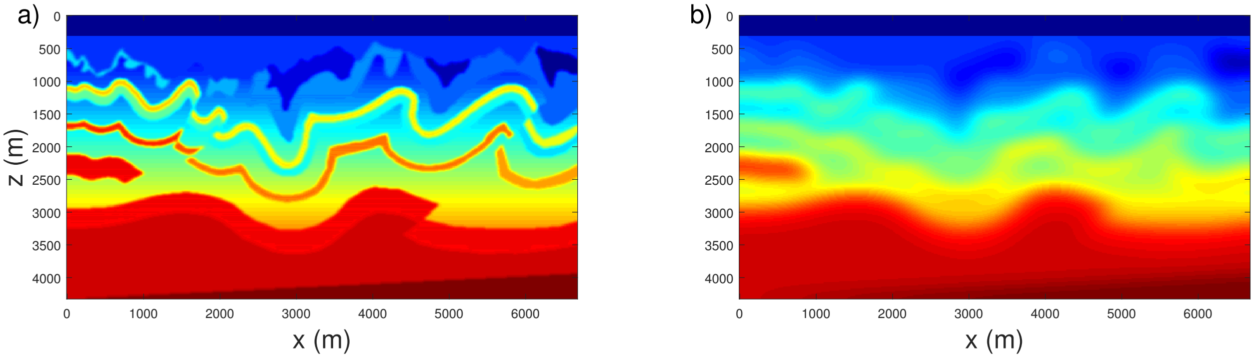

Figure 2.10: a) true Foothills model; b) initial model.

In this case, we compose the shot records into 50, 25, 10 and 5 super-shots, and also run FWI for 25 iterations each. For brevity, we only display the inversion results using dynamic encoding shown in Fig 2.11.

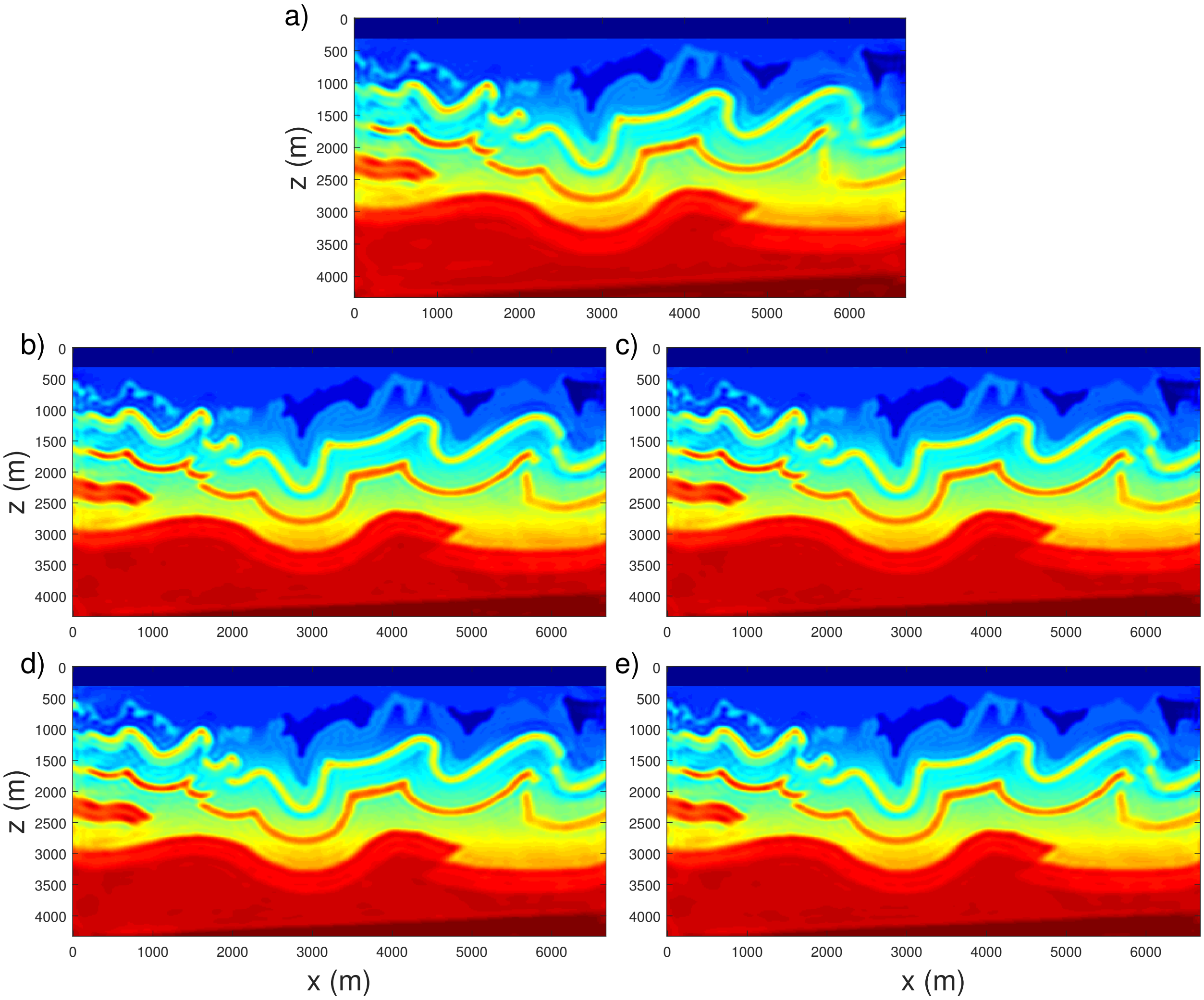

Figure 2.11: Inversion results after 100 iterations: a) by conventional FWI; Inversions results using dynamic-encoding concept by: b) Hartley basis; c) cosine basis; d) sine basis; e) random polarity basis.

For this model, FWI converges really fast, data misfits reduce to 0.1 within 10 iterations as shown in Fig 2.12. The curves for 5 cases overlapped at the first 25 iterations. We may also see the “jump” in here, just much less obvious than the Marmousi model cases.

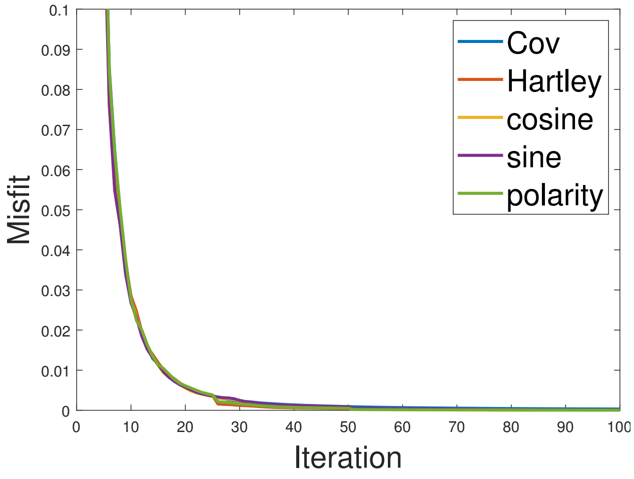

Figure 2.12: Comparison of data misfit functions versus iteration using dynamic encoding concept.

2.4 Numerical results for elastic FWI

In this section, we further apply amplitude-encoding strategy into elastic FWI. In isotropic elastic media, the first-order stress-velocity wave equation can be rewritten as:

$$\begin{aligned} \rho\frac{\partial v_i}{\partial t} &= \frac{\partial \sigma_{ij}}{\partial x_j} + f_i \\ \frac{\partial \sigma_{ij}}{\partial t} &= \lambda\frac{\partial \theta}{\partial t}\delta_{ij} + 2\mu\frac{\partial \varepsilon_{ij}}{\partial t} \\ \frac{\partial \varepsilon_{ij}}{\partial t} &= \frac{1}{2}\left(\frac{\partial v_i}{\partial x_j} + \frac{\partial v_j}{\partial x_i}\right)^2 \end{aligned} \tag{2.10}$$

where ρ is the density, σ is the stress, v is the velocity, λ and μ are Lame coefficients, and vp and vs can be expressed by

$$\begin{aligned} v_p &= \sqrt{(\lambda + 2\mu)/\rho} \\ v_s &= \sqrt{\mu/\rho} \end{aligned} \tag{2.11}$$

The objective function using l2-norm of the data misfit for elastic FWI using amplitude-encoding strategy can also be expressed as equation 2.5, exactly the same as in the acoustic case. So when the crosstalk matrix is a good approximation of the identity matrix, amplitude-encoding strategy should also work for elastic FWI in the same way. In this work, we use the IFOS2D software (Bohlen et al., 2016b) to do the experiments.

We use a subsampled Marmousi II elastic model with a distance of 3600 m and a depth of 1100 m in a grid of 360 by 110 cells with 10 meters size each. This model consists of a 200 m thick water layer above. The true and initial models are shown in Fig 2.13, we only perform FWI for vp and vs in this work.

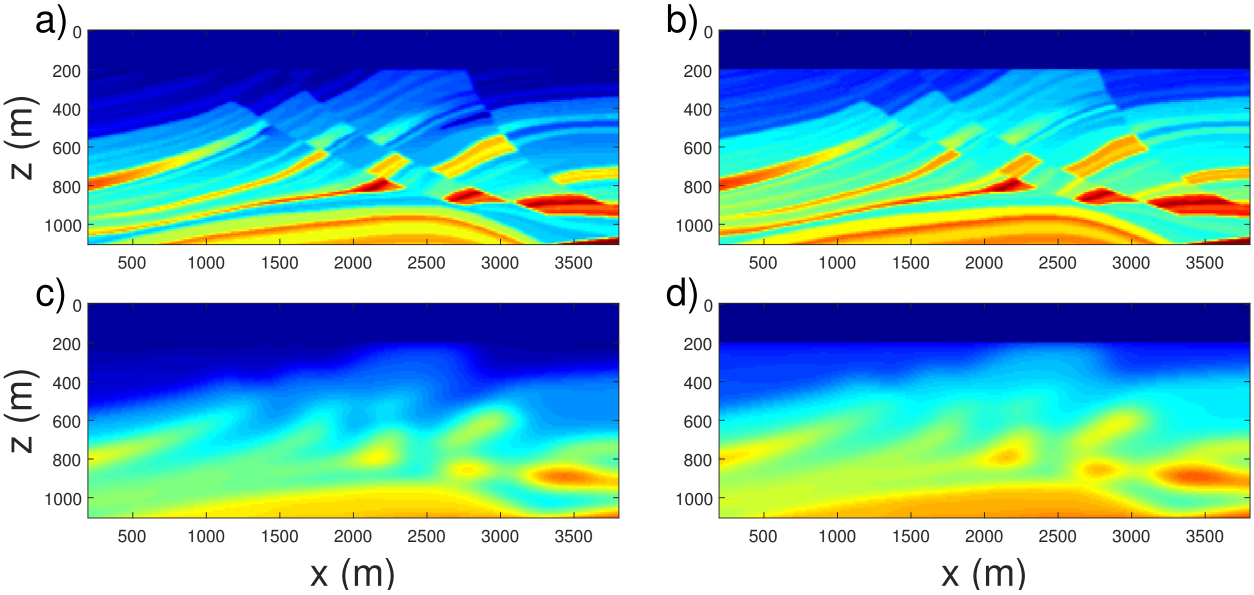

Figure 2.13: Subsampled Marmousi II model: a) and b) are true vp and vs; c) and d) are initial vp and vs.

We generate synthetic shot gathers for 40 explosive sources and deploy 360 two–component receivers. The central freq is 10 hz. The sources and receivers are at depth 20 and 30 meters, respectively.

In this experiment, we compose all 40 individual shots into 20 super-shots, the encoding and crosstalk matrices are shown in Fig 2.14.

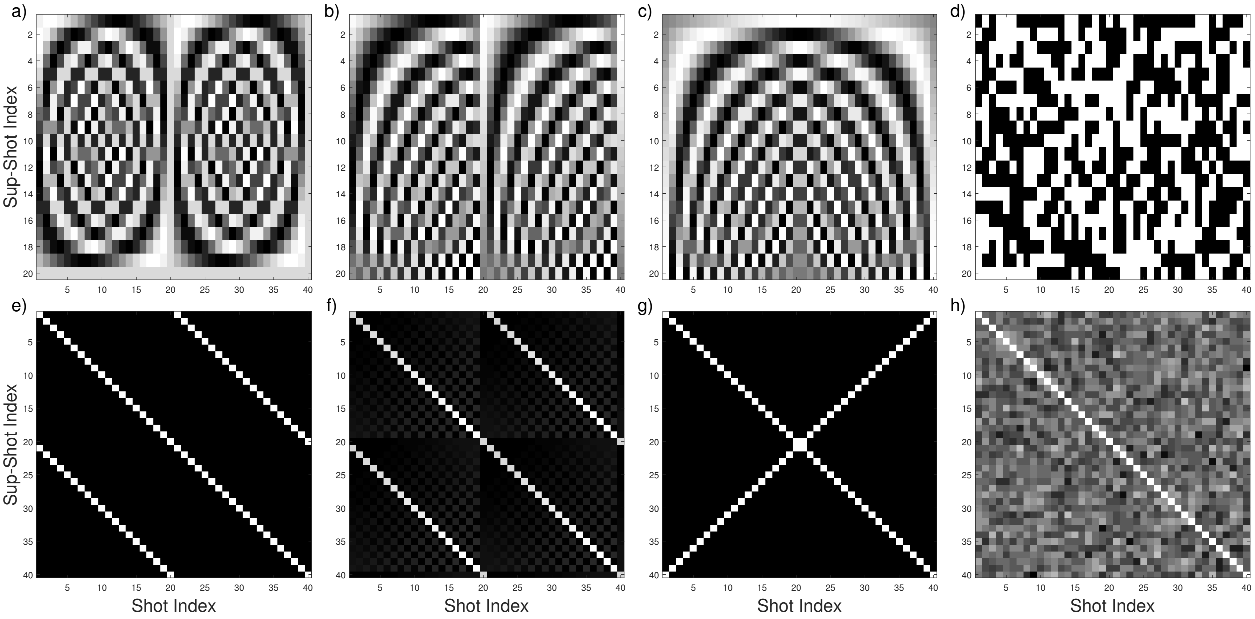

Figure 2.14: The amplitude encoding and corresponding crosstalk matrices: columns from left to right are for Hartley, cosine, sine and random polarity bases.

Also, rather than set the iteration times for our tests, we use an abort criterion to control the inversion progress, which is the defined by the relative misfit change within the last two iterations. If the relative change is smaller than one percent, the inversion stops.

The inversion results are shown in Fig 2.15. The left column are inverted vp and the right column are inverted vs models, from up to down are inverted parameters by conventional FWI, amplitude-encoding FWI using Hartley, cosine, sine and random polarity bases.

When we compare these results, we may notice there exists some minor difference among different cases. But generally, we can also see elastic FWI using amplitude-encoding strategy can also produce comparable inversion result with no obvious crosstalk noise introduced in the final images as in the acoustic cases, which further proves the feasibility of amplitude-encoding strategy for elastic FWI.

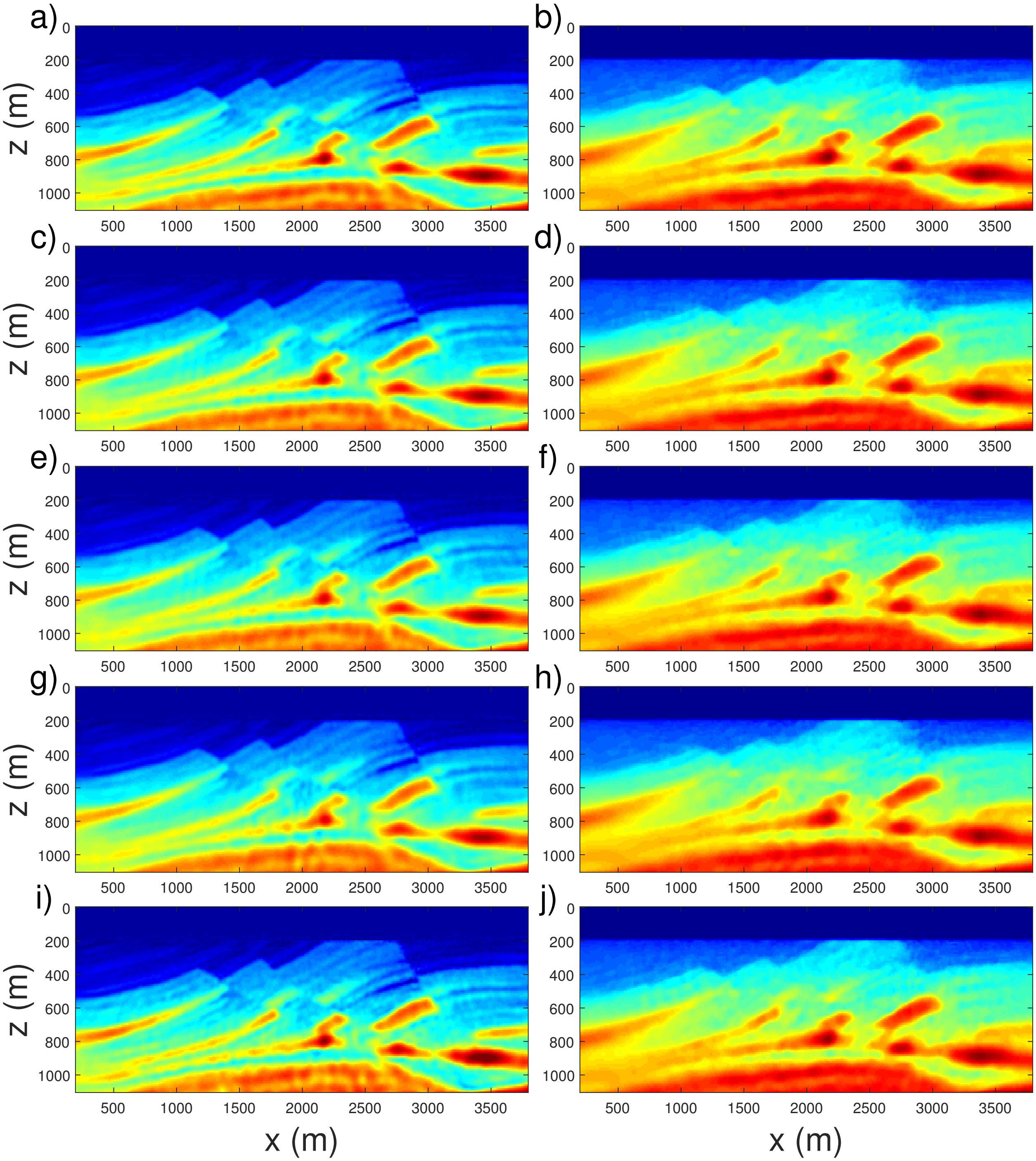

Figure 2.15: Inversion results by both conventional and amplitude-encoding FWI: left column is inverted vp, right column is inverted vs; from up to down are inverted parameters by conventional FWI, amplitude-encoding FWI using Hartley, cosine, sine and random polarity bases.

Additionally, vertical vp and vs profiles at 2.2 km of the initial model and inversion results are compared with the true model in Fig 2.16. The black line is the true model, the dashed red line is the initial model, other thicker lines are the results by amplitude-encoding strategy. The results contain a lot of small details, we can see some fine layers especially in vs model needs further improvement. However, the amplitude-encoding results are still comparable with half reduced calculation effort.

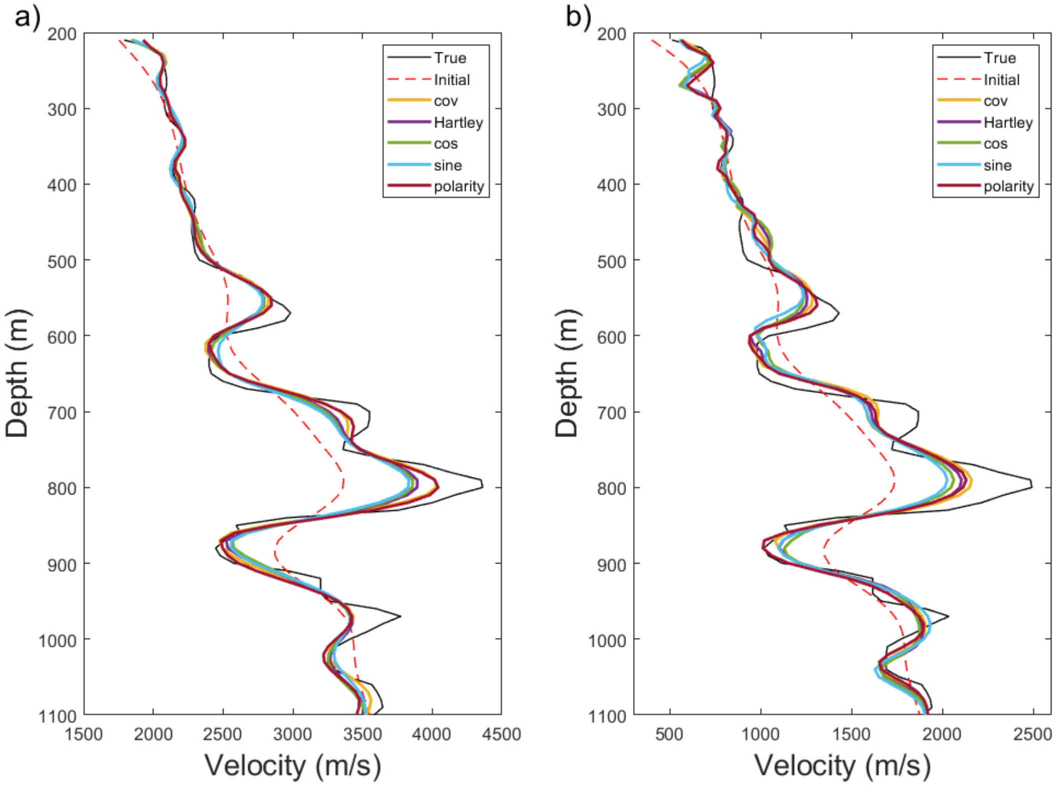

Figure 2.16: Depth profiles at distance 2.2 km of the initial model and inversion results are compared with the true model for the Marmousi II model: P-wave velocity (left), S-wave velocity (right).

2.5 Conclusions

In this work, we present the amplitude-encoding acoustic and elastic FWI using different bases as the encoding functions and compare their performance.

In our experiments, we first use Marmousi model to show that amplitude-encoding acoustic FWI using different bases can mitigate the crosstalk noise very well and produce totally comparable inverted models and convergence rate to the conventional case. Then we demonstrate the feasibility of this strategy using a Foothills model. What's also worth to notice is that, for conventional acoustic FWI, it requires N_{sig} forward model operations to generate the synthetic acoustic data. While for amplitude-encoding FWI, we can directly simulate N_{sup} super-shots without the blending stage, which also helps improve the calculation efficiency for both forward modelling and inversion process.

In addition, we adopt the dynamic-encoding concept and reduce the number of super-shots during the inversion process to further improve the calculation efficiency, producing almost the same updated velocity models as in the static-encoding cases.

We further apply amplitude-encoding strategy to elastic FWI and prove that this strategy also shows great performance for multi-parameter FWI.

Chapter 3

Multi-source time-lapse elastic full-waveform inversion using a target-oriented common-model strategy

Full-waveform inversion (FWI) is a powerful tool for time-lapse seismic analysis, enabling high-resolution imaging of subsurface physical properties to monitor reservoir changes during injection, production, and long-term CO_2 storage. However, conventional time-lapse FWI, which relies on a parallel inversion strategy, suffers from significant artifacts due to survey non-repeatability, disrupting convergence consistency between baseline and monitor inversions. Additionally, the high computational cost remains a major challenge. To address these limitations, we propose a novel time-lapse FWI strategy—the target-oriented (TO) common-model strategy (CMS)—which strategically integrates multiple approaches. Our method combines TO FWI, which enhances model convergence in the target region to improve time-lapse accuracy, with CMS, which reduces artifacts by using an optimized starting model to guide baseline and monitor inversions toward similar convergence paths. Additionally, we employ an amplitude-encoding multi-source strategy, significantly reducing computational costs without compromising inversion accuracy. Through extensive elastic tests, we validate the robustness and effectiveness of TO CMS, demonstrating superior performance over both the conventional parallel strategy and standard CMS across various challenging scenarios—including non-repeated source positions, random noise, seawater velocity variations, and biased initial models. Notably, strong noise and seawater velocity variations can significantly impact time-lapse FWI results, highlighting the need for further investigation. Ensuring consistent multi-source parameters in time-lapse FWI can help minimize artifacts. This time-lapse strategy will adopted in chapter 5.

3.1 Introduction

Time-lapse seismic analysis is widely used for monitoring subsurface property changes, for instance, the reservoir changes caused by oil/gas production or CO_2 injection (Greaves and Fulp, 1987; Ross and Altan, 1997; Wang et al., 1998; Barkved et al., 2003; Arts et al., 2004b; Barkved et al., 2005; Chadwick et al., 2009; Kazemeini et al., 2010; Pevzner et al., 2017). To enable high-resolution imaging for monitoring subsurface changes, time-lapse seismic analysis often relies on full-waveform inversion (FWI), a powerful technique that offers a detailed reconstruction of subsurface properties. FWI is a high-resolution seismic imaging technique that leverages the full information contained within seismic traces, including both amplitude and phase, to extract physical parameters of the subsurface medium probed by seismic waves (Virieux and Operto, 2009; Virieux et al., 2017; Zhang and Curtis, 2020; Operto et al., 2023), which is proposed by Tarantola (1984) in the time domain to invert the subsurface P-wave velocity model by minimizing the $l2$-norm of the difference between predicted and observed data (Symes, 2008). Pica et al. (1990) further extend FWI into elastic cases. Bunks et al. (1995) propose a multi-scale strategy to deal with the cycle skipping issue in FWI. Nevertheless, FWI continues to grapple with a significant computational workload, primarily due to its iterative and computationally intensive nature. In each iteration, the objective function's gradient must be computed concerning the model parameters, accomplished by cross-correlating the backward-propagated residual wavefield with the corresponding forward-propagated source wavefield. Calculating these two types of wave fields places significant demands on computational resources, as it involves performing a substantial number of times to solve the wave equation. For time-lapse FWI, where multiple inversions are required, the computational cost is normally double (the parallel strategy) or four times (such as the common-model strategy) of that in 2D or 3D FWI. Therefore, there is an urgent need to reduce computational complexity for time-lapse FWI.

A efficient way to reduce the computational time is source-encoding strategies (Romero et al., 2000; Krebs et al., 2009), which reduce the data dimension by encoding the individual shot gathers into super-shots. Source-encoding strategies are first introduced into pre-stack migration in the frequency domain (Morse and Feshbach, 1954; Romero et al., 2000). To date, source-encoding strategies have been used to accelerate RTM (reverse time migration), LSRTM (least-squares RTM), and FWI (Krebs et al., 2009; Dai et al., 2012; Godwin and Sava, 2013; Hu et al., 2016; Pan, 2017). Krebs et al. (2009) propose to multiply the source wavelet with a random encoding sequence of $+1$ or -1 and then blend all the shot gathers into one super-shot, but this method inevitably introduces a significant amount of noise to the final image, known as crosstalk noise (Godwin and Sava, 2013). Zhan et al. (2009) propose to compose a multi-source shot gather of a sum of single-shot gathers with random time delays, which is equivalent to using linear phase-shift as a function of frequency. This usually requires zero padding the input shot gathers along the time axis. However, the time shifts may be quite large (up to seconds) (Blacquiere et al., 2009), which increases the computational cost. Dai et al. (2012) proposed to combine these two phase-encoding strategies for LSRTM. Usually, all shots are blended into several sub-super-shots that contain all the shot records. Godwin and Sava (2013) propose an amplitude encoding strategy using the Hartley basis for wave-equation migration and compared its performance with some other source-encoding strategies. Hu et al. (2016) propose an efficient amplitude encoding strategy using a cosine basis to perform LSRTM. Amplitude encoding is based on weighting the input shot gathers instead of modifying their phase Hu et al. (2016) and can be conveniently incorporated into the time-domain wave propagator. Compared with conventional migrations, FWI is a more advanced imaging technique and has been applied successfully to various data types (Huang et al., 2021). Matharu and Sacchi (2018) demonstrate the feasibility of random polarity encoding strategy in multi-parameter FWI. We will introduce the amplitude-encoding strategy to elastic FWI (EFWI), of which the efficiency has been validated in acoustic FWI.

When FWI is used for time-lapse analysis, the most commonly used strategy is known as the parallel strategy (PRS) (Lumley et al., 2003; Plessix et al., 2010), in which the baseline and monitor models are independently inverted with the same initial model (shown in Fig. 3.1(a)), and the inverted time-lapse change is the difference between two inverted models. Due to different convergence in two independent inversions, this strategy usually introduces artifacts in the final inverted time-lapse change. Routh et al. (2012) propose to use the inverted baseline model as the initial model for the monitor model inversion to save computational time, which is known as the sequential strategy (SQS). Its target-oriented version, with a local wave-equation solver to calculate the wavefield within the target area, can be found in Huang et al. (2020). However, this strategy still doesn't cope with the artifact issue in the inverted time-lapse change, and it even enhances them since the convergence difference is widened. Watanabe et al. (2004) and Zheng et al. (2011) introduce the double-difference strategy (DDS) to address artifacts effectively. This approach allows for a more precise focus on time-lapse changes by directly utilizing the difference data (monitor data minus baseline data), corresponding to reservoir changes, during the monitoring inversion process. Zhang et al. (2012) apply the DDS for time-lapse EFWI. Zhang and Huang (2013) take the DDS a step further by incorporating a target-oriented scheme (updating the local area, including reservoir changes in the model, instead of the entire model) to enhance the effectiveness of time-lapse EFWI. For the reason of focusing on reservoir change, the DDS has become a popular strategy in field data application and numerical tests (Yang et al., 2015a, 2016; Malcolm and Willemsen, 2016). Its target-oriented version, with machine learning assistance, is presented by Li et al. (2021). Also, it is used for Bayesian/Markov Chain Monte Carlo formulation of time-lapse seismic waveform inversion (Kotsi et al., 2020; Fu and Innanen, 2022a). Nonetheless, the algebraic processes involved in DDS render it highly susceptible to acquisition nonrepeatability issues, including the non-repeatability in source/receiver locations (Zhou and Lumley, 2021b; Fu and Innanen, 2023) and source wavelets (Fu et al., 2023). Hicks et al. (2016) propose the common-model strategy (CMS), which consists of two stages of inversions, and each stage follows the same process as the PRS. In the second stage of the CMS, the inverted baseline and monitor models from the first stage are averaged as the new initial model, the workflow is shown in Fig. 3.1(b). This strategy has been adopted in field data in a North Sea field (Hicks et al., 2016) and a post-salt field in the Campos Basin (Bortoni et al., 2021). This strategy shows improved performance in mitigating artifacts and is less sensitive in the case of non-repeatability of source locations. However, all the mentioned implementations in time-lapse data are based on acoustic FWI. Hereon, we extend this CMS to time-lapse elastic FWI, and strengthen it with the target-oriented strategy. The numerical experiments performed in this study will demonstrate the effectiveness of the CMS and the newly designed target-oriented (TO) CMS for elastic time-lapse data.

Certainly, an increased emphasis is observable in endeavors to mitigate artifacts in time-lapse inversion techniques. Zhou and Lumley (2021a) propose a central-difference strategy for time-lapse FWI, which includes two SQSs with opposite data usage orders to counteract the artifacts. Fu and Innanen (2023) present a stepsize-sharing strategy, which is able to reduce the artifacts, is stable to a biased initial model, and it is of the capacity to decrease half time of seeking stepsizes when compared with the SQS. Mardan et al. (2023) devise a weighted-average approach to enhance the management of artifacts in the inverted time-lapse changes. In addition, it is also important to process time-lapse seismic data well, which can effectively reduce artifacts in time-lapse imaging or inversion. Fu and Innanen (2022b) design a source-independent matching filter to solve the source wavelet nonrepeatability issue. Attempting to encompass all methods within a single study becomes impractical due to the prohibitive computational demands. This study will center its investigation on the CMS, which has been applied in various field datasets, and the TO CMS, assessing their effectiveness in the context of time-lapse EFWI. Furthermore, we will also evaluate the PRS as the conventional methodology to have a comparison with the CMS and the TO CMS.

In this study, we develop a TO CMS for time-lapse FWI, incorporating a multi-source method. This approach leverages the advantages of TO FWI, which enhances model convergence in the target area to improve time-lapse results, and common-model time-lapse FWI, which mitigates time-lapse errors by using an optimized starting model to guide baseline and monitor inversions toward similar convergence. Both strategies help suppress artifacts in the inverted time-lapse results, while the multi-source method—an amplitude-encoding strategy—effectively reduces computational overhead by allowing multiple seismic shots to be simulated simultaneously in the FWI.

The rest of this paper is laid out as follows: in the theory section, we introduce the fundamental principles of time-domain multi-source EFWI and provide an overview of the time-lapse inversion strategies investigated in this study; the subsequent section presents the numerical examples, where we evaluate the methods across various scenarios; finally, we summarize our findings in the conclusions section.

3.2 Theory

3.2.1 Multi-source EFWI in the time domain

In a standard FWI problem, we minimize a misfit function

$$\mathbf{E}(\mathbf{m}), \tag{3.1}$$

subject to

$$\mathbf{F}(\mathbf{m})\mathbf{u}(\mathbf{x},t) = \mathbf{s}(\mathbf{x},t), \tag{3.2}$$

where $\mathbf{E}$ is a function with respect of model parameters $\mathbf{m}$, $\mathbf{F}(\mathbf{m})$ characterizes the seismic wave equation, $\mathbf{u}(\mathbf{x},t)$ denotes the particle displacement at time $t \in [0,T]$ excited by an external source $\mathbf{s}(\mathbf{x},t)$ and $\mathbf{x}$ denotes spatial coordinates. The wave equation $\mathbf{F}(\mathbf{m})$ in elastic media can be can be solved by the stagger-grid finite-difference scheme Virieux (1986); Levander (1988).

The objective function taking the least-squares norm of the misfit vector $\Delta\mathbf{u}$ is given by

$$\begin{aligned}\mathbf{E}(\mathbf{m}) &= \frac{1}{2}\Delta\mathbf{u}^{\dagger}\Delta\mathbf{u} = \frac{1}{2}\left\|\mathbf{u}_{\mathrm{obs}} - \mathbf{u}_{\mathrm{syn}}\right\|^2 \\ &= \frac{1}{2}\left(\mathbf{u}_{\mathrm{obs}} - \mathbf{u}_{\mathrm{syn}}\right)^{\mathrm{T}}\left(\mathbf{u}_{\mathrm{obs}} - \mathbf{u}_{\mathrm{cal}}\right) \\ &= \frac{1}{2}\sum_{s=1}^{N_s}\sum_{r=1}^{N_r}\int_T \left|u_{\mathrm{obs}}\left(\mathbf{x}_r,t\right) - u_{\mathrm{syn}}\left(\mathbf{x}_r,t;\mathbf{m}\right)\right|^2 \,\mathrm{d}t,\end{aligned} \tag{3.3}$$

where † denotes the adjoint operator (conjugate transpose), the data misfit $\Delta\mathbf{u}$ is defined by the differences between the observed seismic data $\mathbf{u}_{\mathrm{obs}}$ and the synthetic seismic data $\mathbf{u}_{\mathrm{syn}}$ recorded at the r-th receiver and generated by the s-th source $\mathbf{s}_s$ for model $\mathbf{m}$. N_s and N_r denote she number of sources and receivers.

Via the conjugate gradient method, the model is updated iteratively according to

$$\mathbf{m}_{k+1} = \mathbf{m}_k + \alpha_k\delta\mathbf{m}_k, \tag{3.4}$$

where k is the iteration number, α the step length, and $\delta\mathbf{m}_k$ is a search direction or descent direction and can be derived from the gradient of the misfit function.

The gradient of $\mathbf{E}(\mathbf{m})$ with respect to $\mathbf{m}, \nabla_m \mathbf{E}$, can be calculated efficiently using the adjoint-state method Plessix (2006):

$$\nabla_m \mathbf{E}(\mathbf{x}) = -\sum_{s=1}^{N_s} \int_T u^{\dagger}_{\mathrm{obs}}(\mathbf{x}, t) \cdot \frac{\partial \mathbf{F}}{\partial \mathbf{m}} u_{\mathrm{obs}}(\mathbf{x}, t)\, \mathrm{d}t. \tag{3.5}$$

where $u^{\dagger}_{\mathrm{obs}}$ is the adjoint wavefield.

In multi-source FWI, the individual shot gathers are blended into super-shots, and the encoded objective function is given by Matharu and Sacchi (2018):

$$\begin{aligned}
\mathbf{E}(\mathbf{m}) &= \frac{1}{2}\Delta\mathbf{u}^{\dagger}_{\mathrm{ms}}\Delta\mathbf{u}_{\mathrm{ms}} = \frac{1}{2}\left\|\mathbf{u}^{\mathrm{obs}}_{\mathrm{ms}} - \mathbf{u}^{\mathrm{syn}}_{\mathrm{ms}}\right\|^2 \\
&= \frac{1}{2}\left(\mathbf{u}^{\mathrm{obs}}_{\mathrm{ms}} - \mathbf{u}^{\mathrm{syn}}_{\mathrm{ms}}\right)^{\mathrm{T}}\left(\mathbf{u}^{\mathrm{obs}}_{\mathrm{ms}} - \mathbf{u}^{\mathrm{syn}}_{\mathrm{ms}}\right) \\
&= \frac{1}{2}\sum_{ms=1}^{N_{ms}}\sum_{r=1}^{N_r}\int_T \left|u^{\mathrm{obs}}_{\mathrm{ms}}(\mathbf{x}_r, t) - u^{\mathrm{syn}}_{\mathrm{ms}}(\mathbf{x}_r, t; \mathbf{m})\right|^2 \mathrm{d}t,
\end{aligned} \tag{3.6}$$

where $u^{\mathrm{obs}}_{\mathrm{ms}}$ is the blended observed data and $u^{\mathrm{syn}}_{\mathrm{ms}}$ is the blended synthetic data.

Similarly to the way to compute the gradient in standard FWI, the multi-source gradient using the adjoint-state method can be expressed as Matharu and Sacchi (2018):

$$\begin{aligned}
\nabla_m \mathbf{E}_{ms}(\mathbf{x}) &= -\sum_{s=1}^{N_{ms}} \int_T u^{\mathrm{syn}\dagger}_{ms}(\mathbf{x}, t) \cdot \frac{\partial \mathbf{F}}{\partial \mathbf{m}} u^{\mathrm{syn}}_{ms}(\mathbf{x}, t)\, \mathrm{d}t \\
&= \nabla_m \mathbf{E}(\mathbf{x}) - \underbrace{\sum_{i=1}^{N_s}\sum_{\substack{j=1 \\ j\neq i}}^{N_s} \int_T \mathbf{u}^{\dagger}_j(\mathbf{x}, t) \cdot \frac{\partial \mathbf{F}}{\partial \mathbf{m}} \mathbf{u}_i(\mathbf{x}, t)\mathrm{d}t\,.}_{\text{Cross-talk term}}
\end{aligned} \tag{3.7}$$

In this work, we used the amplitude-encoding strategy Godwin and Sava (2013); Hu et al. (2016) to compose super-shots. The individual shot gathers are blended into super-shots by

$$\mathbf{u}_{\mathrm{ms}}^{\mathrm{obs}} = \mathbf{B}\mathbf{u}^{\mathrm{obs}} \tag{3.8a}$$

$$\mathbf{u}_{\mathrm{ms}}^{\mathrm{syn}} = \mathbf{B}\mathbf{u}^{\mathrm{syn}} \tag{3.8b}$$

where the encoding matrix $\mathbf{B}$ is defined as Hu et al. (2016)

$$\mathbf{B} = \begin{bmatrix} b^{1,1} & b^{2,1} & . & b^{N_s,1} \\ b^{1,2} & b^{2,2} & . & b^{N_s,2} \\ . & . & . & . \\ b^{1,N_{ms}} & b^{2,N_{ms}} & . & b^{N_s \cdot N_{ms}} \end{bmatrix} \tag{3.9}$$

where N_{ms} is the number of the super-shots and N_s is the total number of the individual shots. Since usually N_{ms} is much smaller than N_s, the encoding FWI would achieve much better efficiency due to the reduction of data dimension. The ratio between N_s and N_{ms} is the factor by which the computational cost is reduced.

We use the sine basis as the encoding matrix, which is defined as Tsitsas (2010):

$$\mathrm{b}_{m,n} = \sqrt{\frac{2}{n_{\mathrm{s}}}} \sin\left(\frac{\left(m+\frac{1}{2}\right)\left(n+\frac{1}{2}\right)\pi}{n_{\mathrm{s}}}\right) \tag{3.10}$$

where $m = 1,\ldots,\ N_s$ is the shot-index, $n = 1,\ldots,\ N_{ms}$ is the super-shot index, and n_s is the periodization index, which we set to be half of N_s.

Then the multi-source objective function can be rewritten as:

$$\begin{aligned} \mathbf{E}(\mathbf{m}) &= \frac{1}{2}\Delta\mathbf{u}_{\mathrm{ms}}^{\dagger}\Delta\mathbf{u}_{\mathrm{ms}} = \frac{1}{2}\left\|\mathbf{u}_{\mathrm{ms}}^{\mathrm{obs}} - \mathbf{u}_{\mathrm{ms}}^{\mathrm{syn}}\right\|^2 \\ &= \frac{1}{2}\left(\mathbf{u}_{\mathrm{ms}}^{\mathrm{obs}} - \mathbf{u}_{\mathrm{ms}}^{\mathrm{syn}}\right)^{\mathrm{T}}\left(\mathbf{u}_{\mathrm{ms}}^{\mathrm{obs}} - \mathbf{u}_{\mathrm{ms}}^{\mathrm{syn}}\right) \\ &= \frac{1}{2}\left(\mathbf{u}_{\mathrm{obs}} - \mathbf{u}_{\mathrm{syn}}\right)^{\mathrm{T}}\mathbf{B}^{\mathrm{T}}\mathbf{B}\left(\mathbf{u}_{\mathrm{obs}} - \mathbf{u}_{\mathrm{syn}}\right) \end{aligned} \tag{3.11}$$

The matrix $\mathbf{B}^T\mathbf{B}$ is referred to as the crosstalk matrix. When comparing this new misfit function with equation 3.6, we can notice that when the crosstalk matrix is identical to the identity matrix, the multi-source objective function equates to the traditional objective function. Consequently, multi-source FWI, which utilizes blended data, yields identical results to conventional FWI cases. Hence, to ensure that the inversion results from encoded FWI are comparable to those from conventional FWI, it is imperative that the designed encoding crosstalk matrix closely approximates the identity matrix.

3.2.2 Time-lapse inversion strategies

Parallel strategy

In the PRS, whose workflow is shown in Fig. 3.1(a), the baseline and monitor models are independently inverted with the same initial model. Subsequently, the time-lapse model is derived by subtracting the inverted baseline model from the inverted monitor model. However, due to different convergence behaviors between these two models, this strategy often introduces artifacts in the time-lapse result.

Common-model strategy

The CMS shown in Fig. 3.1(b) consists of two stages of inversion processes. In each stage, the workflow precisely mirrors that of the PRS. After the completion of the first stage, instead of directly subtracting the inverted baseline model from the inverted monitor model, as is done in the PRS, the CMS takes a different approach. It calculates an average of the two inverted models to create a new initial model for the second stage. In this subsequent stage, FWI is performed using this new initial model along with the original baseline and monitor data as input. The final time-lapse model is then obtained by performing a subtraction operation. Serving as an enhanced version of the PRS, the CMS uses an optimized starting model to guide baseline and monitor inversions toward similar convergences. Therefore, using the CMS will result in better time-lapse result compared with the PRS. The CMS has demonstrated its ability to effectively mitigate artifacts in acoustic FWI, as evidenced by experiments conducted with both synthetic and field data Hicks et al. (2016); Fu and Innanen (2023).

Target-oriented common-model strategy

In our study, we develop a target-oriented scheme of the CMS, incorporating prior information of reservoir change locations for baseline and monitor inversions, refered to the TO CMS, the workflow is presented in Fig. 3.1(c). Similar to the CMS, the TO CMS begins by averaging the inverted baseline and monitor models derived from the same initial model. In the second stage, we assume prior knowledge of the locations of velocity change areas, and only update the model within specific regions that encompass the time-lapse areas Zhang and Huang (2013). Time-lapse FWI is usually conducted to detect the changes within a specific reservoir, such as the target reservoir for CO_2 injection and sequestration. In such a project, the location of the reservoir is known prior to the injection operation. This allows us to design the target area to update the models, making the TO CMS more feasible. Compared with the CMS, in the implementation of algorithm, the gradient outside the target area is set to zero. This combines the benefits of TO FWI Valenciano et al. (2006); Huang et al. (2020); Cui et al. (2020); Li et al. (2021); Biondi et al. (2023); Zheglova et al. (2023), which improves convergence in the target area, and common-model time-lapse FWI, which uses an optimized starting model to guide baseline and monitor inversions toward similar convergences. Both techniques reduce noise in the inverted time-lapse results.

3.3 Numerical examples

In our study, we assume a constant density and perform EFWI for Vp and Vs using the IFOS2D software Bohlen et al. (2016a). We use a down-sampled elastic Marmousi *II* model to demonstrate the efficiency of the amplitude-encoding strategy in EFWI and feasibility of the CMS and the TO CMS in time-lapse EFWI. Since the amplitude-encoding strategy is a

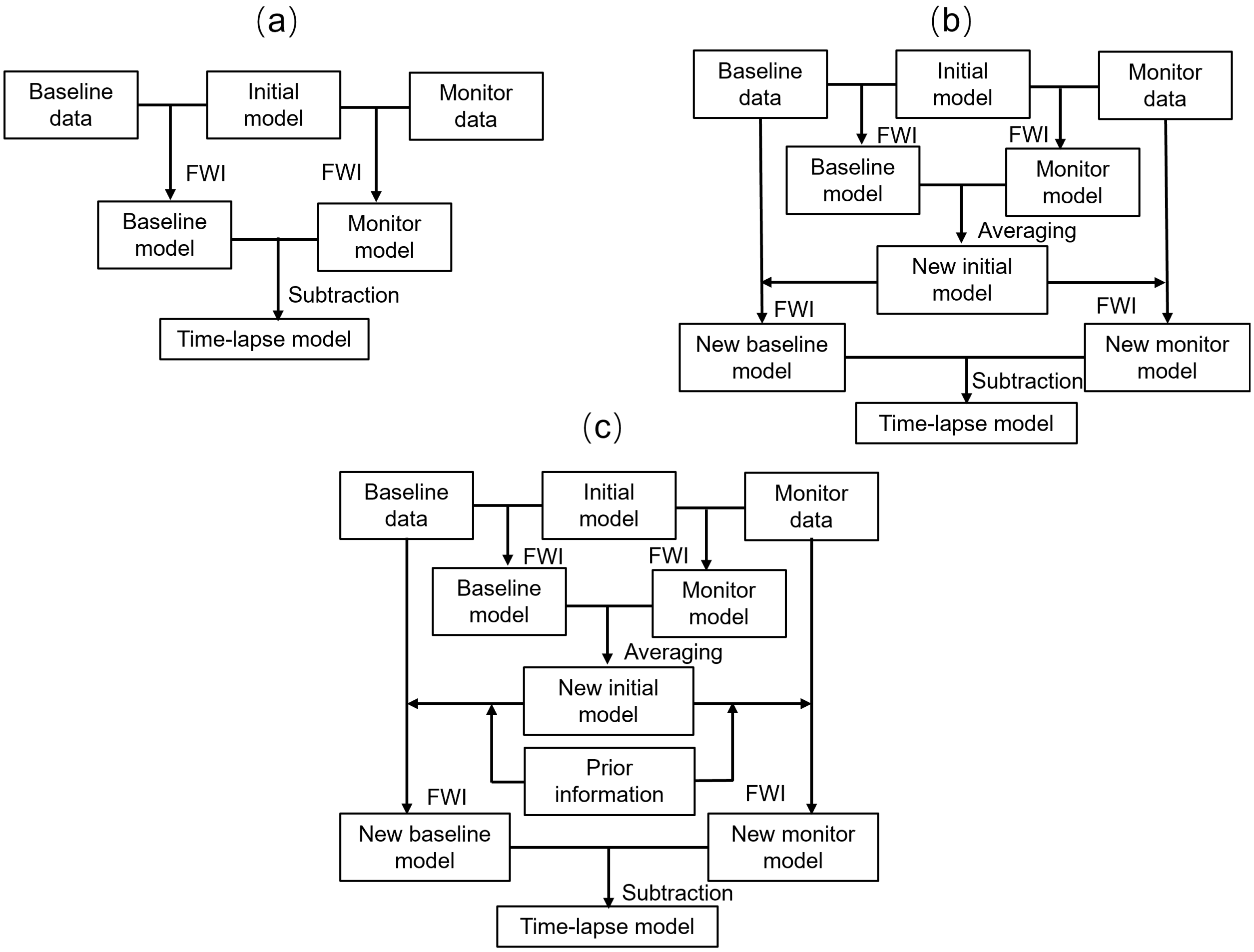

Figure 3.1: Workflows of time-lapse strategies: (a) parallel strategy (PRS), (b) common-model strategy (CMS), (c) target-oriented common-model strategy (TO CMS).

static source-encoding method, we implement it in the software to directly simulate the super-shots without the blending stage. After we achieve multi-source full-waveform inversion using the modified software, we can carry out baseline and monitor model inversions to obtain the time-lapse result using the PRS. To implement the CMS and the TO CMS, we need to use the inverted models from the previous stage to generate new initial models as inputs in the second stage inversions.

The model has a distance of 4100 m and a depth of 1500 m in a grid with a size of 410 by 150 and a 10-meter spacing. The true baseline Vp and Vs models are plotted in Figs. 3.2(a) and 3.2(b). We employ the smoothed true models as the initial models, which are plotted in

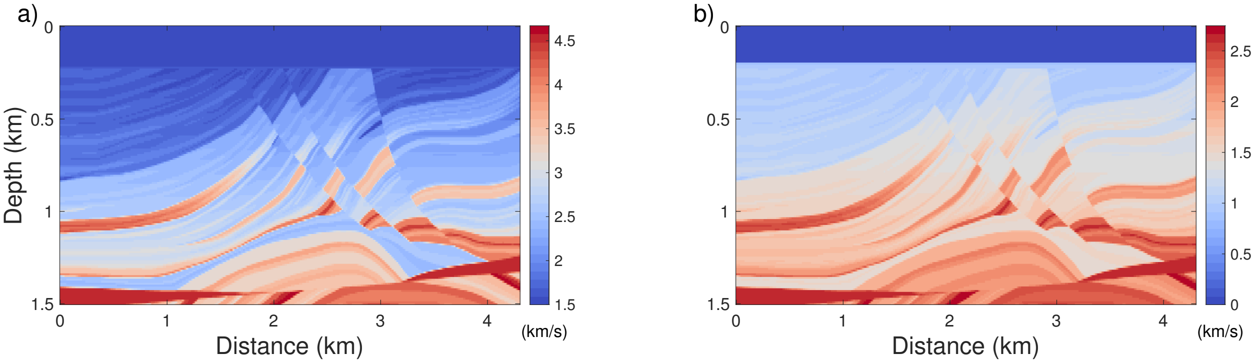

Figure 3.2: True baseline model: (a) Vp model and (b) Vs model.

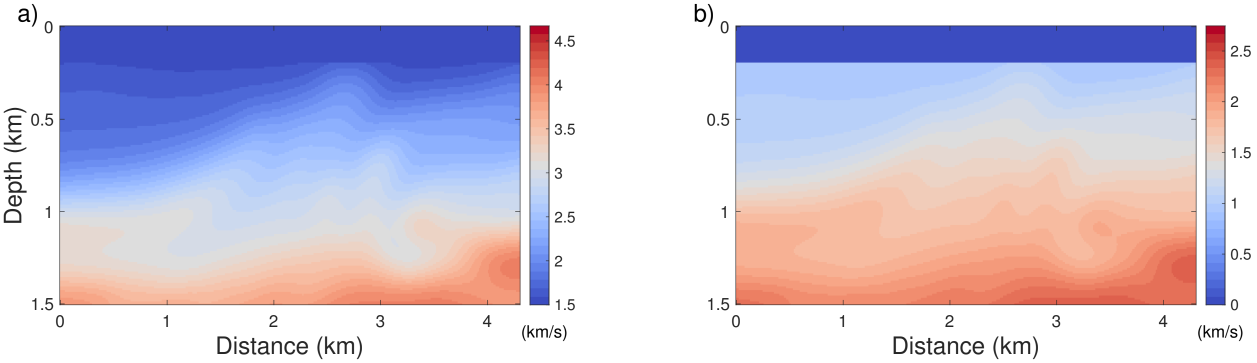

Figure 3.3: The initial baseline model: (a) Vp model and (b) Vs model.

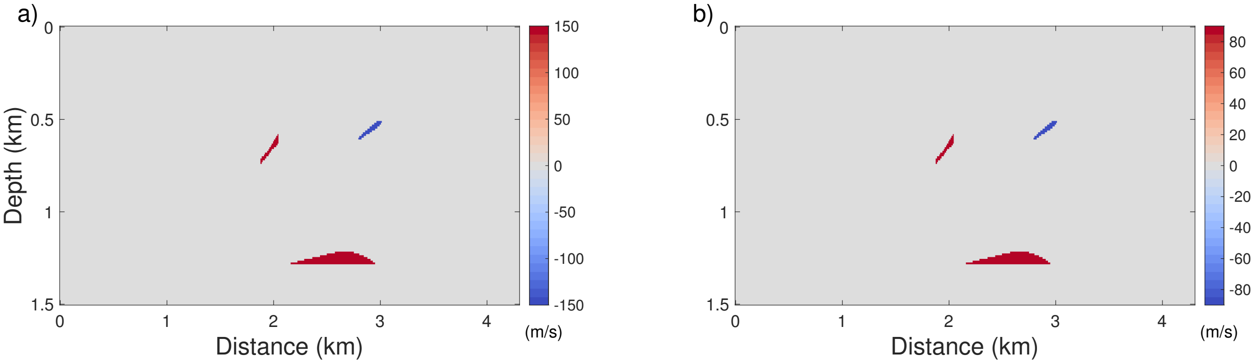

Figure 3.4: True time-lapse model: (a) Vp model and (b) Vs model.

Figs. 3.3(a) and (b). There is a 200 m-thick water layer at the top of the model. The free surface condition Levander (1988) is implemented on top of the model. There are 20 layers of Perfectly Matched Layers (PMLs) Komatitsch and Martin (2007) implemented around the other sides of the model as the absorbing boundary condition in the finite difference modeling.

For the time-lapse survey, three velocity change areas, plotted in Fig. 3.4, are added to the baseline model to have the monitor model. The Vp changes in area 1 (top left), area 2 (top right) and area 3 (bottom) are set to +150, -150 and +150 m/s, respectively. Accordingly, the Vs changes in these 3 areas are set to +90, -90 and +90 m/s. Areas 1 and 2 are located at shallower depths with relatively lower background velocities, while the area 3 is located at large depth with a relatively higher background velocity.

We deploy evenly distributed 80 sources and 410 receivers along the surface at depths of 20 m and 30 m, respectively. The horizontal source location starts from 80 m and the source location interval is 50 m, and the receivers are located at every grid cell. The source wavelets adopted for both baseline and monitor datasets are identical, which is a Riker wavelet with a dominant frequency of 10 Hz. The time sampling interval is 1.25 ms and the maximum recording time is 3 seconds. Moreover, in the EFWI, a multi-scale approach Bunks et al. (1995) is incorporated to mitigate the cycle skipping problem.

3.3.1 Multi-source EFWI

To illustrate the capacity of the multi-source strategy in EFWI, the inversion results of the baseline model using the multi-source FWI are compared with that using the conventional FWI in which the shot gathers are calculated individually. In the conventional EFWI process, 80 synthetic individual shot gathers are generated by using the true baseline model as the observed data and solving the first-order elastic wave equations Virieux (1986); Levander (1988). In the multi-source EFWI experiment, we use the amplitude-encoding strategy to assign the encoding weights to all the individual shot gathers to compose 10 super-shots. In conventional FWI, the encoding and crosstalk matrices are identity matrices, while in multi-source FWI, the encoding and crosstalk matrices are plotted in Fig. 3.5. In both experiments, the computations were carried out on a workstation equipped with an Intel i7-7800X CPU and 64 GB of RAM. The programs were parallelized using MPI with 5 processors. The memory usage in each experiment was approximately 2.19 GB. In Fig. 3.6, we plot an

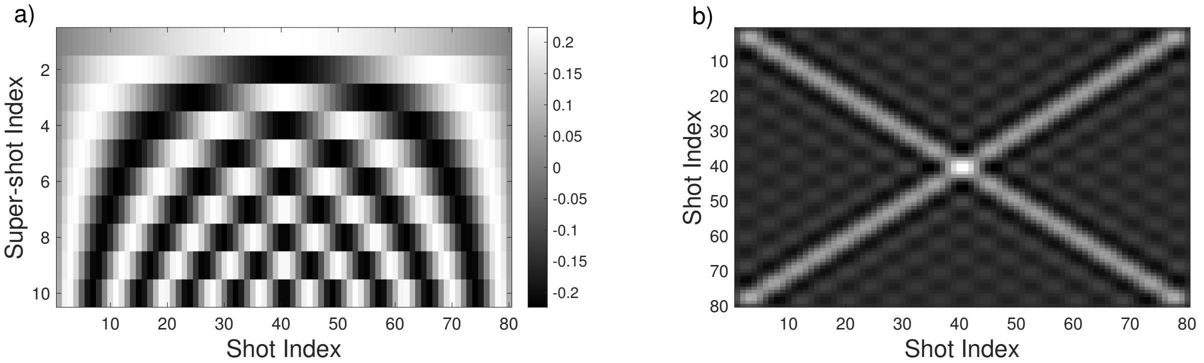

Figure 3.5: (a) The encoding matrix and (b) the crosstalk matrix.

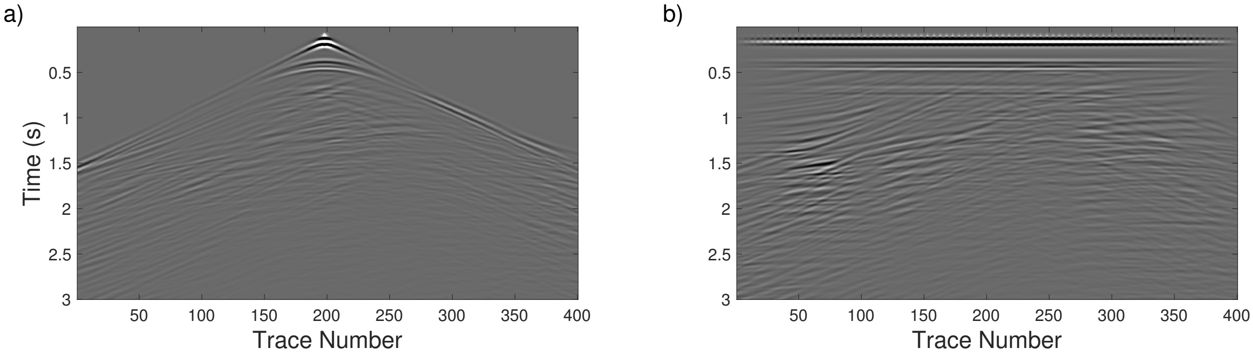

Figure 3.6: Synthetic data: (a) a shot near the center of the model in conventional FWI; (b) the first super-shot in multi-source FWI.

individual central shot and the first encoded super-shot, respectively, used in conventional and multi-source EFWI's.

In Fig. 3.7, the inverted baseline models from both conventional and multi-source EFWI's are plotted, and which shows that the multi-source EFWI can produce high-quality inversion results with acceptable crosstalk noise introduced in the final images. In Fig. 3.8, extracted traces from the results in Fig. 3.7 at distances of 2.08 km, 3.0 km, and 2.68 km, respectively, are plotted, which can well match the true values. In Fig. 3.9(a) and 3.9(b), the normalized model misfits (L1-norm) of conventional and multi-source EFWI are plotted. We observe that both inversions have nice model convergences, and the conventional EFWI has a lower model misfit since there is no impact of data crosstalk. We also observe that the data misfits shown in Fig. 3.9(c) for both methods converge well and reach a similar level. The efficiency comparison between the conventional and multi-source EFWI's is illustrated via table 3.1,

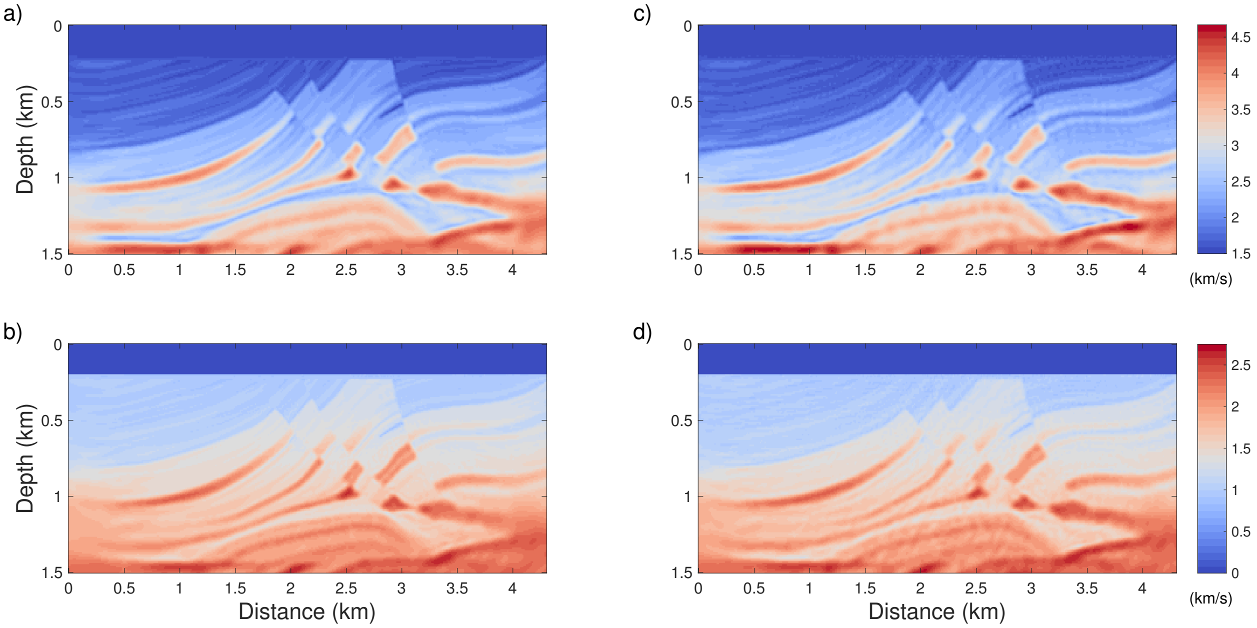

Figure 3.7: Inverted baseline model, (a) Vp and (b) Vs models using conventional FWI; (c) Vp and (d) Vs models using multi-source FWI.

Table 3.1: Averaged calculation time for conventional FWI and encoding-FWI per iteration.

	Conventional FWI (80 shots)	Encoding-FWI (10 super-shots))
Calculation time (s)	968	122

where their average CPU times for each iteration are displayed. It shows that the speed-up ratio for encoding-FWI is approximately the number of individual shots over the number of super-shots.

Since we have demonstrated that the multi-source EFWI can achieve high-quality elastic inversions, in the following tests, we will only adopt the amplitude-encoding EFWI to perform the time-lapse EFWIs using three time-lapse inversion strategies, including the PRS, the CMS, and the TO CMS. In the TO CMS, to lower the practical difficulty of locating three reservoir changes, we treat all three velocity change areas as a whole and update a local region that contains all the changes.

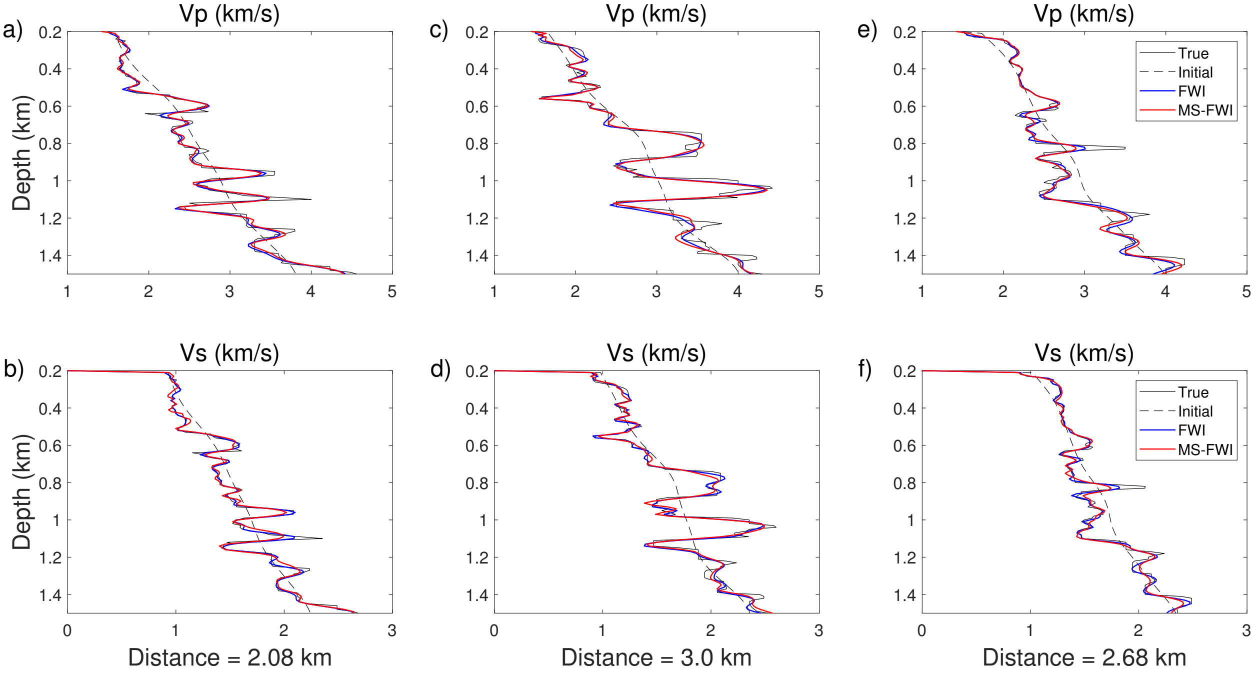

Figure 3.8: Extracted traces of Vp and Vs within 3 reservoir areas extracted at distances 2.08 km, 3.0 km and 2.68 km: the first row are P-wave velocities, the second row are S-wave velocities.Within each panel, the black solid line is the true model, and the black dashed line is the initial model, the blue line is the result of conventional EFWI, and the red line is the result of multi-source EFWI.

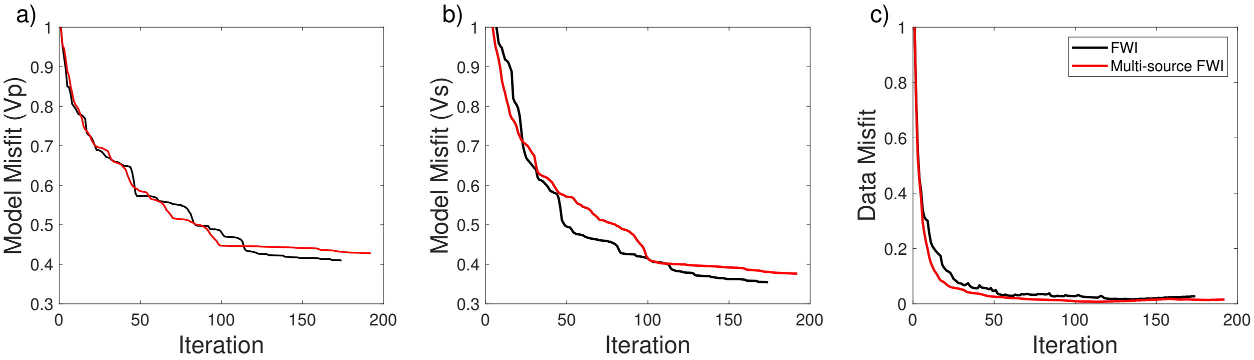

Figure 3.9: Model misfits and data misfit versus iteration of both FWI and multi-source FWI: (a) Vp model misfit, (b) Vs model misfit, and (c) data misfit.

3.3.2 Marmousi model

Noise-free data tests

In this subsection, noise-free datasets with perfectly repeatable acquisition geometries are employed. The first super-shot of the monitor data and the difference between the first super-

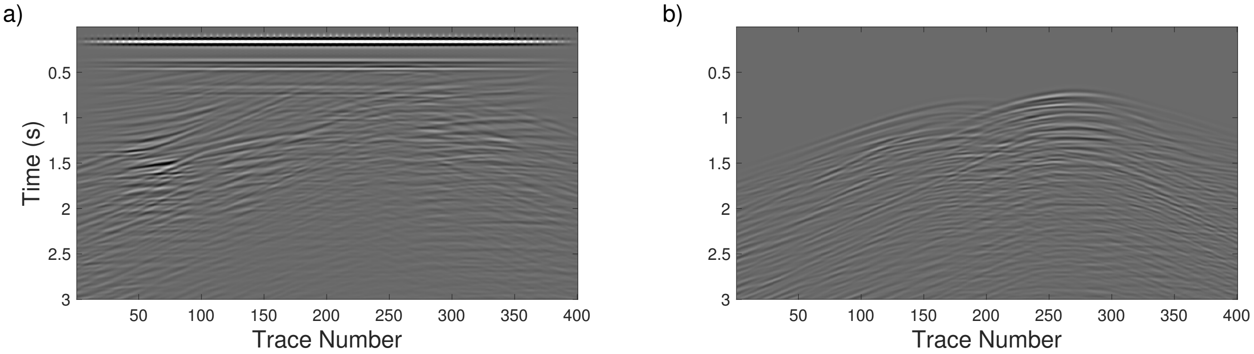

Figure 3.10: Noise-free synthetic data: (a) the first super-shot in the monitor survey; (b) the difference of first super-shots in monitor and baseline surveys.

shots of the monitor and baseline data are plotted in Figs. 3.10(a) and (b), respectively. The results of different time-lapse strategies are plotted in Fig. 3.11. We observe that the PRS gives the worst results, in which artifacts become more noticeable with the increase of depth since the deeper part has worse model convergence. Compared with the PRS, the CMS and the TO CMS can provide results with significantly fewer artifacts. The inverted velocity changes of the TO CMS have better model convergence than that of the CMS. The inverted Vp changes are better than the inverted Vs changes. The same conclusions can also be drawn from Figs. 3.12(a) to (f), where the traces, extracted at distances 2.08 km, 3.0 km, and 2.68 km from the results in Figs. 3.12(a) to (f), are plotted, respectively. In this section, a total of six times of elastic FWI are performed. In the following sections, the situation is similar, which is very time-consuming and makes adopting the multi-source strategy necessary for computational feasibility.

Different encoding functions

In this section, to analyze the effect of encoding function in time-lapse inversion, different encoding functions are adopted to invert the baseline and monitor models. In this case, we used the Hartley basis as the encoding function to invert monitor model, which is defined as

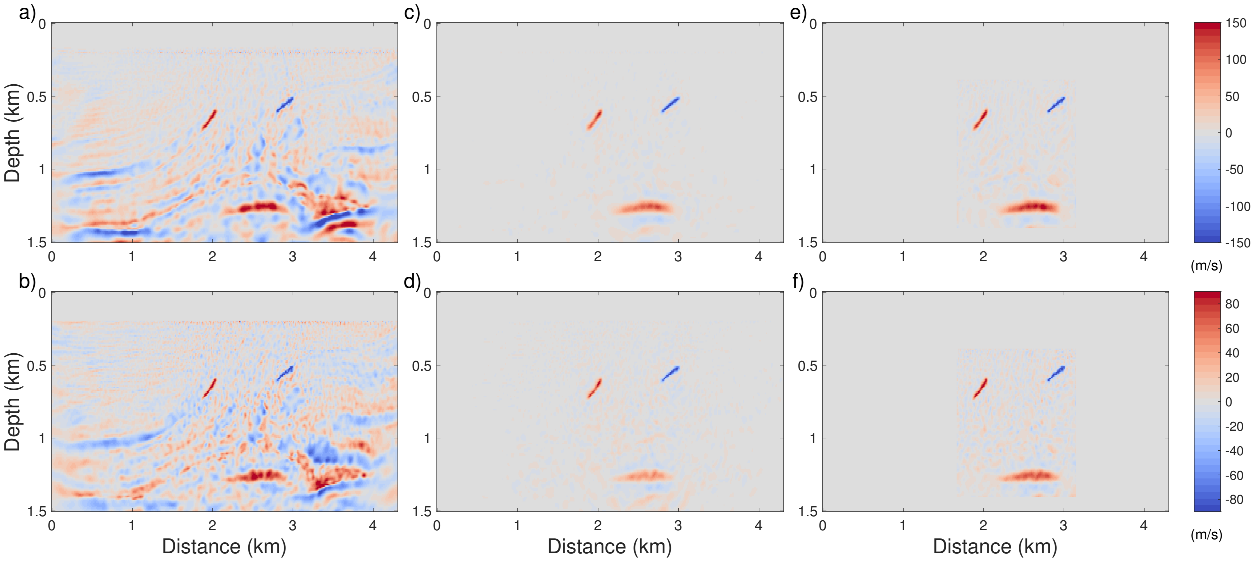

Figure 3.11: Tests with perfectly repeated surveys and source encoding methods. The time-lapse results of different strategies, in the case baseline and monitor inversions use noise-free data: (a) and (b) are Vp and Vs using the parallel strategy (PRS), (c) and (d) are Vp and Vs using the common-model strategy (CMS), (e) and (f) are Vp and Vs using the target-oriented common-model strategy (TO CMS). The PRS introduces noise into the time-lapse result, the CMS and the TO CMS can provide results with significantly fewer artifacts.

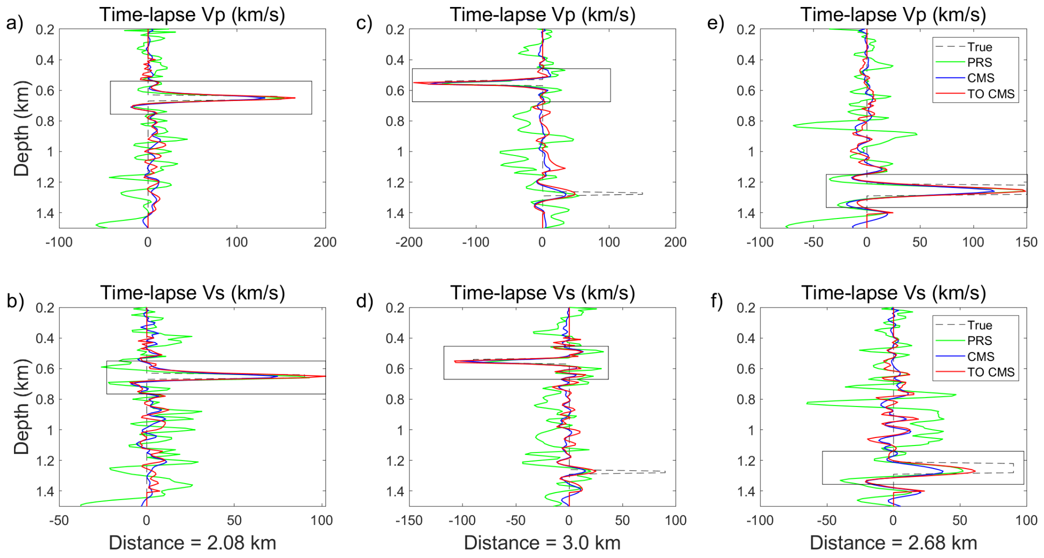

Figure 3.12: Extracted traces of inverted time-lapse results of different strategies, in the case baseline and monitor inversions use the same source-encoding methods, data are noise-free with perfectly repeated acquisition geometry: (a) and (b) are time-lapse Vp and Vs at distance 2.08 km, (c) and (d) are time-lapse Vp and Vs at distance 3.0 km, (e) and (f) are time-lapse Vp and Vs at distance 2.68 km.

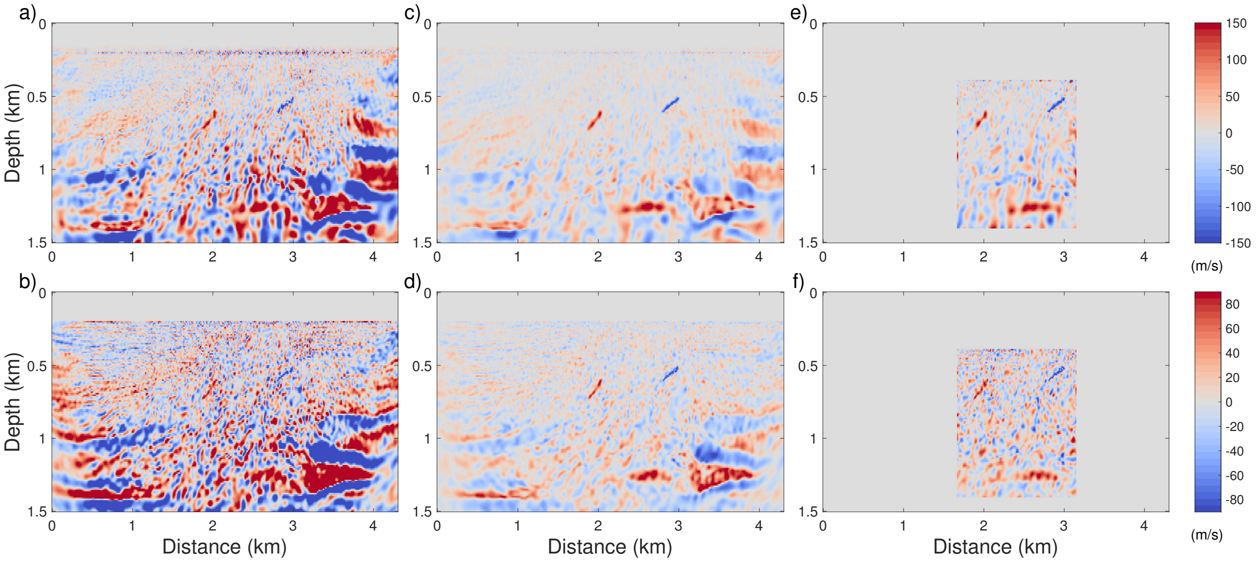

Figure 3.13: Tests with non-repeated source-encoding methods. The time-lapse results of different strategies, in the case baseline and monitor inversions use noise-free data with perfectly repeated acquisition geometry: (a) and (b) are Vp and Vs using the PRS, (c) and (d) are Vp and Vs using the CMS, (e) and (f) are Vp and Vs using the TO CMS. Different encoding functions in baseline and monitor inversions introduce noise into the time-lapse results.

Tsitsas (2010); Godwin and Sava (2013):

$$b_{m,n} = \cos\left(\frac{2\pi mn}{n_{\mathrm{s}}}\right) + \sin\left(\frac{2\pi mn}{n_{\mathrm{s}}}\right) \tag{3.12}$$

where the parameters are defined in the same way as in equation 3.10.

In Fig. 3.13, we compared the results by 3 time-lapse strategies. In the first column, we can see using the PRS, we can't identify all the velocity change areas. While in the results by the CMS and TO CMS, we can identify area 1 and area 2. As for area 3, none of the time-lapse strategies can recover the velocity change. Since the encoding function is repeatable in a time-lapse survey, in the following sections, we used the same encoding functions to invert baseline and monitor models.

Different number of super-shots

In this section, to analyze the impact of super-shot number on time-lapse inverison, the baseline data are still blended into 10 super-shots, while the monitor data are blended into 6 and 14 super-shots respectively. In Figs. 3.14 and 3.15, the inverted time-lapse results in two cases are displayed. Compared with results in the section where the same number of super-shots are used in both baseline and monitor inversions, in the case when 6 super-shots are used in monitor inversion, much more artifacts are introduced in the time-lapse images shown in Fig. 3.14. In the case when 14 super-shots are used in monitor inversion shown in Fig. 3.15, the time-lapse images are also degraded, but the quality are still better than those in the first case. Due to the enhanced convergence using more super-shots in the monitor inversion, it results in stronger time-lapse changes as well as stronger noise. The comparison of results from the last three sections shows that both different encoding functions and different numbers of super-shots in baseline and monitor inversions introduce significant noise into the time-lapse results. When employing the multi-source strategy, we recommend composing baseline and monitor data into super-shots in the same way to achieve more reliable time-lapse FWI outcomes.

Non-repeatable random noise

In this section, we performed time-lapse inverison using noisy datasets with a perfectly repeatable acquisition geometry. We added the same level of Gaussian random noise with different implements to the noise-free baseline and monitor data to obtain noisy data. In Figs. 3.16(a) to (c), the first super-shots of noisy baseline data with SNR (signal-to-noise ratio) $= 20, 10$ and 5. In Figs. 3.16(d) to (f), we display the corresponding differences between noisy monitor and baseline data with SNR$= 20, 10$ and 5 (the amplitudes are magnified by a factor of 10).

In Fig. 3.17, the inverted baseline models using noisy data with different levels of SNR are plotted. In Figs. 3.18 to 3.20, we plot the corresponding time-lapse inversion results

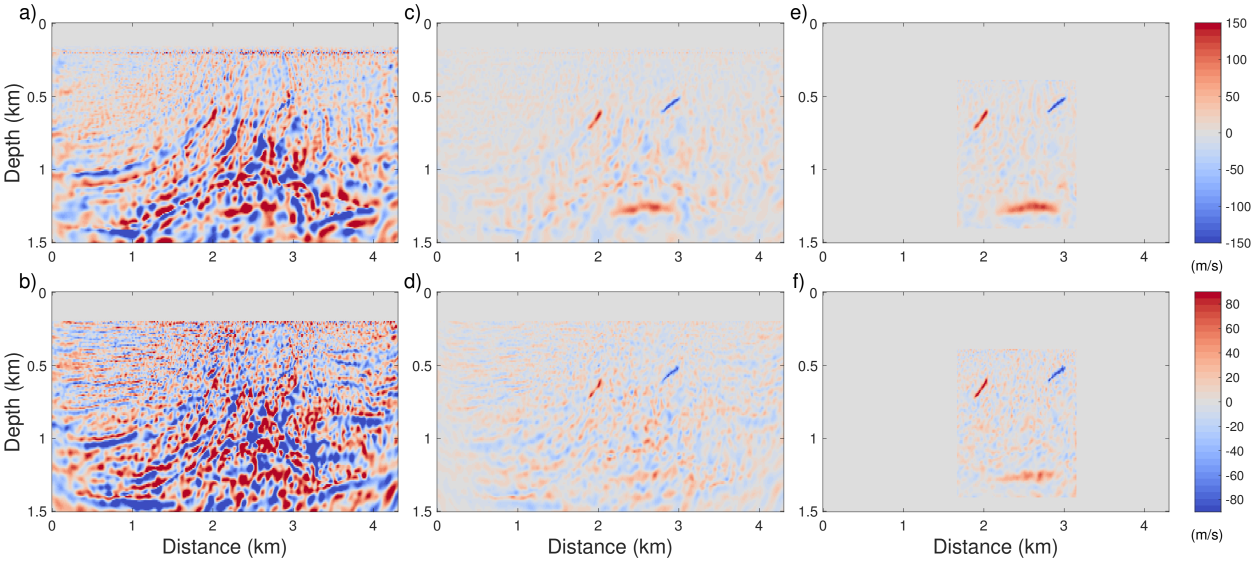

Figure 3.14: Tests with non-repeated source-encoding parameters. The time-lapse results of different strategies, in the case baseline inversion uses 10 super-shots and monitor inversion uses 6 super-shots using the same source-encoding function, data are noise-free with perfectly repeated acquisition geometry: (a) and (b) are Vp and Vs using the PRS, (c) and (d) are Vp and Vs using the CMS, (e) and (f) are Vp and Vs using the TO CMS. Different number of super-shots in baseline and monitor inversions introduce noise into the time-lapse results.

using three time-lapse strategies. From the results, we can see that with an increasing level of Gaussian random noise, the time-lapse results tend to be more noisy. And the inversion of the deeper time-lapse change is worse than those of the sallow ones, since the corresponding reflections are weaker. The PRS still provided results with strong artifacts, and the CMS and the TO CMS perform much better than it. From the results of the CMS and the TO CMS, we observe that all Vp changes can be identified, even when SNR is as low as 5, but for Vs, the deep reservoir change can not be recognized when SNR equals either 10 or 5. The TO CMS still generates more accurate results than the CMS.

Non-repeatable source positions

In this section, we consider how the non-repeatable source positions affect the time-lapse inversion results using different time-lapse strategies. We use noise-free datasets, but the acquisition geometries for baseline and monitor surveys are different. In this work, we only

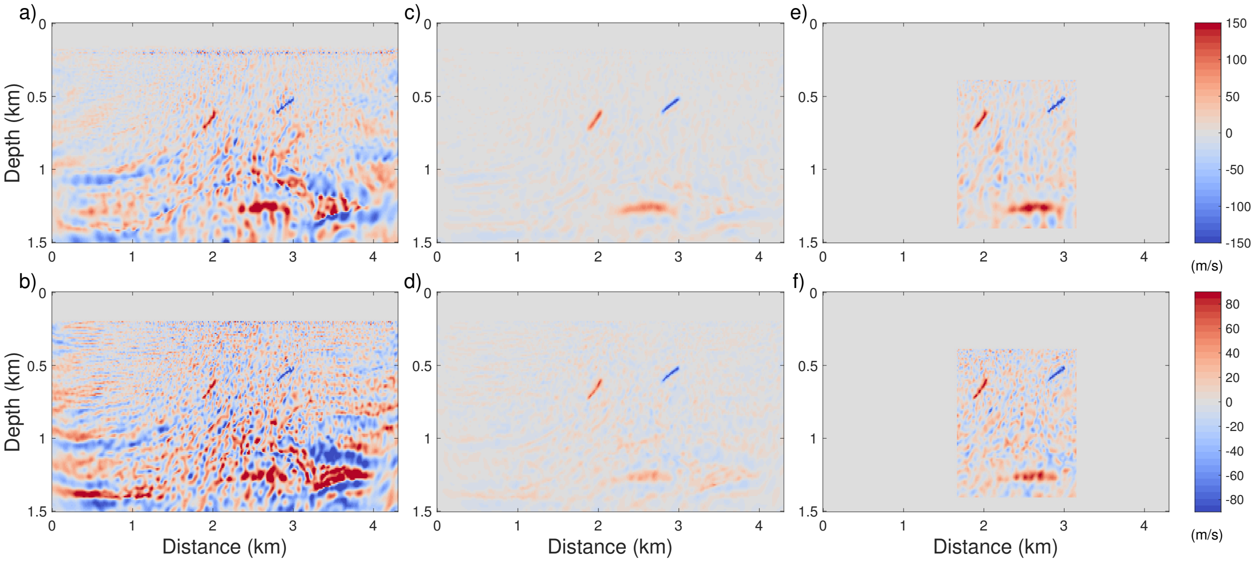

Figure 3.15: Tests with non-repeated source-encoding parameters. The time-lapse results of different strategies, in the case baseline inversion uses 10 super-shots and monitor inversion uses 14 super-shots using the same source-encoding function, data are noise-free with perfectly repeated acquisition geometry: (a) and (b) are Vp and Vs using the PRS, (c) and (d) are Vp and Vs using the CMS, (e) and (f) are Vp and Vs using the TO CMS. Different number of super-shots in baseline and monitor inversions introduce noise into the time-lapse results.

consider the impact of source position non-repeatability on different time-lapse strategies, and receivers are still deployed in each grid cell of the model and kept fixed. To analyze the effects of non-repeatable source positions, we consider three different cases. In cases 1 and 2, the source locations in the baseline model remain the same as in previous sections, the first source locations in monitor survey are, respectively, 10 m and 20 m larger than that in baseline survey. In case 3, we consider an extreme scenario, the source locations in baseline model are also changed, and shifted to left, the first source location starts from a distance of 20 m. In the monitor model, the source locations are still shifted to right, and the first source location starts from a distance of 140 m. In this case, the minimum source location distance between baseline and monitor surveys are also 20 m as in case 2 , but the difference between two acquisition geometries in both surveys are bigger. In the froward simulation of monitor model inversion, the shifted source positions which are non-repeatable from the baseline model are used.

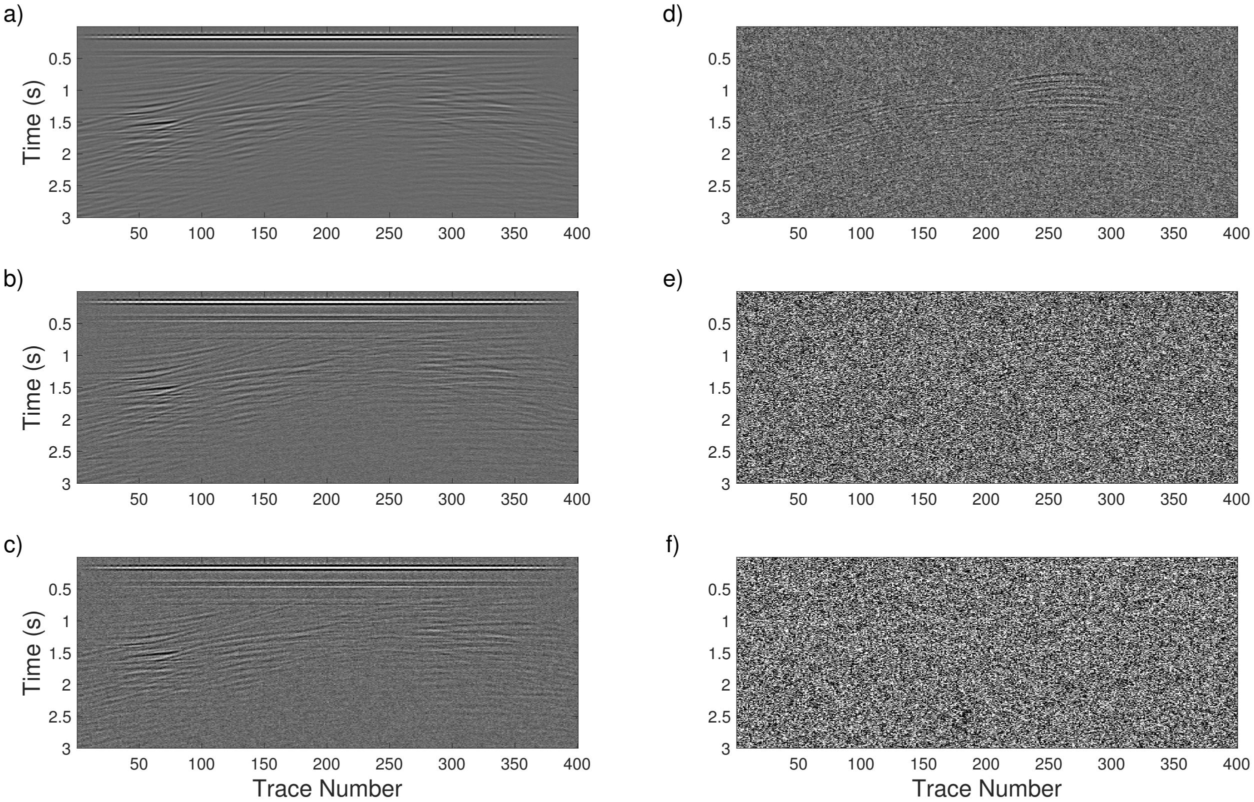

Figure 3.16: Synthetic data: (a), (b) and (c) are the first super-shots of noisy baseline data with SNR=20, 10 and 5, (d), (e) and (f) are the differences between noisy monitor and baseline data with SNR=20, 10 and 5 (the amplitudes are magnified by a factor of 10).

In Figs. 3.21, 3.22 and 3.23, the inverted time-lapse results in three cases are plotted. From these results, we observe that the PRS is sensitive to the source position non-repeatability and gives the worst results, especially in case 3, the time-lapse changes are totally submerged in artifacts. In case 3, we observe that the CMS and TO CMS provide similar results, while in case 1 and case 2, the TO CMS can recover more accurate values for the deeper velocity change.

Non-repeatable seawater velocity change

In a time-lapse survey, the seawater velocity may change, and it seriously affects the recovery of underground velocity change. In this section, we consider the overburden water velocity change. Three cases are considered, in the first two cases, the maximum water velocity

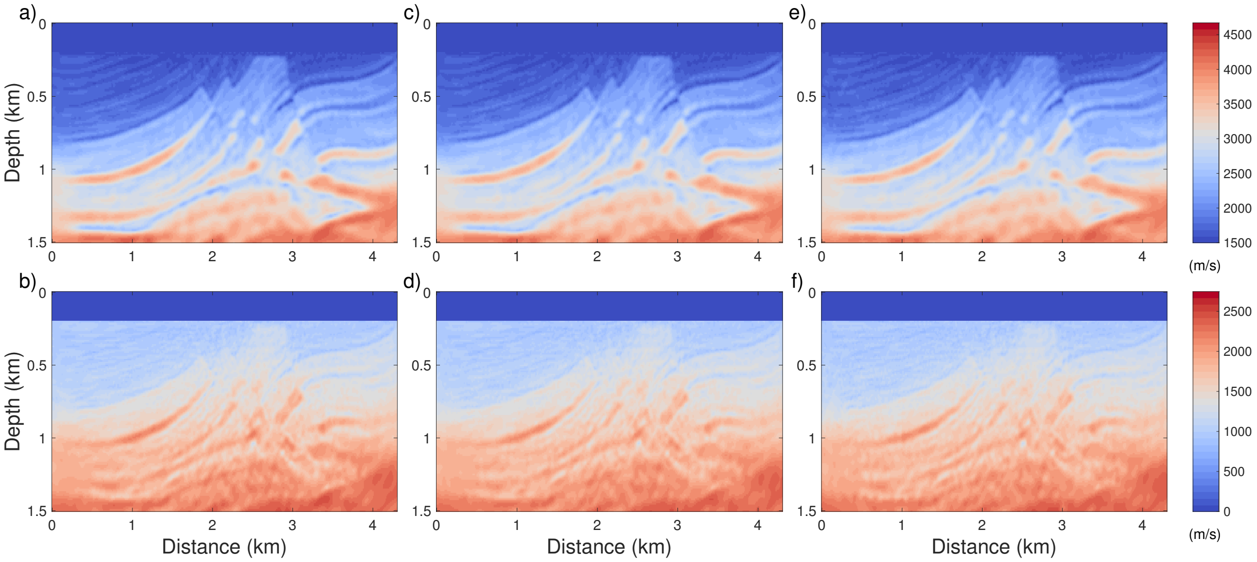

Figure 3.17: Inverted baseline model using noisy data: (a) and (b) are Vp and Vs using data with SNR=20, (c) and (d) are Vp and Vs using data with SNR=10, (e) and (f) are Vp and Vs using data with SNR=5.

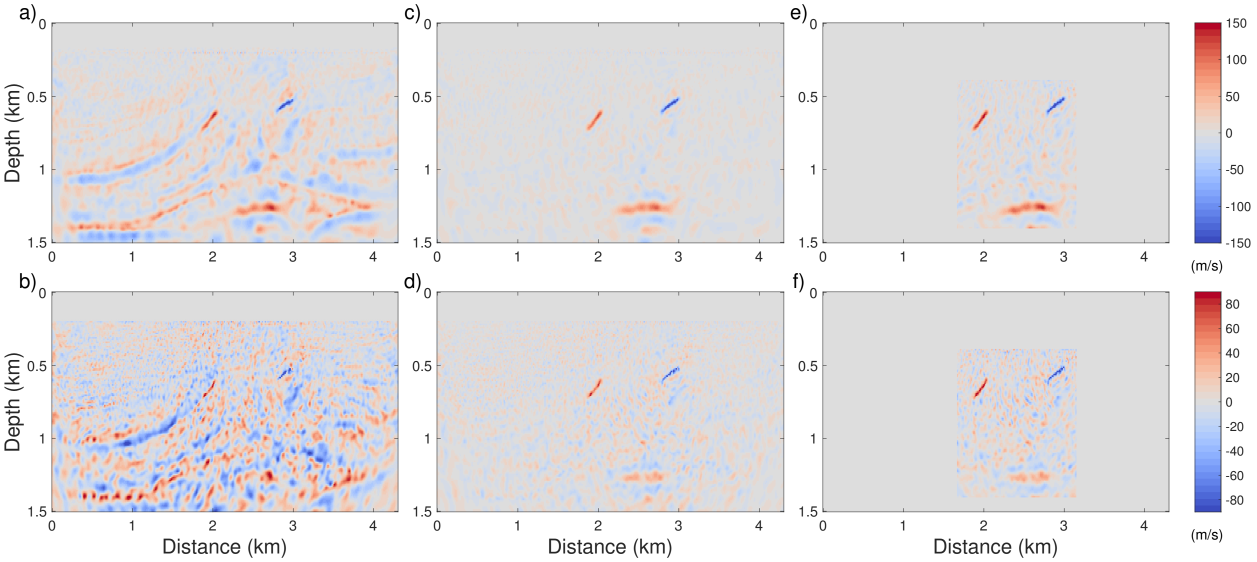

Figure 3.18: Tests with non-repeatable random noise. The time-lapse results of different strategies, in the case baseline and monitor data are noisy (SNR=20) with perfectly repeated acquisition geometry: (a) and (b) are Vp and Vs using the PRS, (c) and (d) are Vp and Vs using the CMS, (e) and (f) are Vp and Vs using the TO CMS. An increasing level of Gaussian random noise results in noisier time-lapse results, making it more difficult to detect deeper time-lapse changes. In all the following tests, including this one, the source-encoding method and parameters are identical across all FWI processes.

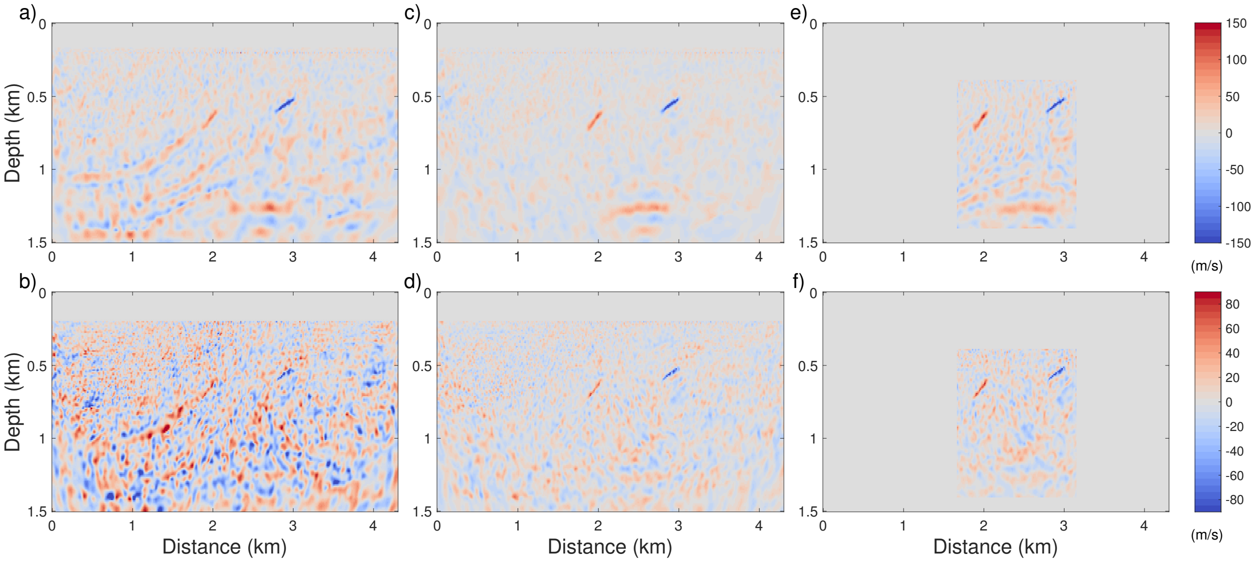

Figure 3.19: Tests with non-repeatable random noise. The time-lapse results of different strategies, in the case baseline and monitor data are noisy (SNR=10) with perfectly repeated acquisition geometry: (a) and (b) are Vp and Vs using the PRS, (c) and (d) are Vp and Vs using the CMS, (e) and (f) are Vp and Vs using the TO CMS. An increasing level of Gaussian random noise results in noisier time-lapse results, making it more difficult to detect deeper time-lapse changes.

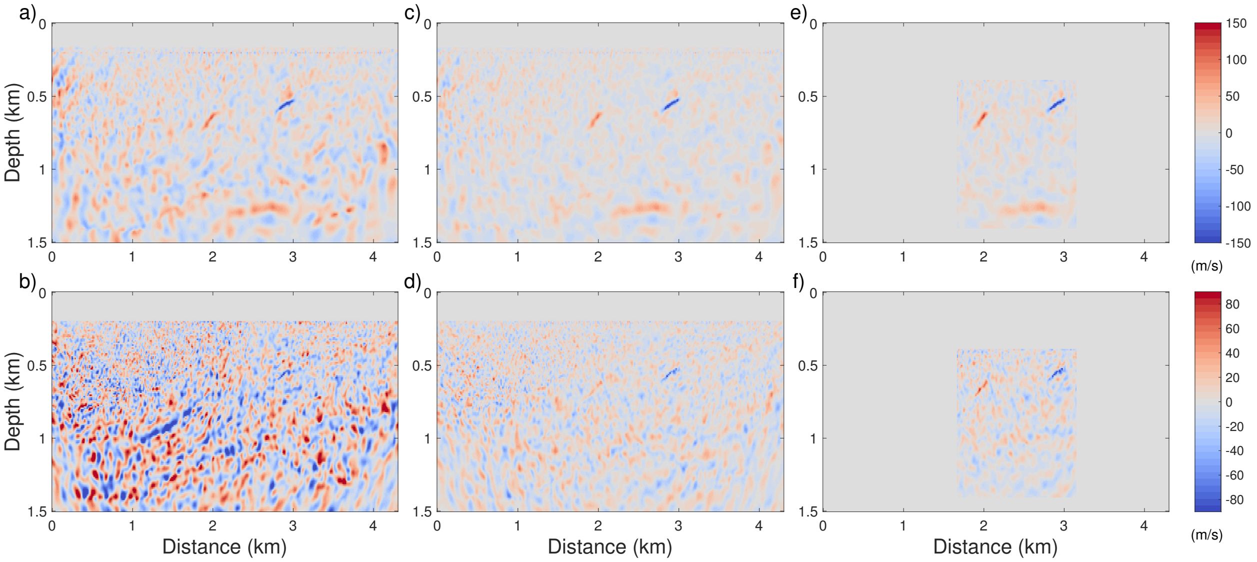

Figure 3.20: Tests with non-repeatable random noise. The time-lapse results of different strategies, in the case baseline and monitor data are noisy (SNR=5) with perfectly repeated acquisition geometry: (a) and (b) are Vp and Vs using the PRS, (c) and (d) are Vp and Vs using the CMS, (e) and (f) are Vp and Vs using the TO CMS. An increasing level of Gaussian random noise results in noisier time-lapse results, making it more difficult to detect deeper time-lapse changes.

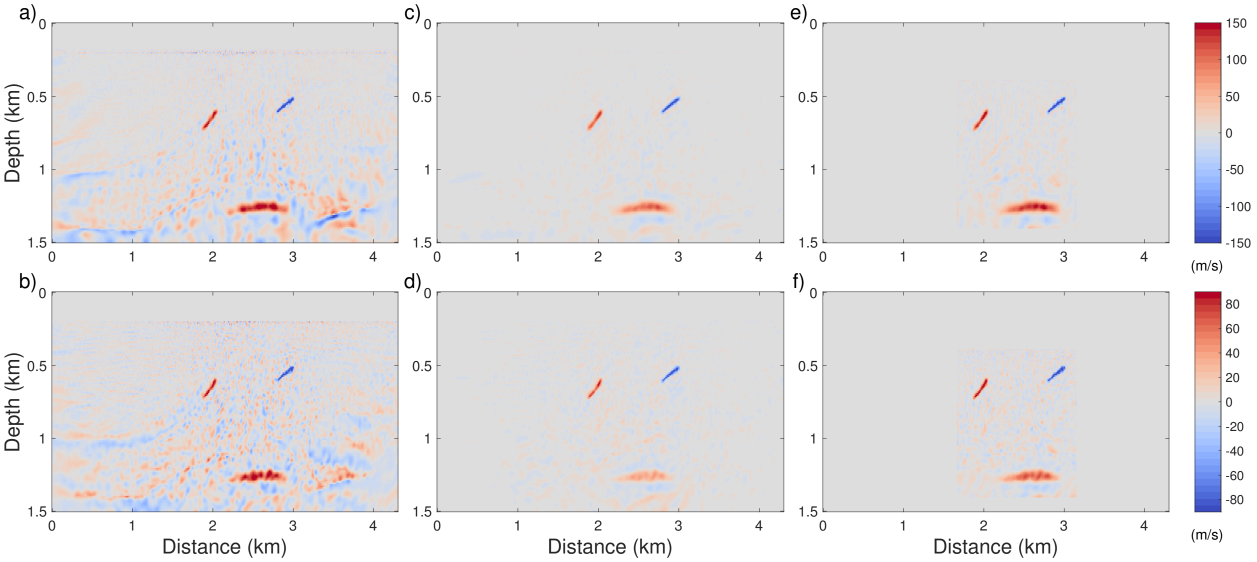

Figure 3.21: Tests with non-repeatable acquisition geometry. The time-lapse results of different strategies, in the case baseline and monitor data are noise-free, monitor source locations as a whole have been moved to the right of baseline source locations by 10 m: (a) and (b) are Vp and Vs using the PRS, (c) and (d) are Vp and Vs using the CMS, (e) and (f) are Vp and Vs using the TO CMS. The PRS is sensitive to the source position non-repeatability and gives the worst results and the TO CMS can recover more accurate values for the deeper velocity change.

changes are 20 m/s and 35 m/s, respectively, the water velocity changes decrease linearly from the surface to the seabed, and at the seabed, the minimum water velocity change is 5% of the maximum. In Figs. 3.24 and 3.25, the time-lapse inversion results for cases of non-repeatable seawater velocity change are plotted. In the case of a small seawater velocity change, we can observe that reservoir changes can still be identified from TO CMS and CMS, with the former showing better convergence and less coherent noise, but stronger random noise. In the case of a large seawater velocity change, the results are significantly impacted for both TO CMS and CMS.

In a realistic scenario, the velocity of seawater is subject to fluctuations due to various factors such as water temperature (T), salinity (S) and depth (D). The water temperature and the salinity vary at different time, the seawater velocity is described as Medwin (1975):

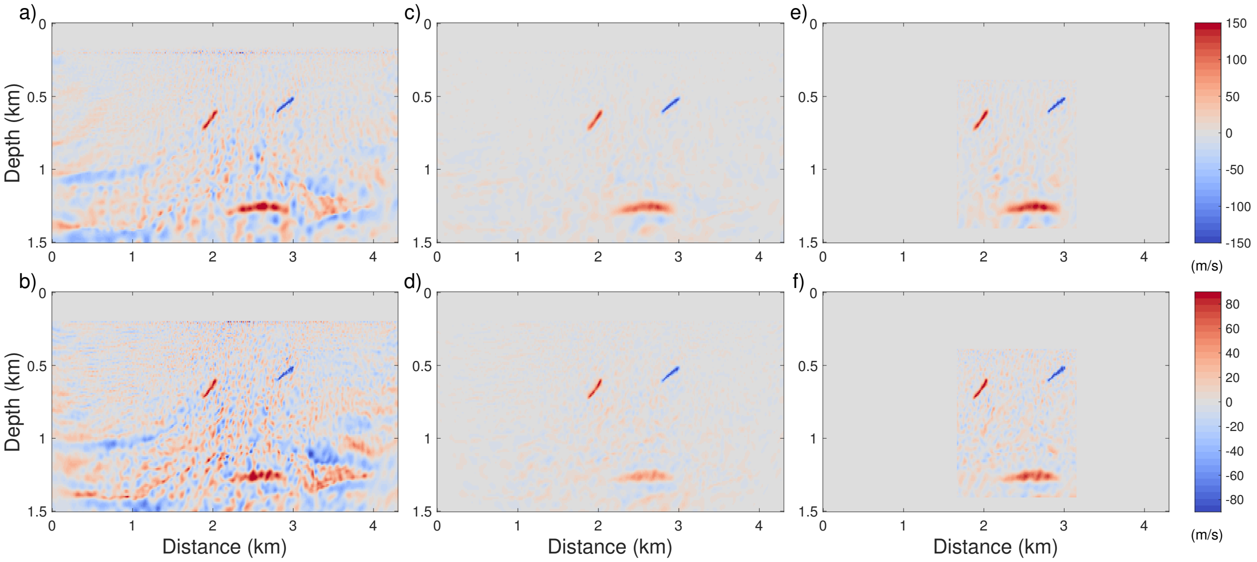

Figure 3.22: Tests with non-repeatable acquisition geometry. The time-lapse results of different strategies, in the case baseline and monitor data are noise-free, monitor source locations as a whole have been moved to the right of baseline source locations by 20 m: (a) and (b) are Vp and Vs using the PRS, (c) and (d) are Vp and Vs using the CMS, (e) and (f) are Vp and Vs using the TO CMS. The TO CMS can recover more accurate values for the deeper velocity change.

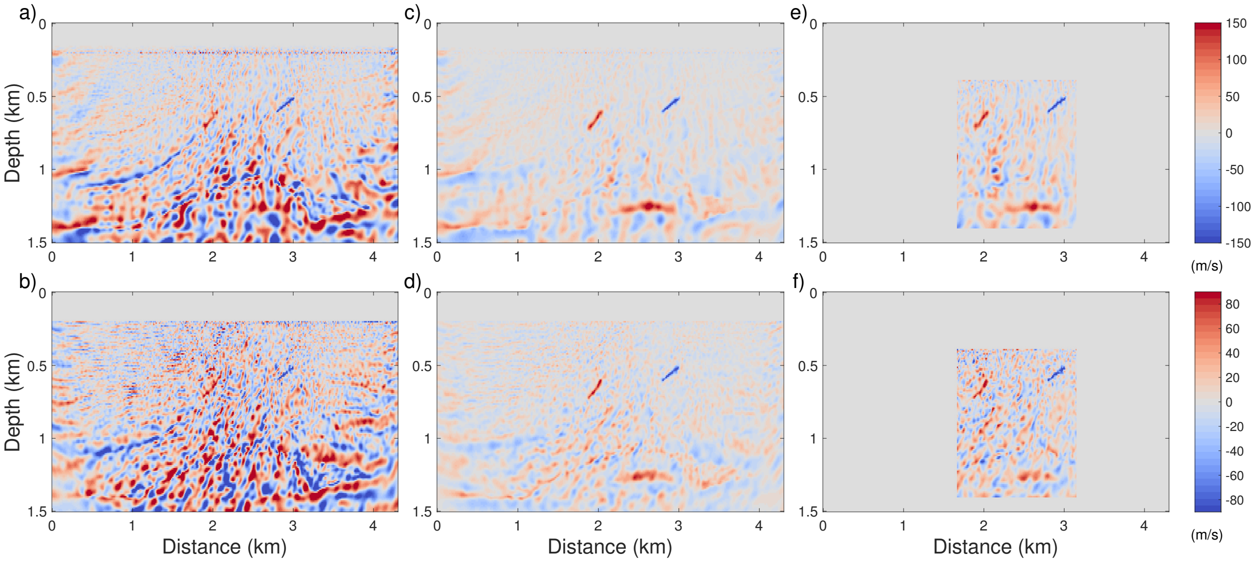

Figure 3.23: Tests with non-repeatable acquisition geometry. The time-lapse results of different strategies, in the case baseline and monitor data are noise-free. monitor source locations as a whole have been moved to the right of baseline source locations by 120 m: (a) and (b) are Vp and Vs using the PRS, (c) and (d) are Vp and Vs using the CMS, (e) and (f) are Vp and Vs using the TO CMS. The CMS and TO CMS provide similarly good results.

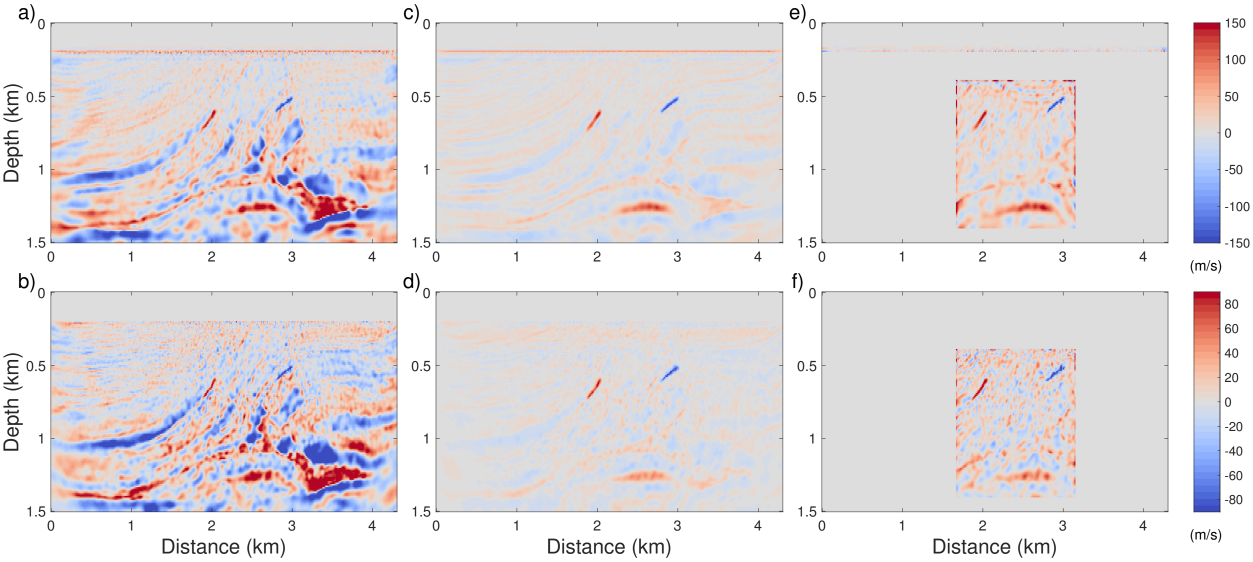

Figure 3.24: Tests with non-repeatable seawater velocity. The time-lapse results of different strategies, in the case baseline and monitor data are noise-free, the water velocity in monitor model is 20 m/s larger and kept constant in all FWI processes: (a) and (b) are Vp and Vs using the PRS, (c) and (d) are Vp and Vs using the CMS, (e) and (f) are Vp and Vs using the TO CMS. The CMS and TO CMS can still identify the velocity change areas.

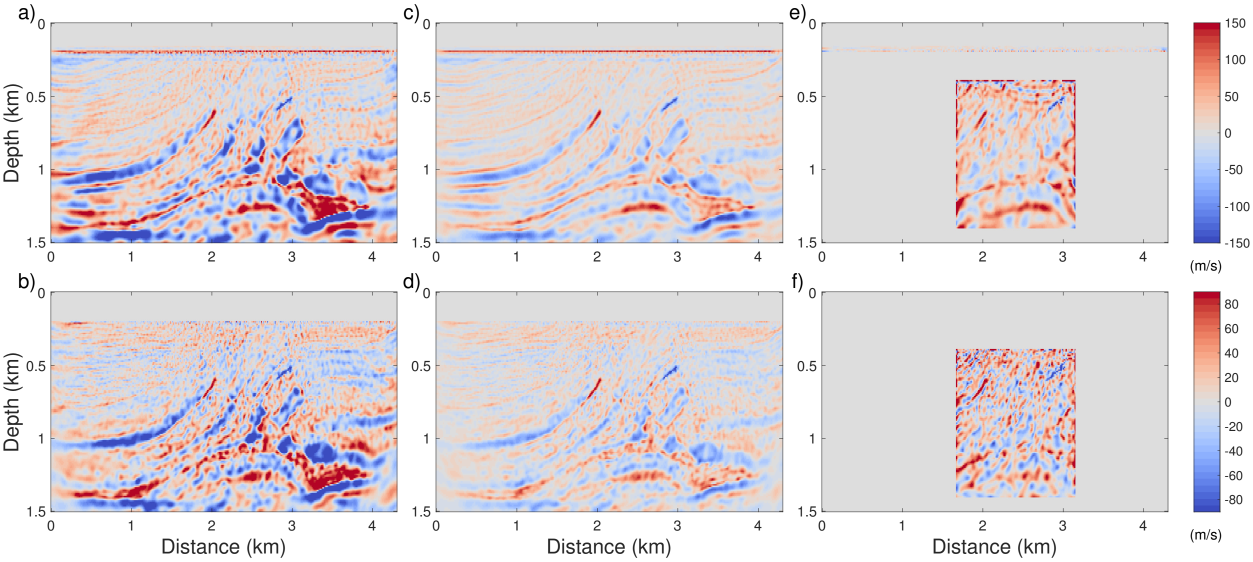

Figure 3.25: Tests with non-repeatable seawater velocity. The time-lapse results of different strategies, in the case baseline and monitor data are noise-free, the water velocity in monitor model is 35 m/s larger and kept constant in all FWI processes: (a) and (b) are Vp and Vs using the PRS, (c) and (d) are Vp and Vs using the CMS, (e) and (f) are Vp and Vs using the TO CMS. When the water velocity change is large, none of the time-lapse strategies succeed.

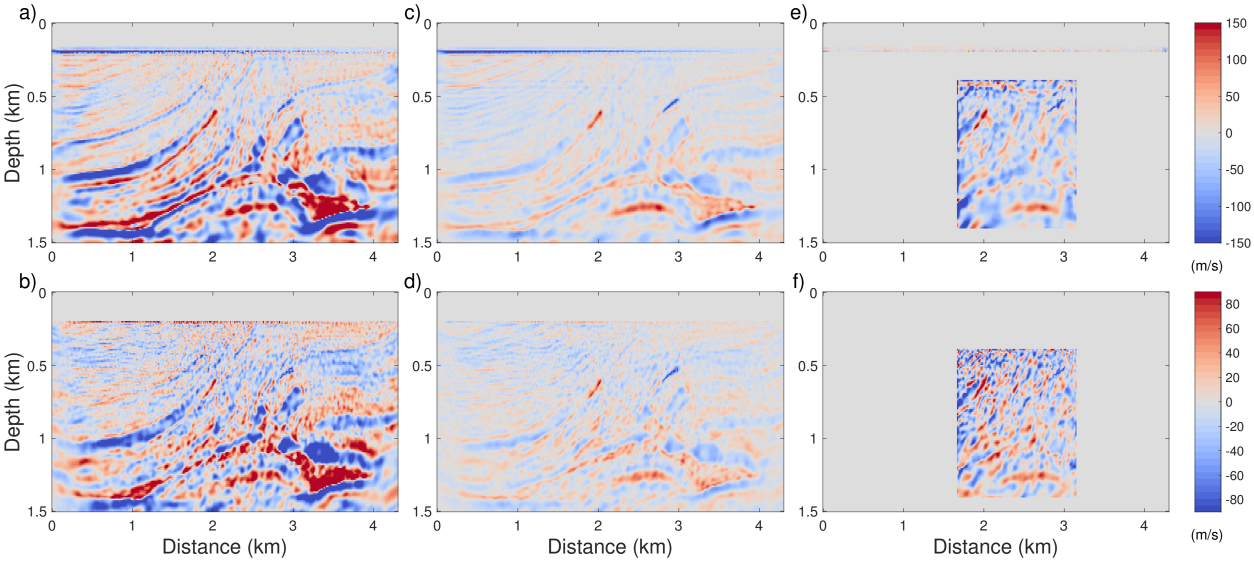

Figure 3.26: Tests with unknown and fluctuating spatially seawater velocity. The time-lapse results of different strategies, in the case where baseline and monitor data are noise-free, and the water velocity in the monitor model is spatially fluctuating and kept constant in all FWI processes: (a) and (b) are Vp and Vs using the PRS, (c) and (d) are Vp and Vs using the CMS, (e) and (f) are Vp and Vs using the TO CMS. The CMS and TO CMS can still identify the velocity change areas.

$$\begin{aligned} c = 1449.2 &+ 4.6T - 0.055T^2 + 0.00029T^3 \\ &+ (1.34 - 0.010T)(S - 35) \\ &+ 0.016D \end{aligned} \tag{3.13}$$

In the third case, we assume the water temperature (T) decreases linearly from the surface at 30 °C to the seabed at 0 °C, the salinity (S) increases linearly from left to right of the model from 35 to 0 ppt, the depth increases from the surface at 0 m to the seabed at 200 m. In this model, the maximum of seawater velocity difference is around 130 m/s. However, in most practical cases of FWI, the seawater velocity remains fixed as a constant. Hence, it is necessary to investigate how this affects the time-lapse FWI results, and the test results are plotted in Fig. 26. We observe that all the tested strategies exhibit strong artifacts. The TO CMS seems more sensitive to this situation. The non-repeatable seawater change issue in time-lapse FWI still requires further research Zhou and Lumley (2021b); Fu et al. (2024).

Overburden velocity change, no matter in a land time-lapse survey or a marine time-lapse survey, is still a trouble to identify the underground velocity changes and recover the velocity change values. It requires further investigation with more advanced time-lapse strategies. In land seismic surveys, surface-wave inversion may be incorporated into time-lapse inversion to exclude the surface velocity change effects.

Combined random noise and non-repeatable source locations

In this subsection, we test different strategies in the case that non-repeatable random noise and non-repeatable source locations exist at the same time. In this experiment, the SNRs of both baseline and monitor data are set to 20, and the source location in the monitor survey is 10 m (case 1) or 20 m (case 2) larger than that in the baseline survey. In Figs. 3.27 and 3.28, we plot the inversion results of different strategies. From the results, we observe that the PRS can not handle either cases 1 or 2, we can only recognize the reservoir change from the Vp result in case 2. For the CMS, the Vp and Vs changes can be imaged only in case 1, and the result for Vs in case 1 contains a lot of coherent artifacts. The best results are given by the TO CMS, we can clearly recognize the Vp and Vs changes from the results in both cases.

Crosstalk analysis

In this section, we analyze the crosstalk introduced by the coupling effects using our time-lapse EFWI strategy using two additional time-lapse models. The two time-lapse models are analogous to those employed in the previous sections utilizing the Marmousi model. However, they differ in that the first model exhibits only Vp time-lapse changes, while the second model exhibits only Vs time-lapse changes. In this way, the time-lapse changes can be used as Vp and Vs perturbations to analyze the crosstalk. The true and initial models remain the same. The general parameters for forward modeling and inversion are set to the same as in the section "Noise-free data tests". In Figs. 3.29 and 3.30, we respectively

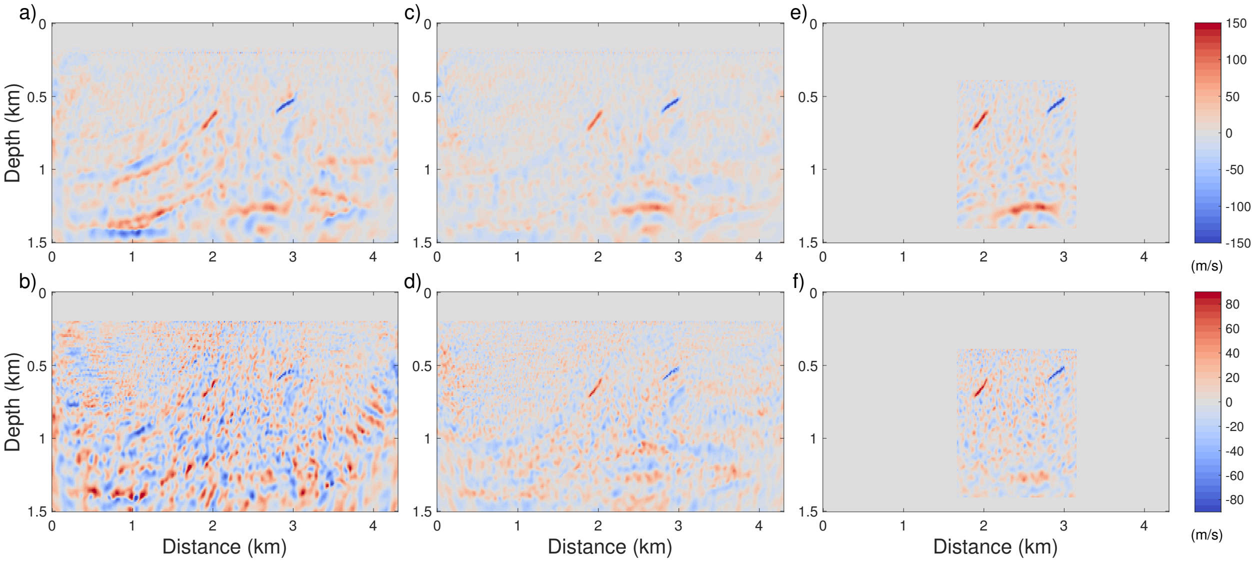

Figure 3.27: Tests with non-repeatable seawater velocity. The time-lapse results of different strategies, in the case baseline and monitor data are noisy (SNR=20), monitor source locations as a whole have been moved to the right of baseline source locations by 10 m: (a) and (b) are Vp and Vs using the PRS, (c) and (d) are Vp and Vs using the CMS, (e) and (f) are Vp and Vs using the TO CMS. The PRS fails, the CMS and TO CMS can detect the time-lapse changes.

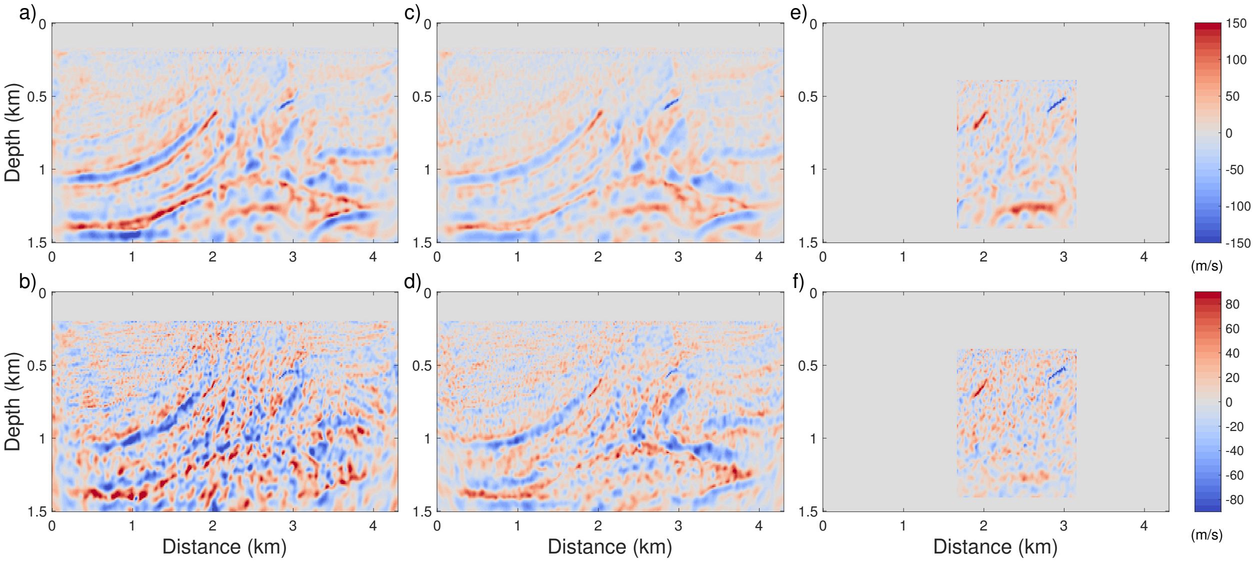

Figure 3.28: Tests with non-repeatable seawater velocity. The time-lapse results of different strategies, in the case baseline and monitor data are noisy (SNR=20), monitor source locations as a whole have been moved to the right of baseline source locations by 20 m: (a) and (b) are Vp and Vs using the PRS, (c) and (d) are Vp and Vs using the CMS, (e) and (f) are Vp and Vs using the TO CMS. The PRS and CMS fails, only the TO CMS can detect the time-lapse changes.

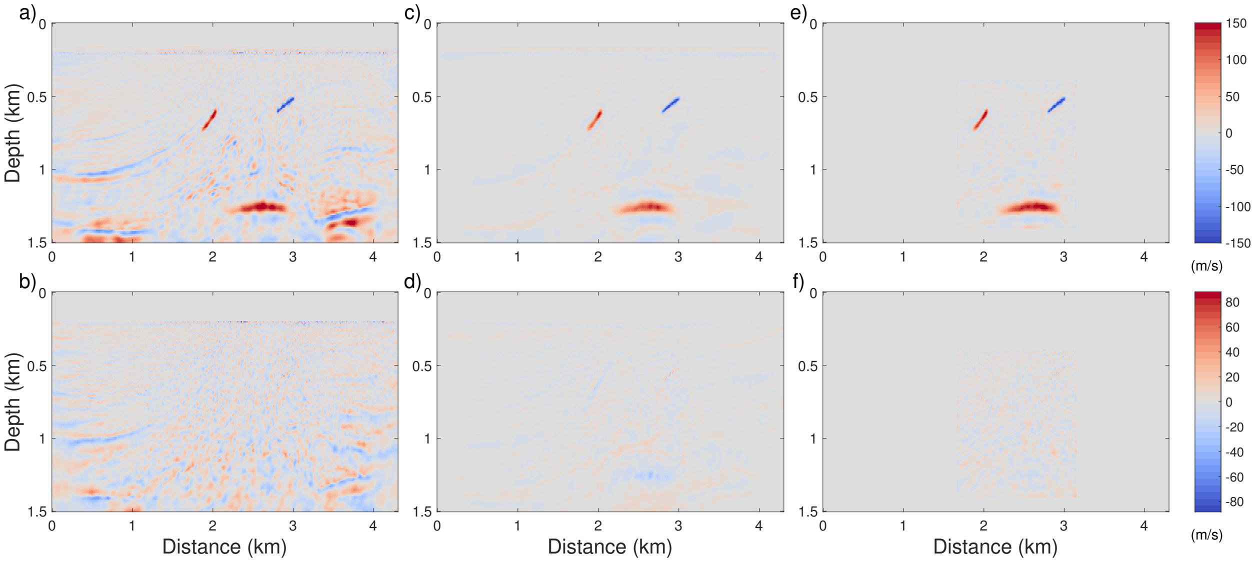

Figure 3.29: Tests with only Vp time-lapse changes in the Marmousi model: a) and b) are Vp and Vs using the PRS, c) and d) are Vp and Vs using the CMS, e) and f) are Vp and Vs using the TO CMS.

present the inverted time-lapse results for two time-lapse models using different time-lapse strategies. When only perturbations of Vp exist as shown in Fig. 3.29, in the results by the PRS, the artifacts are strong and we can't tell any time-lapse change of Vs, in the results by the CMS with mitigated artifacts, some subtle crosstalk can be revealed. In contrast, the TO CMS results effectively mitigate both artifacts and crosstalk. Similarly, in Fig. 3.30, when there are only perturbations of Vs, we observe similar outcomes.

Biased initial models

In the previous tests, the initial model in Fig 3.3 is unbiased, being a smoothed version of the true baseline model shown in Fig 3.2. In this section, we use two biased initial models to test the resilience of the different strategies to bias, using baseline and monitor datasets that are noise-free and are of identical acquisition geometries. The two biased Vp initial models are equal to the unbiased models minus and plus 100 m/s below the water layer. The biased Vs initial models are changed accordingly. In Figs. 3.31 and 3.32, the inverted time-lapse models using different strategies are plotted. In fist case, FWI can still relatively

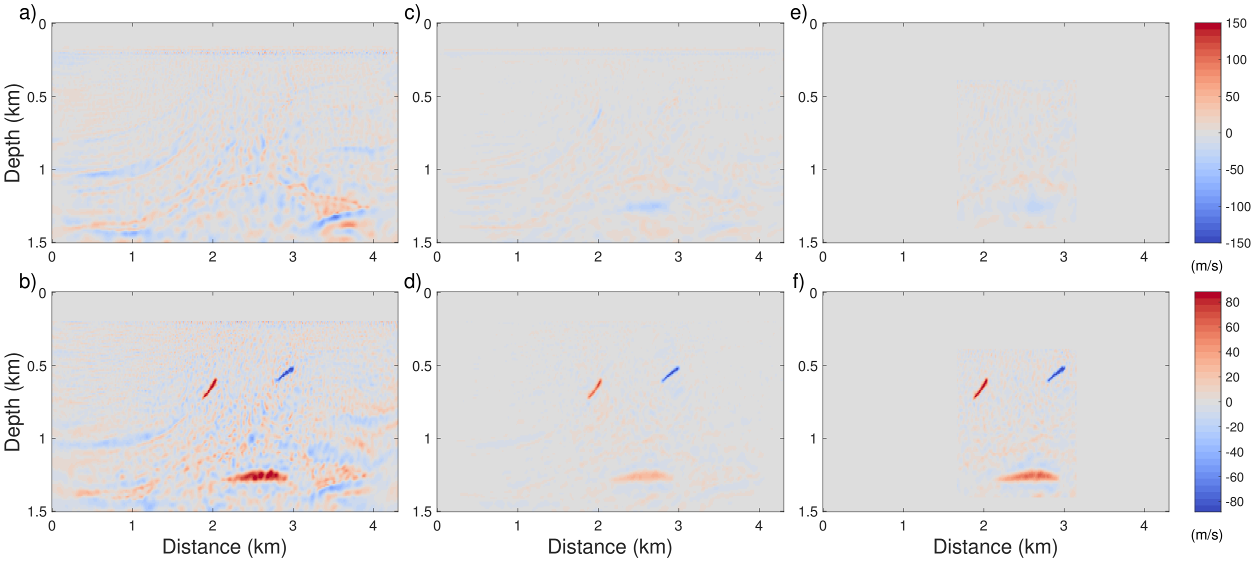

Figure 3.30: Tests with only Vs time-lapse changes in the Marmousi model: a) and b) are Vp and Vs using the PRS, c) and d) are Vp and Vs using the CMS, e) and f) are Vp and Vs using the TO CMS.

well recover the true models. In Fig 3.31, we can observe similar results as in Fig 3.11. In the second case, the increased velocities in the initial models results in degraded convergence, espetically in the inverted Vs modelw. In Fig 3.32, we observe that the PRS and CMS provide no meaningful results. However, in the results using the TO CMS, we can still identify the time-lapse changes.

3.3.3 Overthrust model

In this section, we also use a down-sampled Overthrust model to demonstrate the efficiency of the amplitude-encoding strategy in EFWI and feasibility of the CMS and the TO CMS in time-lapse EFWI. The true baseline Vp and Vs models are plotted in Fig. 3.33. We employ the smoothed true models as the initial models, which are plotted in Fig. 3.34. The time-lapse models are shown in Fig. 3.35, the Vp and Vs changes are set to 300 and 176 m/s. The dimension and grid size are the same as the Marmousi model. The general parameters for forward modeling and inversion are set to the same as in previous sections. In this section, we only consider two scenarios as in the Marmousi model tests.

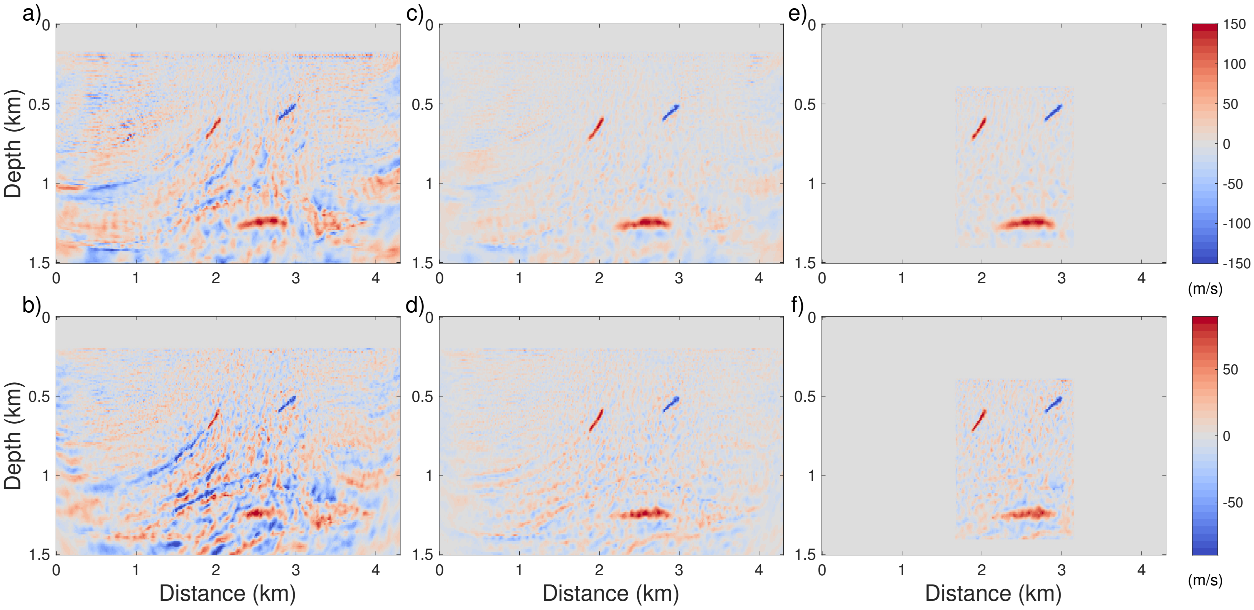

Figure 3.31: Tests with biased initial models. The time-lapse results of different strategies, in the case the biased Vp initial model is equal to the unbiased model (Fig. 3.3a) minus 100 m/s below the water layer. The biased Vs initial model is changed accordingly: a) and b) are Vp and Vs using the PRS, c) and d) are Vp and Vs using the CMS, e) and f) are Vp and Vs using the TO CMS.

Noise-free data tests

In the first case, we consider noise-free datasets with repeatable acquisition geometry. To further consider the influence of the target area on the time-lapse results of the TO CMS, in Fig. 3.36, we present the inverted time-lapse results of the PRS, CMS and TO CMS with varying target areas. As with the Marmousi model examples, the comparison of results by different time-lapse strategies leads to the same conclusion. The results of the TO CMS with different scales of target area demonstrate that more precise prior information leads to more accurate time-lapse change recovery. In Fig. 3.37, we plot the extracted traces at the distance of 1.9 km in the inverted time-lapse results using the PRS, the CMS, and the TO CMS with the smallest target updating area, respectively.

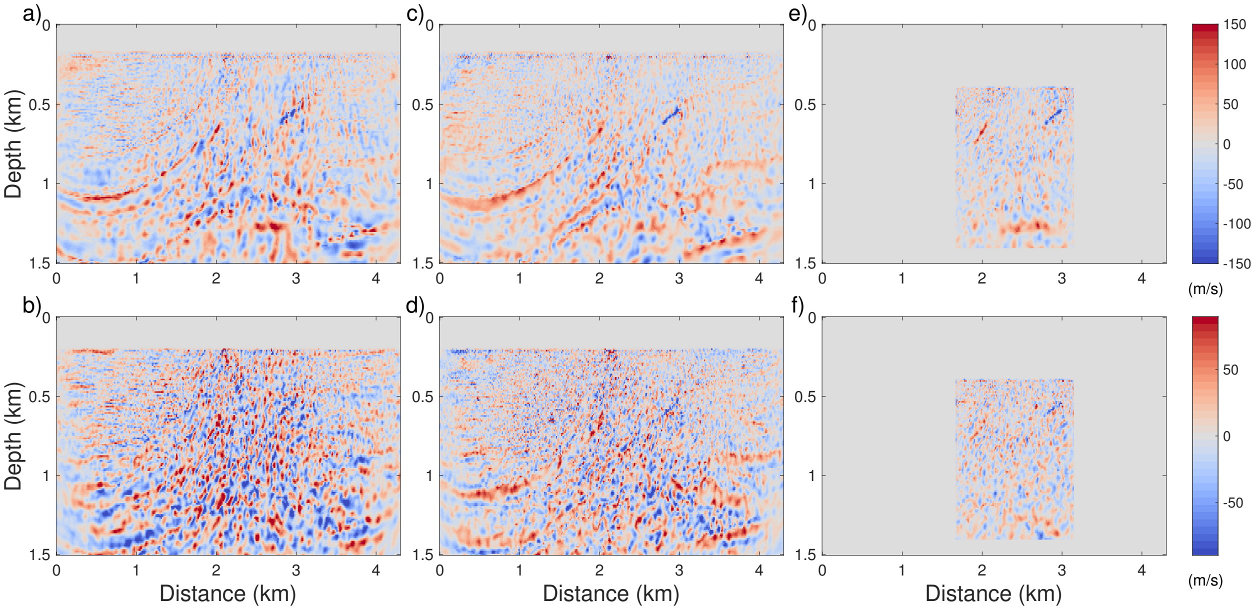

Figure 3.32: Tests with biased initial models. The time-lapse results of different strategies, in the case the biased Vp initial model is equal to the unbiased model (Fig. 3.3a) plus 100 m/s below the water layer. The biased Vs initial model is changed accordingly: a) and b) are Vp and Vs using the PRS, c) and d) are Vp and Vs using the CMS, e) and f) are Vp and Vs using the TO CMS.

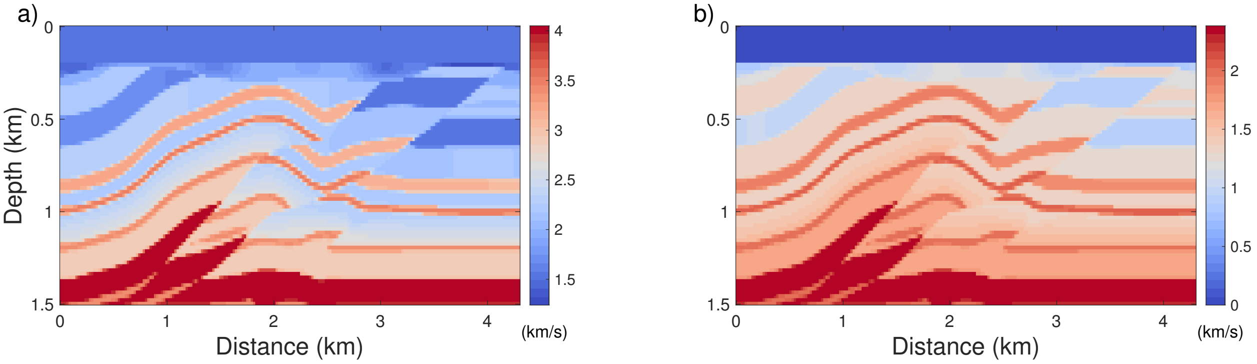

Figure 3.33: True baseline model: (a) Vp model and (b) Vs model.

Combined random noise and non-repeatable source locations

In the second test, we consider the second case in the 'Combined random noise' section, where the SNRs of both baseline and monitor data are set to 20, and the source location in the monitor survey is or 20 m larger than that in the baseline survey. In Figs. 3.38 and **??**, we present the inverted time-lapse results and extracted traces at distance 1.9 km using different strategies. From the results using two different models, we have illustrated the

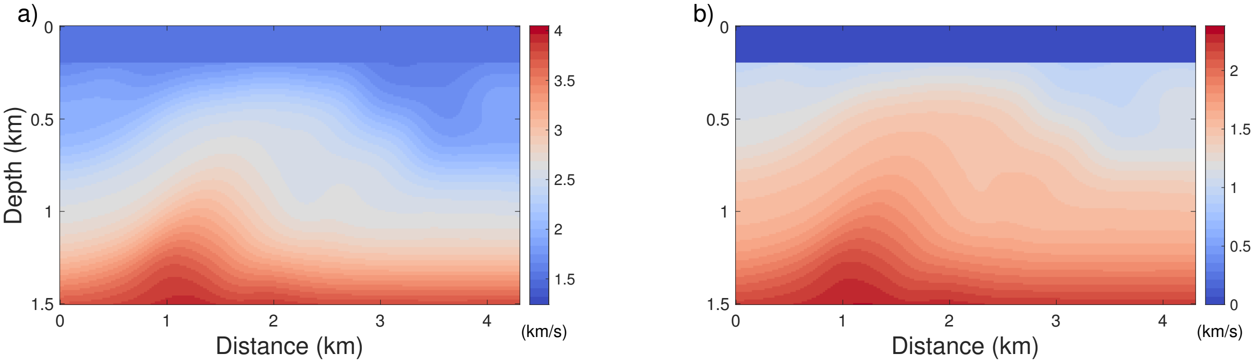

Figure 3.34: The initial baseline model: (a) Vp model and (b) Vs model.

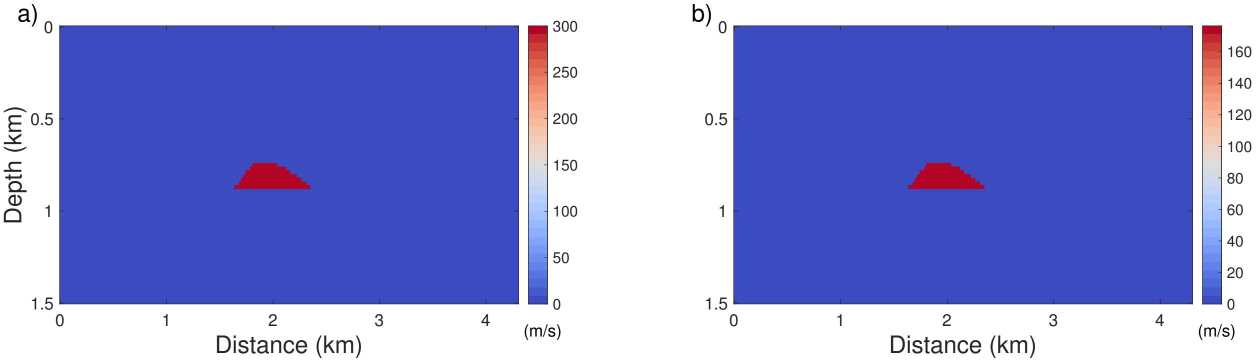

Figure 3.35: True time-lapse model: (a) Vp model and (b) Vs model.

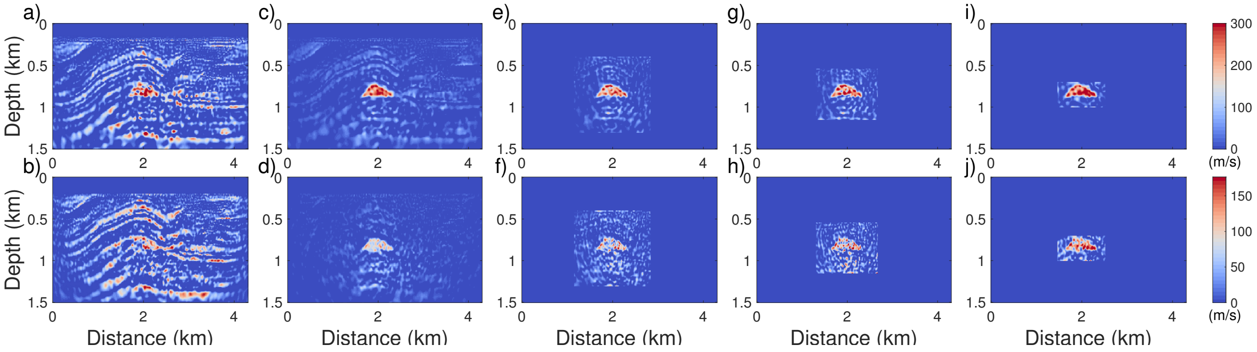

Figure 3.36: Tests with varying target areas in the Overthrust model. The time-lapse results of different strategies, in the case baseline and monitor data are noise-free: a) and b) are Vp and Vs using the PRS, c) and d) are Vp and Vs using the CMS, e), g) and i) are Vp using the TO CMS with decreasing updating target area, f), h) and j) are Vs using the TO CMS with decreasing updating target area.

feasibility of the CMS and the TO CMS in multi-source time-lapse elastic FWI.

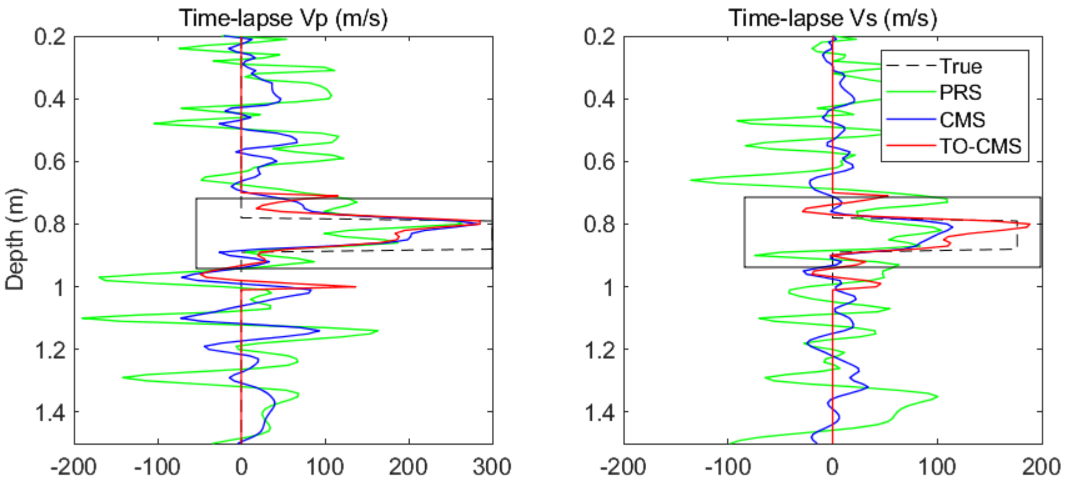

Figure 3.37: Extracted traces of inverted time-lapse results of different strategies, in the case baseline and monitor inversions use the noise-free data with perfectly repeated acquisition geometry: (a) and (b) are time-lapse Vp and Vs.

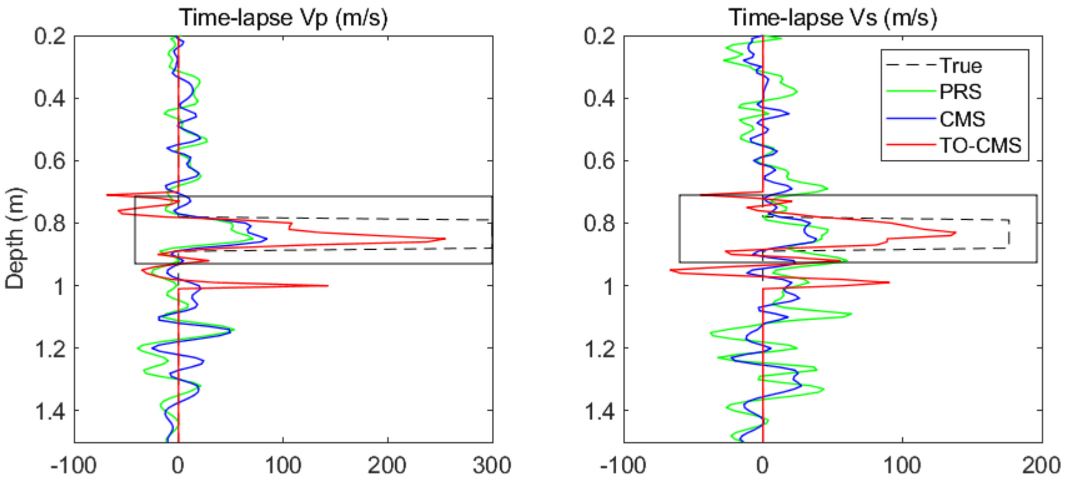

Figure 3.38: Tests with varying target areas in the Overthrust model. The time-lapse results of different strategies, in the case baseline and monitor data are noisy (SNR=20) and monitor source locations as a whole have been moved to the right of baseline source locations by 20 m: a) and b) are Vp and Vs using the PRS, c) and d) are Vp and Vs using the CMS, e), g) and i) are Vp using the TO CMS with decreasing updating target area, f), h) and j) are Vs using the TO CMS with decreasing updating target area.

3.4 Discussions

The difference between acoustic and elastic FWI is that elastic FWI concerns more than one parameter to be inverted, and there is inevitable crosstalk between Vp and Vs Matharu and Sacchi (2018). Compared with acoustic FWI, elastic FWI demands much more computational effort. Hence, the investigation of application of multi-source strategies in elastic FWI is important, especially in a time-lapse survey, which requires carrying out more times of elastic FWI. The issue of source-encoding strategy applied to FWI is the crosstalk introduced by the individual shot gathers, which can be represented by the off-diagonal elements in the crosstalk matrix shown in Fig. 3.5(b). The crosstalk resulting from multi-parameter inversion and source-encoding strategy makes the multi-source elastic FWI more challenging. When this come to the time-lapse elastic FWI, where a small area of time-lapse change exist in the monitor survey, it requires much higher resolution and accuracy for us to identify the time-lapse change location and recover the time-lapse change value.

Using a multi-source strategy will eventually introduce crosstalk noise in a baseline model inversion or a monitor model inversion, and this crosstalk noise will eventually exist in the time-lapse result. If the crosstalk noise is large enough, we can't obtain an acceptable inversion result even for a baseline model, not to mention the time-lapse result. While using a multi-source strategy is still a good choice to accelerate FWI, the key is that we need to balance the calculation efficiency and the imaging quality, that's why we compose the individual shot gathers into several super-shots instead of just one super-shot, because using too few super-shots will introduce non-ignorable crosstalk noise into the inversion result. The speed-up ratio for the amplitude-encoding EFWI is roughly the total number of individual shots divided by the number of super-shots. The numerical experiment illustrates that the output Vp and Vs of adopting this strategy are comparable to those of using the conventional EFWI. Then the amplitude-encoding EFWI is employed for the time-lapse inversion to save computational time. To stably invert the reservoir changes, the same amplitude-encoding parameters should be set up for baseline and monitor EFWI both, otherwise, it could generate artifacts due to the non-repeated amplitude-encoding parameters. In our results, we tried to show that balance and feasibility when the time-lapse result can be well recovered with improved calculation efficiency.

In this study, we use one target area to include three reservoir changes while conducting the TO CMS. On one hand, we are trying to include enough background area, since the contrast between the time-lapse change and the background is important to detect the reservoir change area in practice. On the other hand, precisely locating the reservoir change area is difficult in practice, using a big target area is easy to operate. Of course, for some cases with good prior location information on the reservoir change area, a tight target area can be used. For instance, three independent target areas can be utilized in the modified Marmousi model in this study. It may help to enhance the inverted results further. Actually, in the test of the time-lapse Overthrust model in this study, a tighter target area is employed, which also gives satisfactory results.

In the study, the SNR for time-lapse data with non-repeatable random noise is relatively high, and the value should be much lower in real cases, which could damage signals corresponding to reservoir changes. A more anti-noise EFWI algorithm, such as adding certain penalty terms to the EFWI, could be better. As for how to handle non-repeatable correlated noise, we believe it is still an open question. Moreover, using ambient noise to perform passive time-lapse imaging of the subsurface is also proven in some seismic monitoring cases (Mordret et al., 2014; De Ridder et al., 2014).

The non-repeatability scenarios tested in this study are not too serious compared with real field data cases. For strong non-repeatable noise, large source/receiver position non-repeatability, and complex sea-surface conditions all the time-lapse methods mentioned in this study could fail. Moreover, all tests in this study are based on a good initial model, and the impact of a bad initial model is not discussed, which could be serious. Hence, developing more powerful time-lapse imaging methods is still significant.

3.5 Conclusions

In this study, we have implemented the amplitude-encoding strategy for EFWI, which can significantly improve computational efficiency. In time-lapse EFWI, the same amplitude-encoding parameters should be set up for baseline and monitor model inversions, which would avoid the artifacts resulting from the non-repeated amplitude-encoding parameters.

Furthermore, we've applied CMS to time-lapse EFWI and assessed its robustness and effectiveness through numerical examples in different scenarios. Compared with the conventional PRS, the CMS can effectively reduce the artifacts arising from the convergence difference between the baseline and monitor inversions. Moreover, we have designed a TO CMS by incorporating the prior location information of the reservoir changes into the CMS, and the numerical tests demonstrate that the TO CMS can enhance the model convergence and improve the accuracy of the inverted time-lapse changes. In the application of the TO CMS, a more precise target area results in better time-lapse change resolution. Experiments have also shown that strong noise and changes in seawater velocity have a serious impact on time-lapse EFWI results, these issues require further research.

Chapter 4

Time-lapse FWI using field accelerometer data at CaMI

Applying full-waveform inversion (FWI) to walkway vertical seismic profile (VSP) data provides a promising method for obtaining high-resolution models of subsurface physical properties. While time-lapse FWI has shown potential for monitoring reservoir changes caused by CO_2 storage with high resolution, its application in field data remains scarce due to its vulnerability to non-repeatable noise. We conduct a field experiment using time-lapse VSP data and FWI to monitor long-term changes in a thin, shallow reservoir due to CO_2 injection. We present a workflow that uses time-lapse FWI for field walkway VSP data to identify time-lapse changes related to less than 60 tons of CO_2 injected into a 7 m-thick reservoir at a depth of 300 m. A frequency range of 5 to 60 Hz is applied to achieve high-resolution results. This experiment showcases the capability of FWI to perform high-resolution inversion and detect time-lapse anomalies within a shallow reservoir caused by a small amount of CO_2 injection. To the best of our knowledge, no similar field experiments have been reported.

4.1 Introduction

Time-lapse seismic inversion is a powerful tool for monitoring reservoir changes introduced by CO_2 injection and sequestration. Vertical seismic profile (VSP) surveys offer higher vertical resolution and an improved signal-to-noise ratio compared with surface seismic methods. When combined with full-waveform inversion (FWI), a high-resolution seismic imaging technique capable of capturing subtle reservoir changes over time (Virieux and Operto, 2009), VSP data further improves the detection of time-lapse anomalies. This makes the application of FWI to VSP data particularly well-suited for reservoir monitoring. Liang et al. (2013) detected the time-lapse changes in a heavy oil field introduced by steam injection. Yang et al. (2014) reported challenges in detecting time-lapse differences related to CO_2 injection, partly due to limitations in acquisition geometry. A notable result was obtained by Egorov et al. (2017), who applied FWI to single-source VSP data and identified changes in a saline aquifer at 1500 m depth, caused by the injection of 15,000 tons of CO_2. Cai et al. (2024) used FWI to monitor short-term CO_2 injection at 300 m depth with rapidly repeated single-source VSP data. Other studies have explored using FWI with various borehole data to monitor water injection at shallow depths. Nakata et al. (2022) monitored the dynamic transient fluid-flow effects introduced by water injection at a depth around 25 m, using controlled-source crosswell data. Liu et al. (2023) monitored velocity changes at an approximate depth of 11.6 m associated with in-situ fracture evolution at a shallow contamination site, using continuous active-source borehole data. These studies underscore the potential of this technique for high-resolution subsurface imaging. However, due to its sensitivity to non-repeatable noise, the application of FWI to time-lapse VSP data remains relatively rare, particularly for CO_2 monitoring.

Unlike the cases mentioned above, which involve shallow water injection, large-scale deep CO_2 injections, single-source time-lapse surveys, or short-term monitoring, this study conducts a field experiment using time-lapse walkaway VSP data and FWI to track long-term changes in a thin (7 meters), shallow (at approximately 300 m depth) reservoir caused by less than 60 tons of CO_2 injection.

4.2 Geologic background at the CaMI.FRS

The Field Research Station (FRS), located approximately 200 km southeast of Calgary and developed by the Containment and Monitoring Institute (CaMI) under Canada Management Canada (CMC) Research Institutes Inc., was established to drive research in secure CO_2 storage technologies (Macquet et al., 2019). The injection target is the Basal Belly River Sandstone (BBRS) formation, situated at a depth of 295–302 m. Overlying the BBRS is the 152 m-thick Foremost Formation, consisting of clayey sandstone interbedded with coal layers. The VSP datasets were acquired in 2018 and 2022, serving as the baseline and monitor data (Hall et al., 2019a; Innanen et al., 2022). The injection well is located 20 m northeast of the observation well, where accelerometers were deployed at intervals of 1 to 2 meters, extending from the surface to a depth of approximately 324 m. A Vp well log was recorded from the injection well between depths of 61 and 337 m, as shown on the right side in Fig 4.1. The distributions of geology formations and rock types at different depths in the subsurface of CaMI.FRS also are plotted in Fig 4.1.

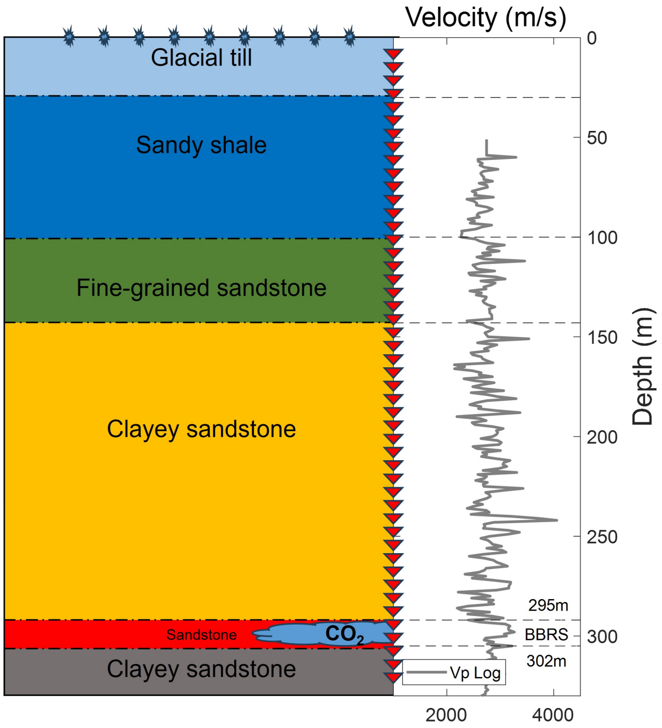

Figure 4.1: On the left is the geology formation at different depths, different colors denote different rock types. On the right side is the Vp velocity well log measured from the injection well (gray line). The horizontal dashed lines indicate dashed gray lines indicate the boundaries of geological formations. The blue stars on top of the surface denote the sources deployed from the southwest to the observation well, in which the red rectangles denote the receivers are deployed. The blue cloud denotes the CO_2 injected into the BBRS layer.

The Vp (P-wave velocity) well log is available from the observation well from 61 to 336 m The distributions of geology formations and rock types at different depths in the subsurface of CaMI.FRS also are plotted in Fig 4.1. In 2018 and 2022, two 3D VSP DAS datasets were acquired by CREWES. One baseline survey before the injection and one monitor after the injection. In both 3D datasets (referred to as Snowflake data I and II), a total of 12 shot lines are deployed at 15-degree intervals centered around the observation well. The INOVA Univib system was employed during the 2018 survey, whereas the 2022 survey utilized the

INOVA AHV-IV vibrator. Although both vibrators exhibit comparable source signatures, the preferred sweep parameters differ slightly between the two surveys (Innanen et al., 2022). The acquisition is presented by Ji et al. (2024). The observation well is located in the center of the snowflake, and the injection well is located 20 m away from the observation well to the northeast aligned in line 4. In the observation well, straight DAS fibers and accelerometers are deployed at 1 to 2 m intervals from the surface to around 324 m in depth.

4.3 Full-waveform inversion

In time-domain acoustic FWI, we adopt the global-correlation norm (GCN) as the objective function (Choi and Alkhalifah, 2012). The GCN measures the coherence between the predicted data and the observed data by

$$E(\mathbf{m}) = \sum_{s=1}^{n_s} \sum_{r=1}^{n_g} [-\hat{\mathbf{u}}(s, r, \mathbf{m}) \cdot \hat{\mathbf{d}}(s, r)] \tag{4.1}$$

where $\mathbf{m}$ represents the subsurface model parameters, $\mathbf{s}$ and $\mathbf{r}$ denote the source and receiver location vectors (Liu et al., 2023). The GCN, similar to phase-only inversion in the frequency domain (Choi and Alkhalifah, 2012), is expected to make the inversion of onshore VSP data more stable than methods based on the standard objective function. The normalized predicted and observed data are expressed as:

$$\hat{\mathbf{u}}(\mathbf{s}, \mathbf{r}, \mathbf{m}) = \frac{\mathbf{u}(\mathbf{s}, \mathbf{r}, \mathbf{m})}{\|\mathbf{u}(\mathbf{s}, \mathbf{r}, \mathbf{m})\|_2} \tag{4.2}$$

and

$$\hat{\mathbf{d}}(\mathbf{s}, \mathbf{r}) = \frac{\mathbf{d}(\mathbf{s}, \mathbf{r})}{\|\mathbf{d}(\mathbf{s}, \mathbf{r})\|_2}, \tag{4.3}$$

where $\mathbf{u}(\mathbf{s}, \mathbf{r}, \mathbf{m})$ and $\mathbf{d}(\mathbf{s}, \mathbf{r})$ are the predicted and observed data, respectively. The gradient of the objective function with respect to the model parameters is derived as (Choi and Alkhalifah, 2012):

$$\frac{\partial E(\mathbf{m})}{\partial m_i} = \sum_{s=1}^{n_s} \sum_{r=1}^{n_g} \left[\frac{\partial \mathbf{u}(s, r, \mathbf{m})}{\partial m_i} \cdot \mathbf{b}(s, r, \mathbf{m}) \right], \tag{4.4}$$

where $m_i \in \mathbf{m}$, and $\mathbf{b}(\mathbf{s}, \mathbf{r}, \mathbf{m})$ is the back-propagated residual, defined as :

$$\mathbf{b}(\mathbf{s}, \mathbf{r}, \mathbf{m}) = \frac{\{\hat{\mathbf{u}}(\mathbf{s}, \mathbf{r}, \mathbf{m})[\hat{\mathbf{u}}(\mathbf{s}, \mathbf{r}, \mathbf{m}) \cdot \hat{\mathbf{d}}(\mathbf{s}, \mathbf{r})] - \hat{\mathbf{d}}(\mathbf{s}, \mathbf{r})\}}{\|\mathbf{u}(\mathbf{s}, \mathbf{r}, \mathbf{m})\|_2}. \tag{4.5}$$

4.4 Results

In the walkway VSP acquisition, the offsets range from 10 m to 480 m. The surveys include 47 sources deployed from east to west, with a nearly uniform spatial interval of 10 m. To focus on the direct waves and the reflected waves from the target layer, we apply a time window of 300 ms and a bandpass filter within 5 to 60 Hz. We convert accelerometer data to displacement by negating the sign to maintain consistency in polarity with displacement. The grid cell size is set to 2 m and the receiver spatial interval is resampled accordingly accounting for the thickness of the reservoir. In Figure 4.2, we present three VSP gathers from the baseline data, the monitor data and their differences.

We conduct FWI of Vp using the vertical component of the field data. The inversion workflow is implemented in an open-source software package IFOS2D (Bohlen et al., 2016a). Following several trial experiments, the filtered Ricker wavelet was identified as a suitable wavelet for the inversion. The inverted baseline and monitor models are presented in Figure 4.3c and d, illustrating effective model updates within a 300 m offset, with the observation well located at 0 m. Compared with the initial model derived by Gaussian smoothing the well log data shown in Figure 4.3a, we observe that FWI significantly improves the model's resolution by introducing fine details into the initial model. The inversion results resolve the target layer at approximately 300 m depth. Furthermore, a 3 m-thick coal layer at approximately 160 m depth is visible in the inverted model, emphasizing FWI's ability to capture thin and subtle subsurface features. In Figure 4.3b, we compare the smoothed well

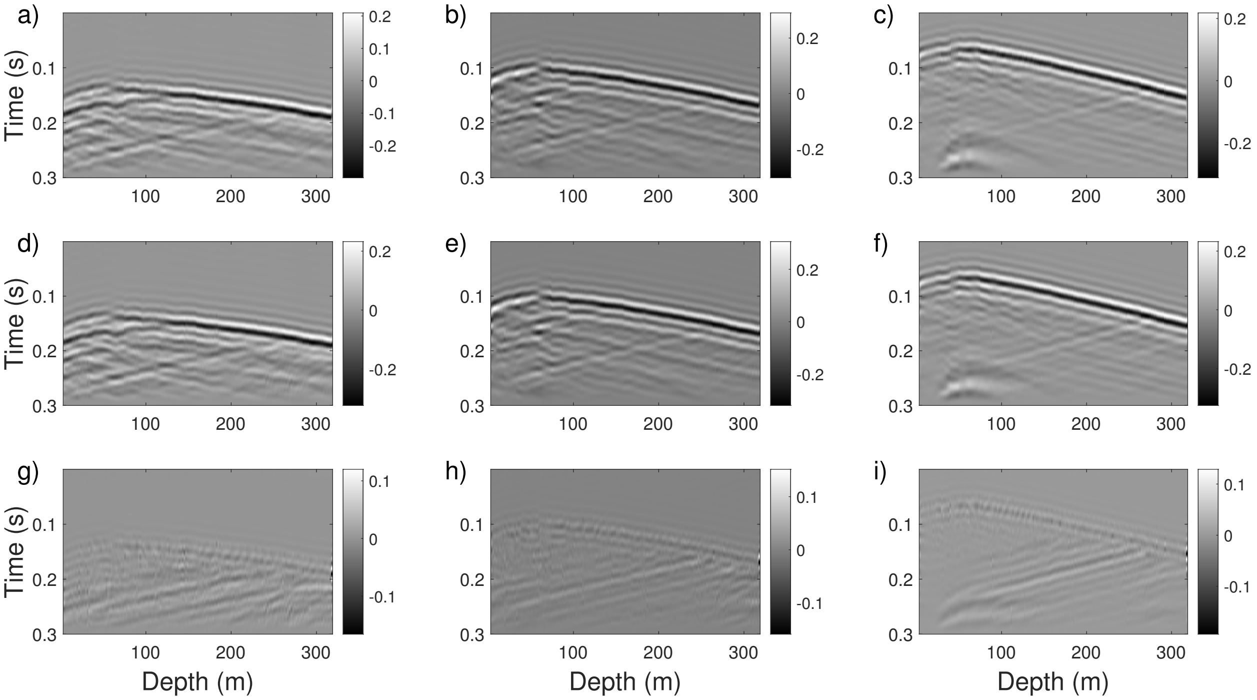

Figure 4.2: Three VSP gathers from the field baseline data (first row), the field monitor data (second row) and their differences (third row). The offsets of the three gathers from left to right are 290, 190, and 90 m, respectively. The differences between the strong upgoing reflected waves in these gathers highlight the seismic response changes introduced by CO_2 injection.

log, initial model, and inverted baseline and monitor models at an offset of 0 m. Both inverted models align well, with only minor discrepancies. For quality control, in Figure 4.4, we present the comparisons of the field baseline data, the simulated data before and after FWI at different offsets.

Following the workflows of the parallel strategy (Lumley et al., 2003) and common-model strategy (Hicks et al., 2016), we obtain the time-lapse change as shown in Figure 4.5a and b. The results demonstrate that the time-lapse change is captured within the 7 m-thick reservoir, and due to the illumination limitations of VSP acquisition geometry, the far edge of the reservoir cannot be accurately identified using VSP data. Comparing two time-lapse results, we observe that the CMS reduces 4D noise while maintaining the localized time-lapse change.

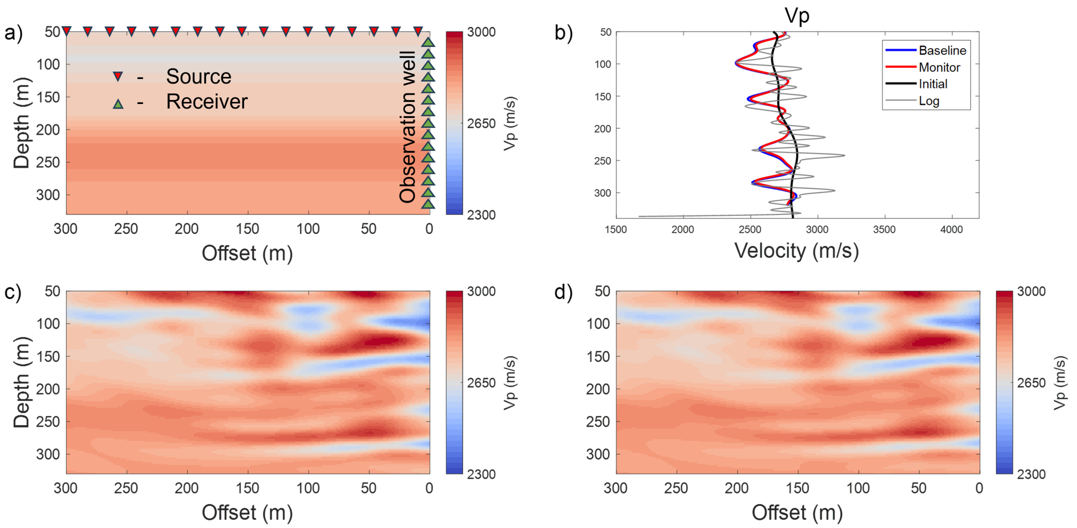

Figure 4.3: (a) The initial model constructed by Gaussian smoothing the well log. The red and green triangles denote the sources and receivers. (b) Comparison of the smoothed well log (gray line), initial model (bold black line), and inverted baseline and monitor models (blue and red lines) using field data at an offset of 0 m. (c) The inverted baseline model using the field baseline data. (d) The inverted monitor model using the field monitor data. The target layer is resolved in the inversion results. A comparison of both inverted models reveals that FWI reproduces identical subsurface structures using both field datasets.

Since the true subsurface conditions are unknown, direct QC of the reservoir change results is not feasible. Instead, we use synthetic seismic data generated from a time-lapse model that closely matches the real geological conditions for inversion. The entire inversion process is repeated, and QC is performed by comparing the inversion results of the field data with those of the synthetic data. A reliable field data inversion result should closely align with the synthetic data inversion result. The true synthetic time-lapse model and the baseline model (also obtained by Gaussian smoothing the well log data) are shown in Figure 4.5c and e. We use the same workflow and acquisition geometry as in the field data inversion. In Figure 4.5d and f, we present the inverted time-lapse change using the parallel strategy and the inverted baseline model. The synthetic test replicates the results observed in the field data, showing a clear time-lapse change within the thin layer. This consistency between synthetic and field results confirms the capability of FWI to effectively detect and identify

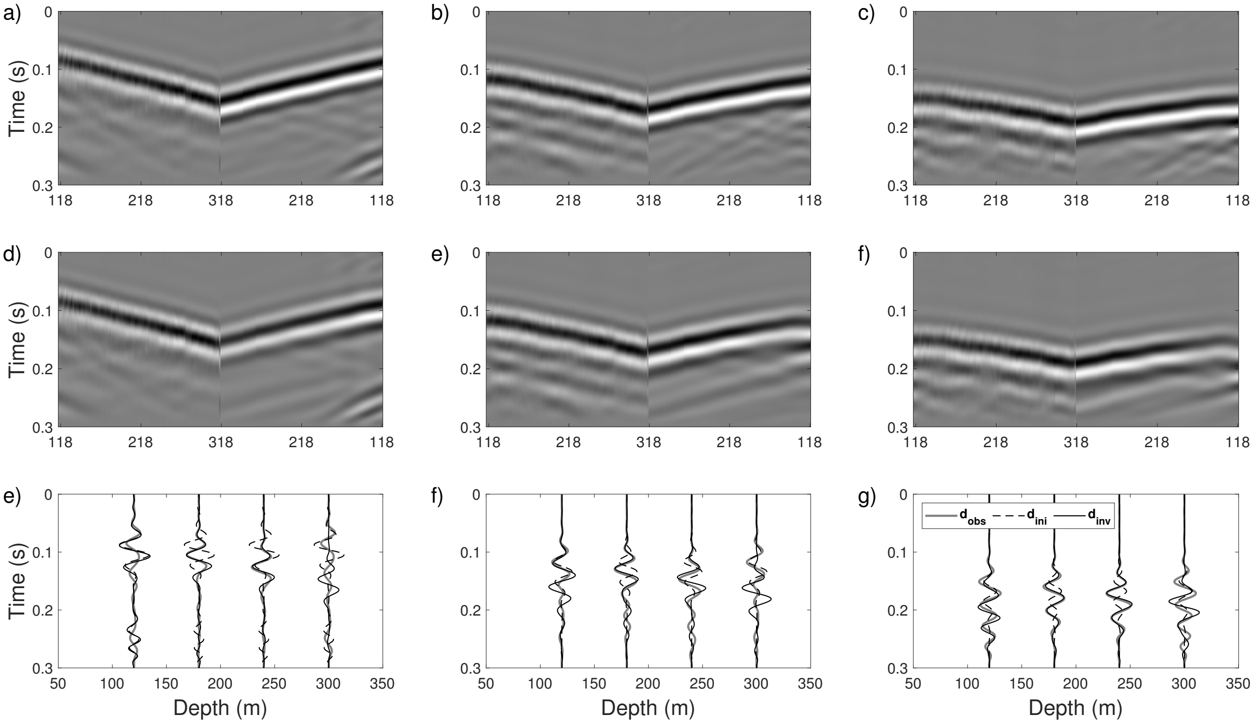

Figure 4.4: Comparison of field baseline data, simulated data from the initial model, and simulated data from the inverted baseline model. The offsets of three gathers (left to right) are 90, 190, and 290 m, respectively. In the first two rows, on the left side of each panel are the field baseline data. On the right side of (a) to (c) are the simulated data using the initial model. On the right side of (d) to (f) are the simulated data using the inverted baseline model. The last row presents the extracted traces from all datasets, spaced at 60 m intervals.

time-lapse changes in the reservoir.

4.5 Discussions

Certain limitations affect the accuracy of the time-lapse inversion. The initial model is based on the Vp well log between 61 m and 337 m, leaving the near-surface velocity profile poorly constrained. Additionally, the absence of initial models for Vs and density further complicates the inversion, as natural elastic effects present in the field data are not accounted for. Observed differences in the data include not only the upgoing reflected waves from the target layer but also components commonly referred to as 4D noise. Despite these challenges, the results underscore the effectiveness of FWI for monitoring CO_2 injection. Future work could address these limitations by incorporating more detailed near-surface information and developing advanced methods to mitigate 4D noise. Such improvements would enhance the accuracy and robustness of time-lapse FWI for reservoir monitoring.

4.6 Conclusions

The application of FWI to baseline and monitor VSP datasets at the FRS demonstrates its feasibility for CO_2 injection monitoring. The time-lapse results from both the field and synthetic data show that this technology can produce high-resolution models of reservoir properties and effectively detect time-lapse velocity changes. This study provides clear evidence that a small-scale CO_2 injection in a shallow 7 m-thick reservoir can be monitored using FWI, offering valuable insights into CO_2 storage dynamics. The results also highlight the potential of time-lapse FWI for small-scale, real-time monitoring, especially when integrated with permanently installed distributed acoustic sensing (DAS) systems as discussed in the next chapter . Moreover, this small-scale injection project establishes a foundation for extending the approach to larger-scale deployments in the future.

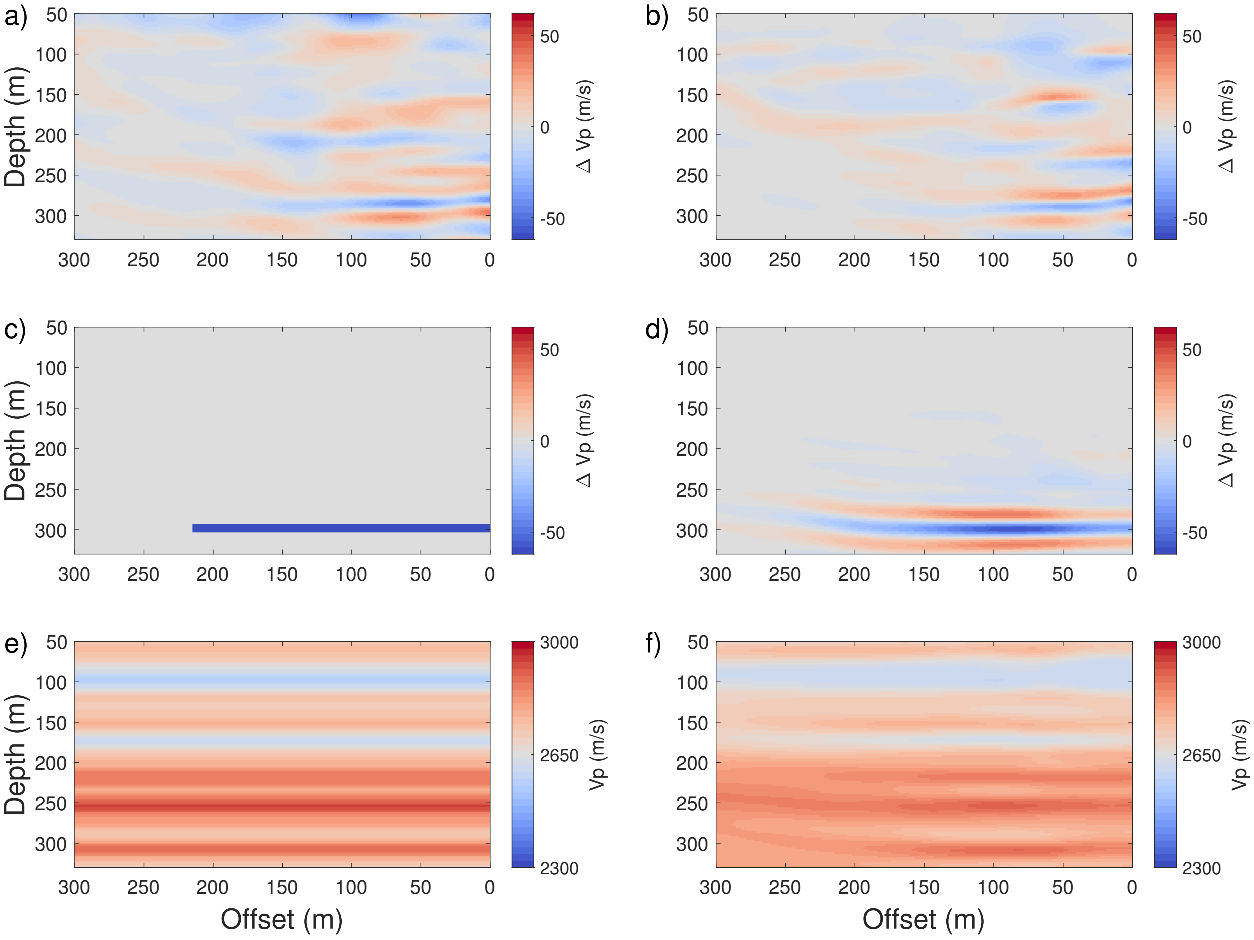

Figure 4.5: (a) The inverted time-lapse change using field data by the parallel strategy. (b) The inverted time-lapse change using field data by the common-model strategy. (c) The true time-lapse model, and the thickness of time-lapse anomaly aligns to the target layer. (d) The inverted time-lapse change using synthetic data. (e) The true baseline model. (f) The inverted baseline model using synthetic data. The results demonstrate that the time-lapse change is captured.

Chapter 5

Time-lapse FWI using field DAS data at CaMI

Time-lapse full-waveform inversion (FWI) using vertical seismic profile (VSP) data has shown great promise for cost-effective and long-term monitoring of CO_2 injection and sequestration. Compared to conventional receivers, Distributed Acoustic Sensing (DAS) offers advantages such as high spatial sampling, long-term deployment, and lower costs, making it particularly well-suited for CO_2 monitoring. While time-lapse FWI with VSP data has demonstrated high-resolution imaging capabilities for tracking reservoir changes due to CO_2 storage, its application to field data remains limited, primarily due to its sensitivity to non-repeatable noise. A recent study has explored FWI using combined single-source DAS and accelerometer VSP data, yet its effectiveness for long-term monitoring remains unverified. To address this gap, we conduct a field experiment using time-lapse walkaway DAS VSP data and FWI to monitor long-term subsurface changes induced by CO_2 injection. We present a workflow that applies FWI to detect time-lapse anomalies associated with the injection of less than 60 tons of CO_2 into a 7 m-thick shallow reservoir. Our results demonstrate the capability of DAS-based FWI to achieve high-resolution inversion and accurately track small-scale CO_2-induced changes. This study highlights the feasibility of leveraging DAS for long-term, high-resolution CO_2 monitoring in real field conditions.

5.1 Introduction

In the previous chapters, I have introduced field cases of CO_2 sequestration and monitoring, as well as the CO_2 monitoring project and geologic background at the CaMI.FRS. Previous studies have demonstrated the potential of full-waveform inversion (FWI) for CO_2 monitoring using both conventional and fiber-optic measurements. For example, Eaid et al. (2023) and Zhang et al. (2025) investigated FWI using combined accelerometer and DAS VSP data, providing early evidence that integrating the two sensing technologies can enhance subsurface imaging. Building on this direction, Cai et al. (2024) implemented time-lapse FWI with real-time, single-source DAS and accelerometer VSP data at CaMI, demonstrating that FWI can capture short-term injection-related changes using field DAS measurements. Furthermore, Ji et al. (2024) extended the investigation to a fully 3D setting, exploring the feasibility of applying 3D time-lapse FWI to accelerometer VSP data and highlighting the potential for high-resolution monitoring in more complex geometries. In Chapter 4, I have conducted time-lapse FWI for field walkway VSP accelerometer data to identify the time-lapse change within the target layer. In this chapter, I conduct a field experiment using walkaway DAS VSP data and FWI to track long-term subsurface changes. Specifically, we monitor a thin (7-meter), shallow (approximately 300 m deep) reservoir following the injection of less than 60 tons of CO_2. This work provides new insights into the feasibility of using DAS-based FWI for high-resolution, long-term CO_2 monitoring. The theory section is consistent with the last chapter and omitted here. Hence, I first review the DAS datasets, describe data matching process, time-lapse strategy and results. Then, I verify the time-lapse result using a synthetic test.

5.1.1 Datasets review

In our 2D FWI for CO_2 monitoring, among all the 13 shot lines in the Snowflake dataset, we chose the shot gathers from line 1 because this line has well-repeated source locations. As depicted in Fig 4.1, the blue stars denote the sources deployed at the surface from the southwest to the observation well, in which the red rectangles denote the deployed receivers. In this 2D walkway VSP DAS acquisition, the offset varies from 470 m to 20 m, there are a total of 29 shot gathers, the minimum distance between two source locations is 10 m, and the maximum distance between two source locations is 90 m. The depth of DAS channels is from the surface to 342 m deep. In the datasets, because most of the signals occur in the first 500 ms, we windowed the data within the first 300 ms which contains direct and reflected waves from the BBRS layer. For both datasets, the preprocessing procedure is conducted following the workflow in Table 5.1 (Cai et al., 2024).

Table 5.1: DAS data processing workflow

DAS data processing
Geometry assignment
Conversion of strain-rate data to strain data
Curvelet-transform-based denoising
Bandpass Butterworth filtering (5–100 Hz)
Median filtering to suppress spike and artifact noise
Time-domain resampling to dt = 0.3 ms
Spatial-domain resampling to dr = 2 m

5.1.2 Data matching

To achieve a successful imaging of time-lapse change in the reservoir where the CO_2 was injected, the datasets from baseline and monitor surveyed have to be well-matched. To cope with the data-matching issue in the DAS VSP datasets, we propose an appoach following the steps below. At first, we also balance the energy of each shot-gather pairs in both datasets, which assures the amplitude of both datasets is at the same level. Second, we separate the upgoing and downgoing waves in the VSP shot gathers using f-k filters. In this way, we can obtain the upgoing reflected waves from the BBRS layer, which are expected to result in the data difference introduced by the CO_2 injection. After the wavefield separation, we calculate a filter based on a spectral balancing filter or matching filter using the downgoing waves in each shot-gather pair. A spectral balancing filter or matching filer is designed to match the amplitude, time delay, and spectra of two traces, making them almost identical. Since in a time-lapse survey, the physical parameters above the time-lapse change area are expected to remain the same, hence the downgoing waves received by the receivers above the injection reservoir should be almost identical. Adopting a spectral balancing filter or matching filter will make the downgoing waves well-matched and eliminate the 4D noise introduced by velocity change at shallow depths and data acquisition. Then we apply the calculated filters to the upgoing waves in the baseline datasets followed by a time-shift correction. Then we sum up the matched downgoing and upgoing waves as the matched baseline datasets.

In practice, we only match the datasets with receivers located below 120 m. Since at shallow depth, there are strong shearing effects not removed by preprocessing. After adopting this new workflow, we found that some shot-gather pairs still could not be matched due to some limitations of the field datasets. First of all, the quality of the baseline datasets is quite poor compared with the monitor datasets, we can't even observe the reflection from the BBRS layer in some shot gathers. Second, the acquired downgoing and/or upgoing waves in a shot-gather pair are not comparable. We tried with all the shot-gather pairs with 29 well-repeated source locations and matched only 10 of them. In Fig 5.1, we present one matched data example at an offset of 60 m. In the first row of Fig 5.1, we present the separated upgoing waves in monitor data, baseline data, and their difference at an offset of 60 m. In the second row of Fig 5.1, we respectively present the matched baseline data and the data difference after the data-matching workflow. From this comparison, we can notice the data difference introduced by the BBRS reflection is well enhanced, and the 4D noise that existed at the bottom right is well mitigated.

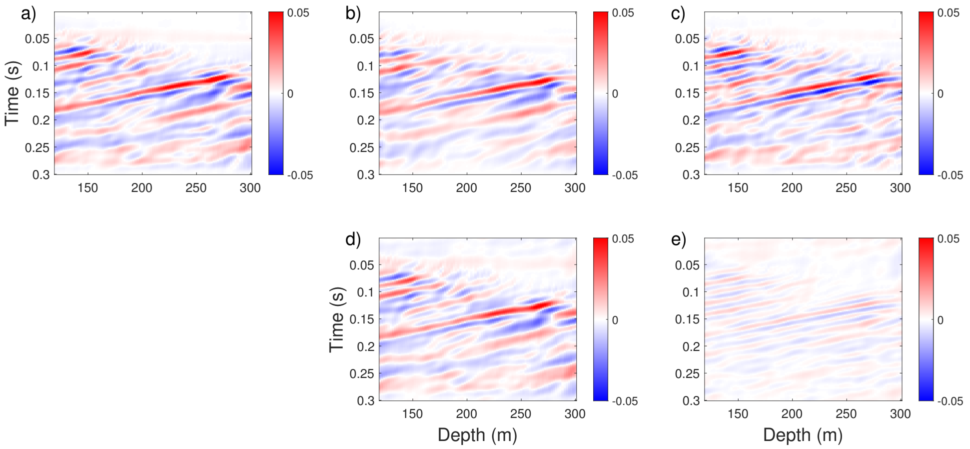

Figure 5.1: Separated upgoing waves in (a) monitor data, (b) baseline data, and (d) matched baseline data at an offset of 60 m. (d) is the data difference before the data-matching workflow, and (e) is the data difference after the data-matching workflow.

5.1.3 Time-lapse inversion strategy

In the previous section, we described the data matching workflow and presented the matched data examples. However, the matched baseline dataset consists of only 10 gathers with 90 receivers, which is insufficient for directly applying FWI to obtain a baseline model comparable to the monitor model. To address this limitation, I use the target-oriented common-model strategy (TO CMS) (Liu et al., 2025) in chapter 3 for this scenario. Given the higher quality of the monitor dataset, we first apply FWI to the monitor dataset to obtain an inverted monitor model, which serves as the initial model for the second stage of CMS. In the second stage, we perform FWI on the matched baseline dataset, using the newly obtained initial model, despite its limited acquisition geometry. During the inversion, we precondition the gradient and prevent the model at shallow depths from updating (Fu et al., 2024). To ensure localized convergence, we then reapply FWI to the monitor dataset, using the same acquisition geometry as the matched baseline dataset. Finally, we obtain the time-lapse result by subtracting the inverted baseline model from the inverted monitor model after the second stage.

5.1.4 Results

As in chapter 4, the VSP DAS data inversion workflow follows the traditional FWI technology (Tarantola, 1984) implemented in an open-source software package IFOS2D (Bohlen et al., 2016a; Köhn, 2011). Given the thin 7-meter Basal Belly River Sandstone (BBRS) reservoir where CO_2 was injected, achieving high-resolution inversion is essential for reservoir identification. To meet this requirement, we use data with frequency components up to 60 Hz and set the grid cell size to 2 m. Both datasets are resampled with a receiver interval of 2 m, spanning depths from 2 m to 342 m, and a temporal interval of 0.3 ms. The free surface condition (Levander, 1988) is implemented on top of the model. At the sides and the bottom of the model, there are 20 layers of Perfectly Matched Layers (PMLs) (Komatitsch and Martin, 2007) implemented as the absorbing boundary condition in the finite difference modeling. For inversion, we employ a filtered Klauder wavelet, which is shown in Fig 5.2. The initial model is same as in chapter 4 shown in Fig 4.3a, which is constructed by applying Gaussian smoothing to the well log data from 61 to 337 m, and then extended into a 2D model.

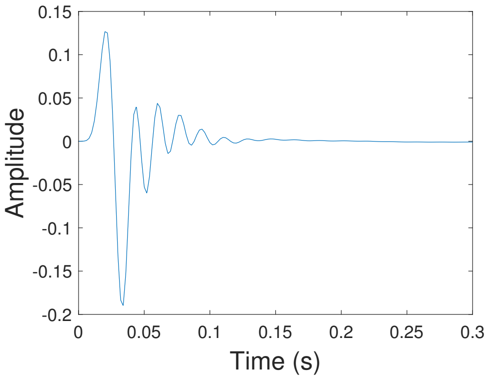

Figure 5.2: The Klauder wavelet with minimum phase filtered with the same bandpass applied to baseline and monitor datasets. This wavelet is used for baseline and monitor model inversion using Snowflake datasets.

In Fig 5.3, we present the inverted monitor model, in which the observation well is located at 0 m. The maximum offset of the source location in our inversion is 470 m. We display part of the model with effective model updates within a 300 m offset. Comparing this inverted model with the initial Vp model shown in Fig 4.3a, we can see that FWI introduces many details into the smooth initial model. The target layer can be identified in the inversion result at a depth of around 300 m, where the CO_2 was injected.

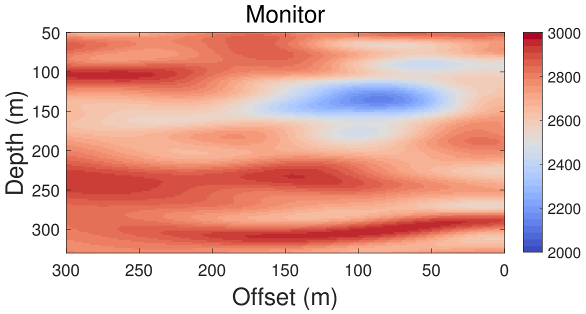

Figure 5.3: Inverted baseline Vp model using the baseline dataset from the northwest to the observation well in line 4 with an offset ranging from 20 m to 470 m. Maximum offset of 300 m of inverted Vp model with effective model updates is depicted.

For quality control, in Fig 5.4, we present the comparison of field monitor data, simulated data using the initial model, and simulated data using the inverted model shown in Fig 5.3 at offsets 100, 200, and 350 m. In Fig 5.5, we respectively extract 4 traces with a spatial interval of 60 m from observed data, initial data, and inverted data in the shot gathers with offsets being 100, 200, and 350 m for comparison.

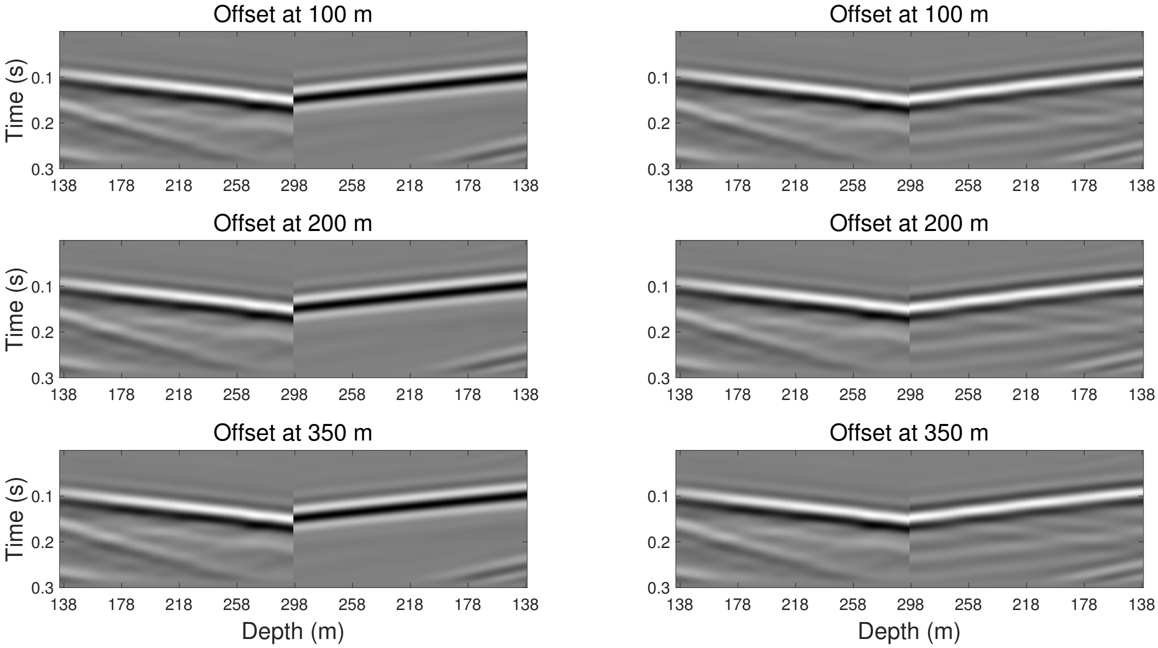

Figure 5.4: Comparison of field monitor data with simulated data from the initial and inverted monitor models. The left side of each panel shows the field data. In the left column, the right side of each panel presents simulated data from the initial model, while in the right column, the right side of each panel displays simulated data from the inverted model.

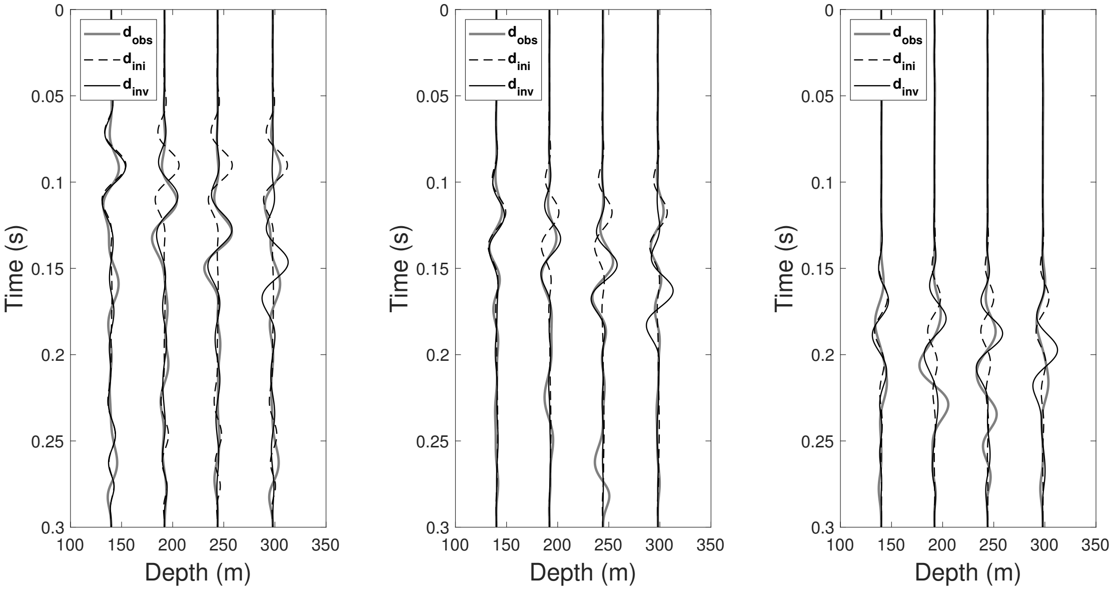

Figure 5.5: Comparison of traces extracted with a spatial interval of 60 m from observed data, initial data, and inverted data in the shot gathers with offsets being 100, 200, and 350 m. The bold gray lines denote the traces from observed data, the black dashed lines denote the simulated data using the initial model, and the solid black lines denote the simulated data using the final inverted model.

After the monitor model inversion, we perform the FWI of the monitor model and baseline model using the first inverted monitor model as the new initial model with matched datasets. The results are presented in Fig 5.6. From the comparison, we can see that applying FWI to two matched datasets provides identical structures.

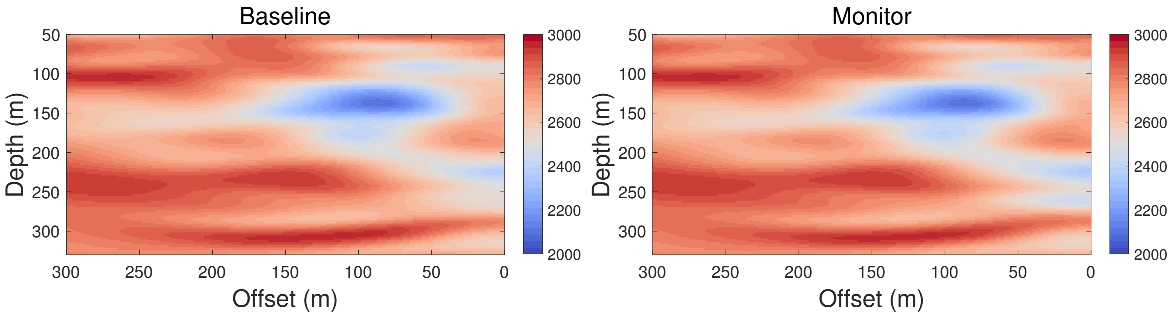

Figure 5.6: (a) The inverted baseline model using matched baseline dataset using the first inverted monitor model as the new initial model. (b) The inverted monitor model using matched monitor dataset using the first inverted monitor model as the new initial model.

To further evaluate the inversion results, we compare the smoothed well log from the observation well, the initial model, and the vertical profiles from the inverted baseline and monitor models at 0 m offset, as shown in Fig 5.7. We can see that two inverted models show good agreement.

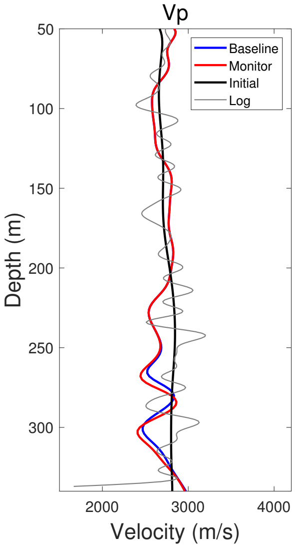

Figure 5.7: Comparison of the smoothed Vp Log from the injection well 20 m away to the northeast of the observation well at offset 0 m, the 1D initial Vp model, and the vertical profiles of the observation well in the inverted baseline and monitor Vp models at 0 m offset. The gray line denotes the smoothed Vp log, the bold black line denotes the 1D initial Vp model, and the blue and red lines denote the vertical profiles of the observation well in the inverted baseline and monitor Vp models at 0 m offset, respectively.

Finally, we obtain the time-lapse change introduced by CO_2 injection by subtracting the two inverted models, as shown in Fig 5.9a. From this figure, we can see the time-lapse change is successfully captured within the thin target layer at a shallow depth. However, due to the limited source illumination from only 10 matched datasets, the resolution of the time-lapse result may also be constrained. Additionally, we also notice the time-lapse noise above the reservoir, resulting from the 4D noise that's not fully eliminated in the matched datasets. For verification, we conduct a synthetic test. The true time-lapse and monitor models are shown in Fig 5.9c and 5.9e. while the synthetic time-lapse result is presented in Fig 5.9b. A comparison between the field and synthetic results reveals similar time-lapse patterns using the same workflow, confirming the reliability of our approach.

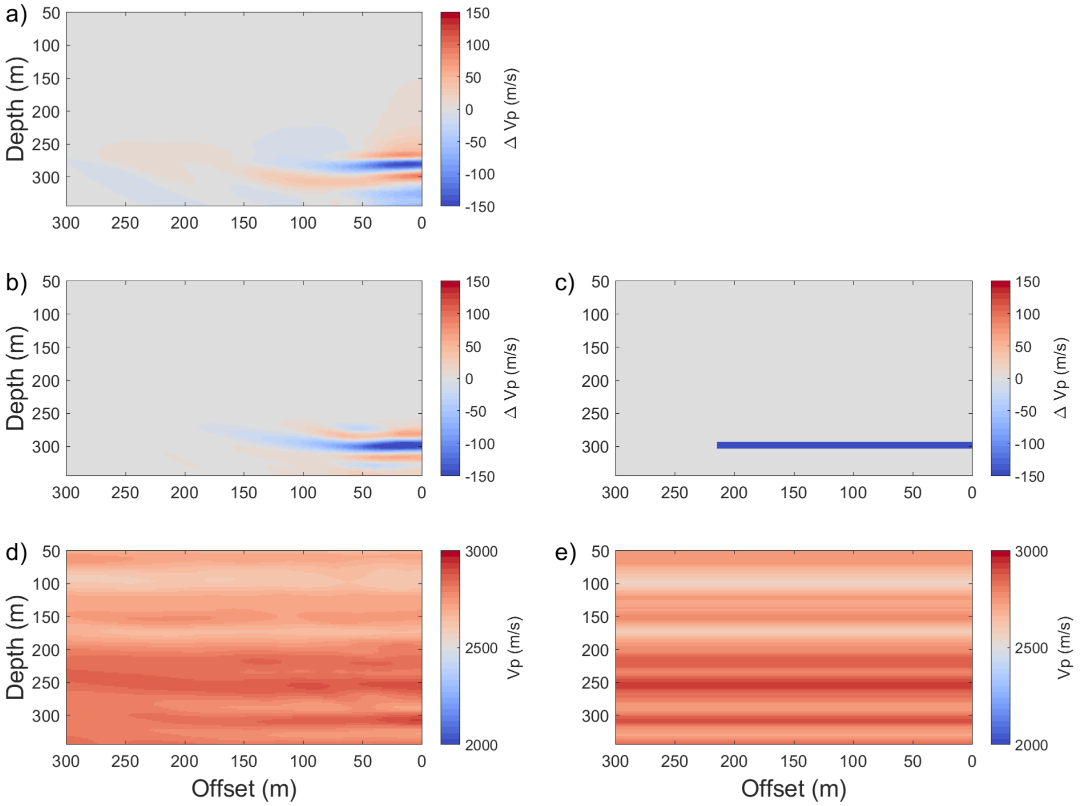

Figure 5.8: (a) The time-lapse result using the matched field data limited acquisition geometry and the target-oriented strategy. (b) The time-lapse result using synthetic data and the same workflow. (c) The true time-lapse model for synthetic test. (d) The inverted monitor model using synthetic data. (e) The true monitor model for synthetic test, which is also obtained by Gaussian smoothing the well log.

At last, we compare the time-lapse results using both accelerometer and DAS VSP datasets. We can see that, the application of FWI to both datasets provides similar time-lapse images, and with much larger offsets, the plume is better imaged due to better illumination. howver, we can also notice that the value of time-lapse anomaly is different.

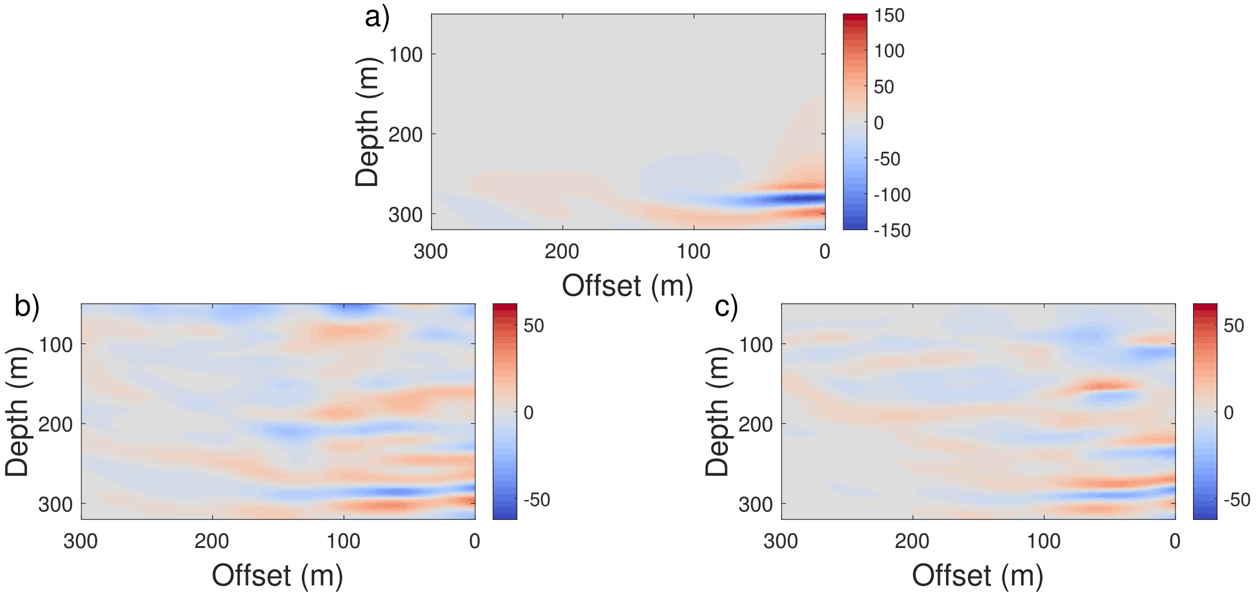

Figure 5.9: Time-lapse inversion results from (a) matched-field DAS VSP data acquired with limited acquisition geometry and the target-oriented common-model strategy, (b) field accelerometer VSP data and the parallel strategy, and (c) field accelerometer data and the common-model strategy. Panel (a) uses 10 shots and 70 receivers with offsets from 60 to 220 m, whereas panels (b) and (c) use 47 shots and 159 receivers with offsets from 10 to 480 m.

5.2 Discussions

In this work, we focus only on detecting time-lapse changes within the target reservoir. However, time-lapse variations may also occur in the overburden, which could potentially indicate CO_2 or other fluid leakage — a critical concern for storage integrity and long-term monitoring.

Due to the limited quality and repeatability of the field DAS data, the target-oriented common-model strategy (TO-CMS) proposed in Chapter 3 is adopted as a practical solution. Although this approach effectively helps identify local velocity changes within the reservoir, it may reduce our sensitivity to subtle anomalies associated with CO_2 leakage in the overburden. Therefore, applying the target-oriented strategy represents a practical but necessary compromise when conducting time-lapse FWI.

At the current stage of research on time-lapse FWI strategies, the primary focus remains on detecting velocity changes within the reservoir. The numerical experiments presented in Chapter 3 demonstrate that even under controlled conditions, identifying subtle time-lapse anomalies is still highly challenging. At present, we are not yet able to reliably detect such small changes, particularly in field data where noise, acquisition differences, and non-repeatability further complicate the inversion — let alone the even subtler signals that might be introduced by CO_2 leakage. Future research should aim to develop more advanced inversion approaches that enhance both sensitivity and robustness, enabling the distinction between genuine reservoir changes and overburden anomalies. Such developments will be essential for improving the reliability of time-lapse FWI in assessing and ensuring the long-term safety of CO_2 sequestration operations.

This work also suffers from the same limitations discussed in Chapter 4, including the absence of P-wave velocity well logs at shallow depths and the lack of other elastic parameters. In addition, the DAS VSP data exhibit relatively poor quality. To mitigate the influence of strong near-surface noise, the data recorded at shallow depths were excluded from the data-matching process.

These limitations primarily affect the shallow section of the model but have only a minor influence on the time-lapse change interpretation, which remains the main focus of this study.

5.3 Conclusions

This study demonstrates the feasibility of applying time-lapse full-waveform inversion (FWI) to field distributed acoustic sensing (DAS) vertical seismic profile (VSP) data for CO_2 sequestration monitoring. The results highlight the potential of integrating DAS with FWI for high-resolution, small-scale CO_2 monitoring in a shallow, thin reservoir. Synthetic experiments further validate the applicability of time-lapse FWI to DAS VSP data, confirming its capability to recover reservoir-scale velocity changes associated with CO_2 injection.

The time-lapse inversion results obtained from both DAS and accelerometer VSP datasets exhibit consistent patterns, reinforcing the reliability and robustness of the proposed workflow. Nevertheless, due to the limited quality and repeatability of the field DAS data, meaningful inversion updates are primarily confined to the reservoir zone. As a practical mitigation, a target-oriented inversion strategy was adopted to concentrate the model updates within this region, ensuring inversion stability while reducing the impact of non-repeatable noise and near-surface inconsistencies.

Overall, this work represents a key step toward establishing a cost-effective, field-deployable time-lapse monitoring framework for CO_2 sequestration using DAS VSP data. The demonstrated approach lays a practical foundation for extending time-lapse FWI to larger-scale and longer-term carbon storage projects, where reliable and continuous subsurface monitoring is essential for ensuring storage security.

Chapter 6

Conclusions

Time-lapse full-waveform inversion (FWI) is a powerful tool for CO_2 monitoring, offering high-resolution imaging of subsurface physical properties to detect reservoir changes during injection, production, and long-term storage. By comparing inversion results from seismic datasets acquired at different times, time-lapse FWI enables the identification and characterization of dynamic reservoir behavior associated with CO_2 injection and sequestration.

This thesis develops a novel time-lapse FWI strategy to address the limitations of conventional approaches, which often rely on a parallel inversion strategy and suffer from significant artifacts and inconsistent convergence between baseline and monitor models due to survey non-repeatability. Specifically, Chapter 3 introduces a target-oriented common-model strategy (TO CMS) that incorporates prior knowledge about the location of reservoir changes into the common-model framework. When combined with the amplitude-encoding technique presented in Chapter 2 to improve computational efficiency, numerical experiments demonstrate that TO CMS improves convergence within the target region and enhances the accuracy of inverted time-lapse changes. The results also suggest that more precise delineation of the target area leads to improved imaging. Nonetheless, the experiments indicate that strong noise and variations in seawater velocity can significantly impair inversion performance—issues that warrant further investigation.

Chapter 4 explores the feasibility of CO_2 monitoring using time-lapse FWI and vertical seismic profile (VSP) data acquired at the Field Research Station (FRS). In this field experiment, accelerometer-based VSP data are used to construct high-resolution velocity models that successfully capture subtle time-lapse changes in reservoir properties. The results clearly demonstrate that even small-scale CO_2 injections into a shallow, 7-meter-thick reservoir can be effectively monitored using time-lapse FWI. These findings also underscore the potential of time-lapse FWI for real-time, high-resolution subsurface monitoring, particularly when integrated with distributed acoustic sensing (DAS) technology.

Building on this, Chapter 5 presents a second field experiment using DAS-based VSP data. To mitigate the impact of strong near-surface noise, shallow-depth recordings were excluded from the data matching process. Despite the limited acquisition geometry, the use of the TO CMS strategy—employing the monitor model from the first stage as the initial model—enabled successful application of time-lapse FWI to both the baseline and monitor DAS datasets at the FRS. The resulting time-lapse velocity changes exhibit strong agreement with synthetic benchmarks, validating the robustness and reliability of the proposed workflow. This study confirms the feasibility of integrating DAS data with FWI for small-scale CO_2 monitoring in shallow, thin reservoirs.

Together, these two field experiments demonstrate the practical viability of time-lapse FWI for monitoring small-scale CO_2 injection projects and lay a foundation for its extension to larger-scale and long-term deployments. The findings of this thesis highlight the effectiveness of advanced time-lapse FWI strategies, the feasibility of using VSP data for monitoring small-scale CO_2 injection and sequestration, as well as the potential of integrating DAS data into time-lapse FWI workflows for high-resolution, real-time subsurface monitoring under challenging field conditions.

Bibliography

Ajo-Franklin J, Wagner A, Lindsey N, et al. (2016) Using distributed fiber-optic methods to track a changing landscape: combining das tomography, dss, & dts for timelapse permafrost monitoring. In: SEG Postconvention workshop W-10: Fiber-optic Sensing for Exploration and Monitoring: Development, Applications, and Challenges, Dallas, TX, USA

Ancelle C, Lord NE, Wang HF, et al. (2014) Directivity and sensitivity of fiber-optic cable measuring ground motion using a distributed acoustic sensing array. In: 2014 AGU Fall Meeting, San Francisco, CA, USA, abstract NS31C-3935

Arts R, Eiken O, Chadwick A, et al. (2004a) Monitoring of co2 injected at sleipner using time-lapse seismic data. Energy 29(9–10):1383–1392. `https://doi.org/10.1016/j.energy.2004.03.072`

Arts R, Eiken O, Chadwick A, et al. (2004b) Monitoring of co2 injected at sleipner using time-lapse seismic data. Energy 29(9-10):1383–1392

Bachu S (2000) Sequestration of co2 in geological media: Criteria and approach for site selection in response to climate change. Energy Conversion and Management 41(9):953–970. `https://doi.org/10.1016/S0196-8904(99)00149-1`

Bachu S (2008) Co2 storage in geological media: Role, means, status and barriers to deployment. Progress in Energy and Combustion Science 34(2):254–273. `https://doi.org/10.1016/j.pecs.2007.10.001`

Barkved O, Buer K, Halleland K, et al. (2003) 4d seismic response of primary production and waste injection at the valhall field. In: 65th EAGE Conference & Exhibition, EAGE Publications BV, pp cp–6

Barkved OI, Kristiansen T, Fjær E (2005) The 4d seismic response of a compacting reservoir-examples from the valhall field, norway. In: 2005 SEG Annual Meeting, OnePetro

Benson SM, Cole DR (2008) Carbon dioxide capture and storage: Issues and prospects. Annual Review of Environment and Resources 33:117–142

Biondi E, Barnier G, Biondi B, et al. (2023) Target-oriented elastic full-waveform inversion through acoustic extended image-space redatuming. Geophysics 88(3):R269–R296

Blacquiere G, Berkhout G, Verschuur E (2009) Survey design for blended acquisition. In: SEG Technical Program Expanded Abstracts 2009. Society of Exploration Geophysicists, p 56–60

Bohlen T, De Nil D, Köhn D, et al. (2016a) Sofi2d seismic modeling with finite differences: 2d—elastic and viscoelastic version. user guide

Bohlen T, Nil D, Groos L, et al. (2016b) Ifos2d, version 2.0. 3

Bortoni S, Barragan S, Azevedo G, et al. (2021) Learnings from an fwi imaging study using 3d and 4d data over a postsalt field in campos basin. In: SEG/AAPG/SEPM First International Meeting for Applied Geoscience & Energy, OnePetro

Bunks C, Saleck FM, Zaleski S, et al. (1995) Multiscale seismic waveform inversion. Geophysics 60(5):1457–1473

Cai X, Hu Q, Innanen KA, et al. (2024) Rapid-repeat time-lapse vertical seismic profile imaging of co2 injection. Geophysics 90(2):1–36

Chadwick R, Noy D, Arts R, et al. (2009) Latest time-lapse seismic data from sleipner yield new insights into co2 plume development. Energy Procedia 1(1):2103–2110

Choi Y, Alkhalifah T (2012) Application of multi-source waveform inversion to marine streamer data using the global correlation norm. Geophysical Prospecting 60(4-Simultaneous Source Methods for Seismic Data):748–758

Cui T, Rickett J, Vasconcelos I, et al. (2020) Target-oriented full-waveform inversion using marchenko redatumed wavefields. Geophysical Journal International 223(2):792–810

Dai W, Fowler P, Schuster GT (2012) Multi-source least-squares reverse time migration. Geophysical Prospecting 60(4-Simultaneous Source Methods for Seismic Data):681–695

Daley TM, Freifeld BM, Ajo-Franklin J, et al. (2013) Field testing of fiber-optic distributed acoustic sensing (DAS) for subsurface seismic monitoring. The Leading Edge 32:699–706. `https://doi.org/10.1190/tle32060699.1`

Daley TM, Miller DE, Dodds K, et al. (2016) Field testing of fiber-optic distributed acoustic sensing for monitoring of co2 injection at otway, australia. International Journal of Greenhouse Gas Control 45:25–35. `https://doi.org/10.1016/j.ijggc.2015.12.005`

De Ridder S, Biondi B, Clapp R (2014) Time-lapse seismic noise correlation tomography at valhall. Geophysical Research Letters 41(17):6116–6122

Dou S, Lindsey NJ, Wagner AM, et al. (2017) Distributed acoustic sensing for seismic monitoring of the near surface: a traffic-noise interferometry case study. Scientific Reports 7:11,620. `https://doi.org/10.1038/s41598-017-11986-4`

Eaid MV, Keating SD, Innanen KA, et al. (2023) Field assessment of elastic full-waveform inversion of combined accelerometer and distributed acoustic sensing data in a vertical seismic profile configuration. Geophysics 88(6):WC163–WC180

Egorov A, Pevzner R, Bóna A, et al. (2017) Time-lapse full waveform inversion of vertical seismic profile data: Workflow and application to the co2crc otway project. Geophysical Research Letters 44(14):7211–7218

Eiken O, Ringrose P, Hermanrud C, et al. (2011) Lessons learned from 14 years of ccs operations: Sleipner, in salah and snøhvit. Energy procedia 4:5541–5548

Florez KA, Mantilla JG, Ramirez AB (2016) Full waveform inversion (fwi) in time for seismic data acquired using a blended geometry. In: 2016 XXI Symposium on Signal Processing, Images and Artificial Vision (STSIVA), IEEE, pp 1–5

Fu X, Innanen KA (2022a) A time-domain, multi-source bayesian/markov chain monte carlo formulation of time-lapse seismic waveform inversion. Geophysics 87(4):1–110

Fu X, Innanen KA (2022b) Time-lapse seismic imaging using shot gathers with non-repeatable source wavelets. Geophysics 88(1):1–108

Fu X, Innanen KA (2023) Stepsize sharing in time-lapse full-waveform inversion. Geophysics 88(2):M59–M70

Fu X, Romahn S, Innanen KA (2023) Double-wavelet time-lapse full-waveform inversion. Canadian Journal of Exploration Geophysics 46(1):1–19

Fu X, Liu H, Innanen KA, et al. (2024) Time-lapse 4d full-waveform inversion for ocean-bottom cable seismic data with seawater velocity changes. Geophysics 90(2):1–89

Godwin J, Sava P (2013) A comparison of shot-encoding schemes for wave-equation migration. Geophysical Prospecting 61:391–408

Greaves RJ, Fulp TJ (1987) Three-dimensional seismic monitoring of an enhanced oil recovery process. Geophysics 52(9):1175–1187

Hall K, Lawton DC, Daley TM, et al. (2018) Effect of source effort and source distance on DAS data at CaMI.FRS, Newell County, Alberta. GeoConvention pp 1–4

Hall KW, Bertram KL, Bertram M, et al. (2019a) Simultaneous accelerometer and optical fibre multi-azimuth walk-away vsp experiment: Newell county, alberta, canada. In: SEG International Exposition and Annual Meeting, SEG, p D043S111R007

Hall KW, Bertram KL, Bertram M, et al. (2019b) Simultaneous accelerometer and optical fibre multi-azimuth walk-away VSP experiment: Newell County, Alberta, Canada. In: SEG Technical Program Expanded Abstracts 2019. Society of Exploration Geophysicists, p 5340–5344

Hicks E, Hoeber H, Houbiers M, et al. (2016) Time-lapse full-waveform inversion as a reservoir-monitoring tool—a north sea case study. The Leading Edge 35(10):850–858

Hu J, Wang H, Fang Z, et al. (2016) Efficient amplitude encoding least-squares reverse time migration using cosine basis. Geophysical prospecting 64(6):1483–1497

Huang R, Zhang Z, Wu Z, et al. (2021) Full-waveform inversion for full-wavefield imaging: Decades in the making. The Leading Edge 40(5):324–334

Huang X, Jakobsen M, Nævdal G, et al. (2020) Target-oriented inversion of time-lapse seismic waveform data. Communications in Computational Physics 28(1):249–275

Innanen K, Hall KW, Lawton DC (2022) A time-lapse multi-offset, multi-azimuth vsp acquired as a candidate for low-cost monitoring of co2 injection and storage. In: CSEG, CSEG, p D043S111R007

Ji HG, Innanen KA, Park SE, et al. (2024) 3d full-waveform inversion of the" snowflake" baseline dataset: towards monitoring of co2 storage through inversion of multi-offset, multi-azimuth vsp data at the newell county facility in alberta, canada. IEEE Geoscience and Remote Sensing Letters

Jousset P, Reinsch T, Henninges J, et al. (2017) Crustal exploration and monitoring seismic events with a fibre-optic cable deployed at the ground surface in iceland. In: 79th EAGE Conference and Exhibition, Expanded Abstracts, `https://doi.org/https://doi.org/10.3997/2214-4609.201700169`, fr SRP09

Kazemeini SH, Juhlin C, Fomel S (2010) Monitoring co2 response on surface seismic data; a rock physics and seismic modeling feasibility study at the co2 sequestration site, ketzin, germany. Journal of Applied Geophysics 71(4):109–124

Köhn D (2011) Time domain 2d elastic full waveform tomography [ph. d. thesis]. Kiel: Christian-Albrechts-Universität zu Kiel

Komatitsch D, Martin R (2007) An unsplit convolutional perfectly matched layer improved at grazing incidence for the seismic wave equation. Geophysics 72(5):SM155–SM167

Kotsi M, Malcolm A, Ely G (2020) Uncertainty quantification in time-lapse seismic imaging: A full-waveform approach. Geophysical Journal International 222(2):1245–1263

Krebs JR, Anderson JE, Hinkley D, et al. (2009) Fast full-wavefield seismic inversion using encoded sources. Geophysics 74(6):WCC177–WCC188

Levander AR (1988) Fourth-order finite-difference p-sv seismograms. Geophysics 53(11):1425–1436

Li Y, Alkhalifah T, Guo Q (2021) Target-oriented time-lapse waveform inversion using deep learning-assisted regularization. Geophysics 86(4):R485–R495

Liang L, Li M, Rufino R, et al. (2013) Application of frequency-domain full-waveform inversion for time-lapse 3d vsp data interpretation in an extra heavy oil field. In: SEG International Exposition and Annual Meeting, SEG, pp SEG–2013

Liu H, Fu X, Trad D, et al. (2025) Multi-source time-lapse elastic full-waveform inversion using a target-oriented common-model strategy. IEEE Transactions on Geoscience and Remote Sensing

Liu X, Zhu T, Ajo-Franklin J (2023) Understanding subsurface fracture evolution dynamics using time-lapse full waveform inversion of continuous active-source seismic monitoring data. Geophysical Research Letters 50(4):e2022GL101,739

Lumley D (2010) 4d seismic monitoring of co2 sequestration. The Leading Edge 29(2):150–155. `https://doi.org/10.1190/1.3304817`

Lumley D, Adams DC, Meadows M, et al. (2003) 4d seismic data processing issues and examples. In: SEG Technical Program Expanded Abstracts 2003. Society of Exploration Geophysicists, p 1394–1397

Macquet M, Lawton DC, Saeedfar A, et al. (2019) A feasibility study for detection thresholds of co2 at shallow depths at the cami field research station, newell county, alberta, canada. Petroleum Geoscience 25(4):509–518

Macquet M, Lawton D, Osadetz K, et al. (2022) Overview of carbon management canada's pilot-scale co2 injection site for developing and testing monitoring technologies for carbon capture and storage, and methane detection. Official publication of the Canadian Society of Exploration Geaophysicist

Malcolm A, Willemsen B (2016) Rapid 4d fwi using a local wave solver. The Leading Edge 35(12):1053–1059

Mardan A, Giroux B, Fabien-Ouellet G (2023) Weighted-average time-lapse seismic full-waveform inversion. Geophysics 88(1):R25–R38

Masson-Delmotte V, Zhai P, Pirani A, et al. (2021) Climate change 2021: the physical science basis. Contribution of working group I to the sixth assessment report of the intergovernmental panel on climate change 2(1):2391

Matharu G, Sacchi MD (2018) Source encoding in multiparameter full waveform inversion. Geophysical Journal International 214(2):792–810

Medwin H (1975) Speed of sound in water: A simple equation for realistic parameters. The Journal of the Acoustical Society of America 58(6):1318–1319

Metz B, Davidson O, de Coninck H, et al. (eds) (2005) IPCC Special Report on Carbon Dioxide Capture and Storage. Cambridge University Press, Cambridge, UK and New York, USA, URL `https://www.ipcc.ch/report/carbon-dioxide-capture-and-storage/`

Mordret A, Shapiro NM, Singh S (2014) Seismic noise-based time-lapse monitoring of the valhall overburden. Geophysical Research Letters 41(14):4945–4952

Morse PM, Feshbach H (1954) Methods of theoretical physics. American Journal of Physics 22(6):410–413

Morton SA, Ober CC (1998) Fastershot-record depth migrations using phase encoding. In: SEG Technical Program Expanded Abstracts 1998. Society of Exploration Geophysicists, p 1131–1134

Nakata R, Jang UG, Lumley D, et al. (2022) Seismic time-lapse monitoring of near-surface microbubble water injection by full waveform inversion. Geophysical Research Letters 49(24):e2022GL098,734

Operto S, Gholami A, Aghamiry H, et al. (2023) Extending the search space of full-waveform inversion beyond the single-scattering born approximation: A tutorial review. Geophysics 88(6):R671–R702

Pan W (2017) Waveform inversion for estimating subsurface properties: phase-encoding strategies, optimization methods, interparameter tradeoffs quantification and reduction. PhD thesis

Pevzner R, Urosevic M, Popik D, et al. (2017) 4d surface seismic tracks small supercritical co2 injection into the subsurface: Co2crc otway project. International Journal of Greenhouse Gas Control 63:150–157

Pica A, Diet J, Tarantola A (1990) Nonlinear inversion of seismic reflection data in a laterally invariant medium. Geophysics 55(3):284–292

Plessix RE (2006) A review of the adjoint-state method for computing the gradient of a functional with geophysical applications. Geophysical Journal International 167(2):495–503

Plessix RE, Michelet S, Rynja H, et al. (2010) Some 3d applications of full waveform inversion. In: 72nd EAGE Conference and Exhibition-Workshops and Fieldtrips, European Association of Geoscientists & Engineers, pp cp–162

Ringrose P, Meckel T (2019) Maturing global co2 storage resources on offshore continental margins to achieve 2ds emissions reductions. Scientific Reports 9(17944):1–10. `https://doi.org/10.1038/s41598-019-54363-z`

Romero LA, Ghiglia DC, Ober CC, et al. (2000) Phase encoding of shot records in prestack migration. Geophysics 65(2):426–436

Ross CP, Altan MS (1997) Time-lapse seismic monitoring: Some shortcomings in nonuniform processing. The Leading Edge 16(6):931–937

Routh P, Palacharla G, Chikichev I, et al. (2012) Full wavefield inversion of time-lapse data for improved imaging and reservoir characterization. In: 2012 SEG Annual Meeting, OnePetro

Symes WW (2008) Migration velocity analysis and waveform inversion. Geophysical prospecting 56(6):765–790

Tarantola A (1984) Inversion of seismic reflection data in the acoustic approximation. Geophysics 49(8):1259–1266

Tsitsas NL (2010) On block matrices associated with discrete trigonometric transforms and their use in the theory of wave propagation. Journal of Computational Mathematics pp 864–878

Valenciano AA, Biondi B, Guitton A (2006) Target-oriented wave-equation inversion. Geophysics 71(4):A35–A38

Vinje V, Martinez R, Ringrose P (2025) A breakthrough in the imaging of a co2 plume—using obn data to the full. First Break 43(6):83–87

Virieux J (1986) P-sv wave propagation in heterogeneous media: Velocity-stress finite-difference method. Geophysics 51(4):889–901

Virieux J, Operto S (2009) An overview of full-waveform inversion in exploration geophysics. Geophysics 74(6):WCC1–WCC26

Virieux J, Asnaashari A, Brossier R, et al. (2017) An introduction to full waveform inversion. In: Encyclopedia of exploration geophysics. Society of Exploration Geophysicists, p R1–1

Walter F, Gräff D, Lindner F, et al. (2020) Distributed acoustic sensing of microseismic sources and wave propagation in glaciated terrain. Nature communications 11(1):1–10

Wang Z, Cates ME, Langan RT (1998) Seismic monitoring of a co 2 flood in a carbonate reservoir; a rock physics study. Geophysics 63(5):1604–1617

Watanabe T, Shimizu S, Asakawa E, et al. (2004) Differential waveform tomography for time-lapse crosswell seismic data with application to gas hydrate production monitoring. In: SEG technical program expanded abstracts 2004. Society of Exploration Geophysicists, p 2323–2326

Wright I, Ringrose P, Mathieson A, et al. (2009) An overview of active large-scale co2 storage projects. In: SPE International Conference on CO2 Capture, Storage, and Utilization, SPE, pp SPE–127,096

Yang D, Malcolm A, Fehler M, et al. (2014) Time-lapse walkaway vertical seismic profile monitoring for co2 injection at the sacroc enhanced oil recovery field: A case study. Geophysics 79(2):B51–B61

Yang D, Meadows M, Inderwiesen P, et al. (2015a) Double-difference waveform inversion: Feasibility and robustness study with pressure data. Geophysics 80(6):M129–M141

Yang D, Liu F, Morton S, et al. (2016) Time-lapse full-waveform inversion with ocean-bottom-cable data: Application on valhall field. Geophysics 81(4):R225–R235

Yang P, Gao J, Wang B (2015b) A graphics processing unit implementation of time-domain full-waveform inversion. Geophysics 80(3):F31–F39

Zhan G, Boonyasiriwat C, Dai W, et al. (2009) Multi-source waveform inversion with deblurring: Journal of seismic exploration

Zhang T, Cai X, Hall K, et al. (2025) Assessing the value of combined use of distributed acoustic sensing and multicomponent vertical seismic profiling data with network-based full-waveform inversion and uncertainty quantification: A case study in alberta, canada. Geophysics 90(1):B29–B47

Zhang X, Curtis A (2020) Variational full-waveform inversion. Geophysical Journal International 222(1):406–411

Zhang Z, Huang L (2013) Double-difference elastic-waveform inversion with prior information for time-lapse monitoring. Geophysics 78(6):R259–R273

Zhang Z, Huang L, Lin Y (2012) Double-difference elastic-waveform inversion with weighted gradients for monitoring egs reservoirs. In: Thirty-Seventh Workshop on Geothermal Reservoir Engineering, Stanford University California

Zheglova P, Ravasi M, Vasconcelos I, et al. (2023) Target-enclosing inversion using an interferometric objective function. Geophysical Journal International 232(1):37–52

Zheng Y, Barton P, Singh S (2011) Strategies for elastic full waveform inversion of time-lapse ocean bottom cable (obc) seismic data. In: SEG Technical Program Expanded Abstracts 2011. Society of Exploration Geophysicists, p 4195–4200

Zhou W, Lumley D (2021a) Central-difference time-lapse 4d seismic full-waveform inversion. Geophysics 86(2):R161–R172

Zhou W, Lumley D (2021b) Nonrepeatability effects on time-lapse 4d seismic full-waveform inversion for ocean-bottom node datanr effects on 4d fwi. Geophysics 86(4):R547–R561